



**HAL**  
open science

# Intrinsic tactile sensing system for robotic dexterous manipulation

Andrés Felipe Ospina Triviño

► **To cite this version:**

Andrés Felipe Ospina Triviño. Intrinsic tactile sensing system for robotic dexterous manipulation. Robotics [cs.RO]. Université Pierre et Marie Curie - Paris VI, 2017. English. NNT : 2017PA066369 . tel-01743738

**HAL Id: tel-01743738**

**<https://theses.hal.science/tel-01743738v1>**

Submitted on 26 Mar 2018

**HAL** is a multi-disciplinary open access archive for the deposit and dissemination of scientific research documents, whether they are published or not. The documents may come from teaching and research institutions in France or abroad, or from public or private research centers.

L'archive ouverte pluridisciplinaire **HAL**, est destinée au dépôt et à la diffusion de documents scientifiques de niveau recherche, publiés ou non, émanant des établissements d'enseignement et de recherche français ou étrangers, des laboratoires publics ou privés.

# Université Pierre et Marie Curie

École doctorale ED391: Sciences mécaniques, acoustique,  
électronique et robotique de Paris

Commissariat à l'énergie atomique et aux énergies alternatives

## Intrinsic tactile sensing system for robotic dexterous manipulation

Presented by

Andrés Felipe OSPINA TRIVIÑO

Directed by Alain MICAELLI

Presented the 28/04/2017

To:

*Directeur :* Alain MICAELLI

*Co-encadrant :* Saifeddine ALOUI

Mathieu GROSSARD

*Rapporteurs :* Cédric CLEVY

Yassine HADDAB

*Examineurs :* Faïz BEN AMAR



# Contents

<b>Introduction</b>	<b>1</b>
<b>1 Adaptation of MEMS based three-axis force sensor to dexterous manipulation requirements</b>	<b>5</b>
1.1 State of the art . . . . .	6
1.2 Existing 3-axis force sensor . . . . .	9
1.3 3-axis force sensor characterization . . . . .	14
1.4 Coating of the 3-axis force sensor . . . . .	20
1.5 Resistance to high forces test . . . . .	26
1.6 Conclusion . . . . .	27
<b>2 Intrinsic tactile sensing systems based on an array of 3 axis force sensors</b>	<b>29</b>
2.1 State of the art . . . . .	30
2.2 Intrinsic tactile sensing feasibility test . . . . .	40
2.3 Intrinsic tactile sensing system adapted to robotic finger implementation . . . . .	55
<b>3 Early slip detection for an intrinsic tactile system</b>	<b>65</b>
3.1 State of the art: Limit surface . . . . .	66
3.2 State of the art: Contact models for soft fingers . . . . .	69
3.3 Soft fingertips characterization . . . . .	78
3.4 Slip detection using limit surface . . . . .	92
<b>Conclusion and perspectives</b>	<b>101</b>
<b>A Test system</b>	<b>103</b>
A.1 Measuring devices . . . . .	103
A.2 Data acquisition and motor control . . . . .	111
<b>Bibliographie</b>	<b>119</b>



# List of Figures

1.1	Coated 3-axis force sensors arrays . . . . .	8
1.2	Protected 3-axis force sensor of [Bec+08] . . . . .	8
1.3	Protected 3-axis force torque sensor of [Ho+11] . . . . .	9
1.4	Protected 3-axis force sensor of [Db10] . . . . .	9
1.5	Sensor structure . . . . .	10
1.6	Transversal view of the sensor . . . . .	10
1.7	Configuration and distribution of the piezoresistors . . . . .	11
1.8	Analogue electronic . . . . .	13
1.9	Sensor connection with the PCB . . . . .	15
1.10	Conditioned sensor . . . . .	15
1.11	Conditioned sensors . . . . .	16
1.12	Sensor placed on support . . . . .	16
1.13	Trajectory for the sensor characterization . . . . .	17
1.14	Results of the sensor characterization . . . . .	18
1.15	Graph of linearity . . . . .	18
1.16	Dynamic response of the sensor when the exerted forces are released . . . . .	19
1.17	Frequency response and phase of the force sensors . . . . .	20
1.18	Behaviour of the force sensors to a step input . . . . .	20
1.19	Conditioned coated sensors . . . . .	21
1.20	Sensor placed on support . . . . .	22
1.21	Results of the coated sensor characterization . . . . .	23
1.22	Graph of linearity of the coated sensors . . . . .	24
1.23	Dynamic response of the coated sensor when the exerted forces are released . . . . .	25
1.24	Frequency response and phase of the coated force sensors . . . . .	25
1.25	Behaviour of the coated force sensors to a step input . . . . .	25
1.26	Results of the selected coated sensors . . . . .	26

2.1	Cross section of the skin in the human hand [Wol06] . . . . .	31
2.2	Motor and sensory homunculus . . . . .	35
2.3	Array of 3-axis force sensor of [Alc+13] . . . . .	36
2.4	Different configurations to locate the ATI sensor in a robotic finger . . . . .	36
2.5	Two sensors configurations of three 3-axial force sensors for a robotic finger . . .	37
2.6	Biotac commercial system . . . . .	37
2.7	Hybrid system by [CM06] . . . . .	38
2.8	Intrinsic measure from six-axis force/torque sensor . . . . .	38
2.9	Intrinsic measure from multiple sensors . . . . .	39
2.10	Tactile system configuration for the flat surface tactile sensor . . . . .	41
2.11	Top view of the base with the sensors . . . . .	42
2.12	Flat surface system . . . . .	42
2.13	Minimal force applied with approximated calibration values . . . . .	47
2.14	Setup of experiment 1 . . . . .	48
2.15	Trajectories used for sensor test . . . . .	48
2.16	Experimental results of experiment 1 . . . . .	49
2.17	Setup of experiment 2 . . . . .	50
2.18	Setup of experiment 3 . . . . .	51
2.19	Minimal force applied with full system calibration . . . . .	52
2.20	Experimental results of experiments 2 and 3 . . . . .	53
2.21	Design of the system . . . . .	56
2.22	Mounted sensors in the PCB . . . . .	57
2.23	Mounted rigid frame and tactile system . . . . .	57
2.24	Intrinsic measures . . . . .	60
2.25	Trajectories for calibration . . . . .	61
2.26	Experimental results . . . . .	62
3.1	Representation of the COR and the local infinitesimal area $dA$ where each force is calculated . . . . .	67
3.2	Representation limit surface . . . . .	69

3.3	Power Law model of pressure distribution . . . . .	70
3.4	Limit surface based on the Power in law model . . . . .	70
3.5	Viscoelastic model of contact . . . . .	71
3.6	Block model of the equation 3.18 . . . . .	74
3.7	Block model of the equation 3.31 . . . . .	76
3.8	Block-scheme initial representation normal force $N$ to radius of contact $a$ and the parameter $k$ . . . . .	78
3.9	Soft fingertips design 1 . . . . .	79
3.10	Intrinsic system with soft surface . . . . .	80
3.11	Test bench: Viscoelastic characterization . . . . .	81
3.12	Block-scheme representation normal force $N$ to radius of contact $a$ and the parameter $k$ v2 . . . . .	82
3.13	Results . . . . .	84
3.14	Block-scheme representation normal force $N$ to radius of contact $a$ and the parameter $k$ v3 . . . . .	85
3.15	Function $H_L(s)$ . . . . .	85
3.16	Results . . . . .	87
3.17	Block-scheme representation normal force $N$ to radius of contact $a$ and the parameter $k$ v3 . . . . .	88
3.18	Results . . . . .	89
3.19	Block-scheme representation normal force $N$ to radius of contact $a$ and the parameter $k$ v4 . . . . .	89
3.20	Coupling equation illustration . . . . .	90
3.21	Parameter $k$ estimated to a step input . . . . .	91
3.22	Block-scheme representation normal force $N$ to radius of contact $a$ and the parameter $k$ . . . . .	92
3.23	Test bench: Slip detection . . . . .	93
3.24	Frictional force $f_f$ and normal torque $\tau_N$ . . . . .	96
3.25	Pressure distribution and limit surface for the finger A . . . . .	97
3.26	Pressure distribution and limit surface for the finger B . . . . .	98
A.1	Two axis force measurement system . . . . .	103



---

A.2	Second order mass spring damper . . . . .	104
A.3	Force transducer operating principle . . . . .	105
A.4	Force transducer characterisation . . . . .	106
A.5	Measures for the characterization . . . . .	106
A.6	Dynamic reaction force transducer to step signal . . . . .	108
A.7	Three axis force measurement system . . . . .	109
A.8	Characteristics of the K3D40 sensor . . . . .	110

# List of Tables

1.1	3-axis force MEMs sensors . . . . .	7
1.2	Error statistics sensor . . . . .	19
1.3	Error statistics coated sensor . . . . .	24
2.1	Mechanoreceptors, adapted from [Dah+10] and [DN04] . . . . .	31
2.2	Summary of needed tactile sensor characteristics for dexterous manipulation (Adapted from [Dah+10], [YBA11], [Lee00]) . . . . .	34
2.3	Error statistics of experiment 1 . . . . .	50
2.4	Error statistics of experiments 2 and 3 . . . . .	54
2.5	Error statistics for experiment 1 . . . . .	61
3.1	Soft finger properties . . . . .	80
3.2	Elastic functions . . . . .	82
3.3	Elastic response $N^{(e)}(\delta)$ parameters . . . . .	83
3.4	Creep compliance function $h(t)$ parameters . . . . .	86
3.5	Goodness of fit reduced relaxation function (NRMSE) . . . . .	88
3.6	Goodness of fit radius of contact (NRMSE) . . . . .	88
3.7	Distances from the COR . . . . .	94
A.1	Error statistics force transducer . . . . .	107
A.2	Reference sensor characteristics: sensibility . . . . .	109
A.3	Reference sensor characteristics: bias . . . . .	109



# Introduction

Industrial robots are traditionally located in controlled environments. Most of them are equipped with one or many grippers, each adapted to a single task. Future factories are moving towards more generic robotic manipulators with abilities to manipulate a variety of objects. Meanwhile, robots are emerging in demotics, restauration and entertainment which require them to perform more human like manipulation tasks. This means that the need for a more generic and dexterous manipulators is increasing.

To achieve dexterous manipulation of objects, robots need to "feel" the touch of the object in order to determine the adequate way to hold and grasp it. This ability is called artificial tactile sensing. It consists in measuring a given property, such as force or temperature, through contact with an object, then deducing certain parameters such as direction and position of the force, torques, texture, hardness, sliding, object shape, etc. This allows the robot to adapt its action parameters in order to optimize the way it holds the object and reduce the probability of destroying it.

Most of the robotic systems created for dexterous manipulation of objects are inspired from the human body. However, developing a robotic system that mimics the human body is highly complex. No system created by men has the capabilities of the central nervous system, nor the thousands of receptors placed on the muscles and skin. Therefore, the different manipulation systems are adapted to a specific manipulation context, with several hypothesis and mathematical models created for different tasks.

Studies like [LN99], [YBA11] and [Dah+10] have focused on the characteristics of tactile systems needed to achieve robotic dexterous manipulation of objects derived from human touch sense characteristics. Others, like [Mur+94], based their studies on the mathematical models using mechanical analysis.

To achieve robustness of the control adapted to a dexterous manipulation task, there are two main essential elements to satisfy in the tactile system:

- The knowledge of the contact information (the contact area, the contact center position, as well as the force and torque vectors applied through the contact).
- The detection of slippage.

The first element allows a higher efficiency in the gripping process essentially when dealing with fragile objects. The second element allows monitoring the safety and effective quality of the grip.

The CEA-LIST has designed a fully modular and anthropomorphic hand, which exactly replicates the kinematics of the human hand, adding up to 24 degrees of mobility and 20 degrees of freedom, which is a design challenge if a high level of dexterity must be guaranteed. A thorough mechanical design assures backdrivability through the whole mechanism, including actuators and transmission of movement to the joints [MG14] [GMP15]. This feature greatly improves the sensory capabilities of the hand: every surface becomes sensitive as every part of the hand is driven by a backdrivable actuator. However, such an anthropomorphic gripper suffers from a lack of knowledge about the contact point localization on the one hand, and the quantitative estimation of all the distal force-torque components on the other hand.

Therefore, a suitable tactile system should be added to the robotic gripper in order to meet most of the requirements of dexterous manipulation. In this field, the most used systems are based on the Biotac [Syn] and the Ati Nano 17 [Ati] sensors. Both tactile systems have been widely implemented, such as in [Cio+13] and [Bat+16]. Each system has its advantages and disadvantages. The main disadvantage of the Biotac is that the system cannot measure the applied torques. It can measure just one-force component. In the other hand, the Ati Nano 17 cannot measure the distribution of pressure.

Meanwhile, the CEA-Leti developed a 3-axis force sensor based on Micro Electro-Mechanical system (MEMS) technology. This sensor has been used in different applications such as texture detection [Db10] and human skin analysis [CPD11] with promising experimental results. This sensor could differentiate texture on a printed page, i.e., the difference between the surfaces covered with ink and the blank paper. This doctoral work is intended to explore the possibility of creating a suitable tactile sensing system for robotic dexterous manipulation purposes based on the 3-axis force sensor developed by CEA-Leti. The developed system should meet as many requirements as possible by combining one or several sensors. The objective is to create a system that can benefit from the small size and high integrality of the 3-axis force sensor in order to provide the following contact information: the contact area (given sufficient information about the manipulated object nature and the manipulator characteristics), the contact center position, as well as the force and torque vectors applied through the contact.

In other perspective, one of the most important aspect in dexterous manipulation of objects is the detection of slippage. Force torque sensors such as the Ati Nano 17 are able to predict slippage by applying different theories. For example, slip theory of friction cone by applying the coulombs law or an elliptical approximation of the relation force of friction and applied torque as presented in [Mel00]. In the case of the commercial sensor Biotac, the slippage cannot be predicted because there is no measurement of the tangential forces or normal torque. Therefore, the slippage should be estimated by the vibrations as presented in [Rei+14], or by the thermal micro fluxes as presented in [FAG13]. Additionally, the system can be implemented with machine learning to prevent slippage. However, as presented in [Rei+14], the system is unable to detect when the object slips by an applied torque. Therefore, an analysis of slippage should be done with the tactile system based on the 3-axis force sensors.

This work is mainly divided in three chapters. Given the variety of subjects, each chapter has a section dedicated to the state of the art.

The 3-axis force sensor developed by the CEA presents interesting characteristics, such as high resolution, small size and linearity. However, the range of forces of the sensor should be enlarged to meet the requirements of dexterous manipulation of objects. Therefore, chapter 1 is dedicated to the protection of the 3-axis force sensor. The chapter is mainly divided into 6 sections: the first section describes the state of the art related to the protection of multi-axis force MEMs sensors. The second section shows the operation principle and the theoretical characteristics of the 3-axis sensor. The third section is dedicated to the experimental characterization of the sensor. In order to protect the sensor and increase its sensitivity range, the fourth section deals with sensor protection using different coating techniques. The fifth section deals with the characterization and analysis of the coated sensors. A coating technique is selected based on the desired sensor characteristics. Finally, some of the coated sensors are tested to validate their resistance to high-applied forces.

The next stage consists in finding the best manner to implement the 3-axis force sensor as a tactile system. Two main ideas can be applied; the first idea is to implement one or many

sensors side by side. However, it would only measure the three axes of forces and the spatial resolution would be inappropriate. In the other hand, an array of 3-axis force sensors fixed to a rigid surface can produce an equivalent to the force-torque sensor ATI Nano 17. Those systems are called intrinsic tactile systems. Chapter 2 presents the development of two different intrinsic tactile systems. It is divided into three sections. The first section is the state of the art on tactile sensing systems. The goal of this section is to guide the research around the best way to implement the 3-axis force sensor of chapter 1 in a tactile sensing system. With the conclusion and the system proposal of the first section, the second section is intended to prove and test the capabilities of the proposed tactile system. The last section discusses the creation of the proposed system for a robotic gripper and the integration into a soft contact approach.

Finally, the detection of slippage using an intrinsic tactile system is presented in chapter 3. This chapter is divided into five sections: The first section describes the friction limit theory named limit surface. The second section, reviews the viscoelastic contact model that is necessary to implement the limit surface theory on an intrinsic tactile sensing system. The third part shows the construction and characterization of soft fingers based on the viscoelastic model of contact. The fourth section reports the implementation of limit surface theory for early slippage detection on an intrinsic tactile system. Finally, the results are analyzed and conclusions are made.



# Adaptation of MEMS based three-axis force sensor to dexterous manipulation requirements

---

## Contents

---

<b>1.1</b>	<b>State of the art</b> . . . . .	<b>6</b>
1.1.1	MEMS based 3-axis force Sensors . . . . .	6
1.1.2	MEMS sensors protection . . . . .	7
1.1.3	Conclusion . . . . .	9
<b>1.2</b>	<b>Existing 3-axis force sensor</b> . . . . .	<b>9</b>
1.2.1	Operation principle . . . . .	9
1.2.2	Dimensions and characteristics of the sensor . . . . .	12
1.2.3	Processing the sensor signal . . . . .	13
<b>1.3</b>	<b>3-axis force sensor characterization</b> . . . . .	<b>14</b>
1.3.1	Sensor conditioning . . . . .	15
1.3.2	Characterization methodology . . . . .	16
1.3.3	Characterization results . . . . .	17
1.3.4	Analysis of the results . . . . .	19
<b>1.4</b>	<b>Coating of the 3-axis force sensor</b> . . . . .	<b>20</b>
1.4.1	Coating process . . . . .	21
1.4.2	Coated sensor characterization . . . . .	22
1.4.3	Characterization results of the coated sensors . . . . .	22
1.4.4	Result analysis and conclusions . . . . .	22
<b>1.5</b>	<b>Resistance to high forces test</b> . . . . .	<b>26</b>
<b>1.6</b>	<b>Conclusion</b> . . . . .	<b>27</b>

---

## Context and motivations

The CEA-Leti has developed a 3-axis MEMs force sensor that exhibits interesting characteristics such as linear behaviour, low hysteresis, and good accuracy (for more details refer to [DB+09] and section 1.2.2). Together with CEA-List, CEA-Leti foresee the possibility of implementing the sensor as a tactile sensing system for a robotic anthropomorphic gripper.



The sensor, as is, has few defaults : it has a small sensitive area and low maximum supported force (the maximum tangential force supported by the sensor is 1 N). Therefore, a suitable coating should be applied to the sensor in order to meet the necessary measuring force range for dexterous manipulation of objects.

## Chapter objective

The main objective of this chapter is the study of the protection for multi-axis force sensors based on the technology Micro Electro-Mechanical Systems (MEMS).

## Outline of the chapter

This chapter is mainly divided into 6 sections: the first section describes the state of the art related to the protection of multi-axis force MEMS sensors. The second section shows the operation principle and the theoretical characteristics of the 3-axis sensor. The third section is dedicated to the experimental characterization of the sensor. In order to protect the sensor and increase its sensitivity range, the fourth section deals with the sensor protection using different coating techniques. The fifth section deals with the characterization and analysis of the coated sensors. A coating technique is selected based on the desired sensor characteristics. Finally, some of the coated sensors are tested to validate their resistance to high applied forces.

## 1.1 State of the art

This section reviews the state of the art related to the protection of multi-axis force MEMS sensors. The main goal is to understand what has been made to the protection for this type of sensor. Additionally, conclude what is the following step to protect the 3-axis force sensor created by the CEA.

### 1.1.1 MEMS based 3-axis force Sensors

Micro Electro-Mechanical Systems (MEMS) development helped creating miniaturized and accurate sensors, such as accelerometers and gyroscopes [Reb04]. It has allowed massive production of inexpensive and small sensors present nowadays in nearly all new smart-phones.

To create force MEMS sensors, different technologies have been developed such as bulk micro-machining and surface micromachining. These technologies are used to create silicon structures inside a silicon wafer. Microelectronic silicon structures, transducers and interconnections are used to create sensitive systems. In the case of force measurement, transducers measure the mechanical deformation. Most commonly, they change their resistance or its capacitance when they exhibit a deformation.

In tactile sensing field, force/torque MEMS based sensors such as presented in Table 1.1 have allowed a highly integrated touch sensing systems.

This type of sensors has interesting characteristics such as linear behavior, low hysteresis, and high accuracy. However, because of their size and fragility, they can't resist to high applied forces (as shown in table 1.1, the maximal normal force that the listed sensors can support

Reference			Characteristics		
Year	Author	Ref.	Force range [N]		Sensitive area
			Normal	Shear	
<b>3-axis force sensors arrays</b>					
2011 - 2013	Candelier, Alcheikh	[CPD11] [Alc+13]	0 to 0.08	0 to 0.03	0.7 mm $\varnothing$
2010	Choi	[Cho10]	0 to 0.08	0 to 0.08	1.5 mm $\varnothing$
2009	Sohgawa	[Soh+09]	0 to 0.13	0 to 0.03	1 mm $\times$ 1 mm
2008	Lee	[Lee+08]	0 to 0.01	0 to 0.01	1.3 mm $\times$ 1.3 mm
2007	Vásárhelyi	[Vá07]	0 to 0.01	no data	0.25 mm $\times$ 0.25 mm
2006	Kim	[Kim+06]	0 to 2	0 to 2	1.2 mm $\times$ 1.2 mm
<b>3-axis force sensors</b>					
2001 - 2011	Dao, Ho	[Dao+01],[Ho+11]	no data	0 to 1	1.7 mm $\times$ 1.7 mm
2010	Boissieu	[Db10]	0 to 2	0 to 1	2 mm $\varnothing$
2009	Noda	[Nod+09]	0.05 to 3	0.05 to 3	20 mm $\times$ 20 mm
2009	Wang	[WB00]	0 to 0.4	0 to 0.4	10 mm $\times$ 10 mm
2005 - 2008	Beccai	[Bec+05] [Bec+08]	0 to 3	0 to 0.5	2 mm $\varnothing$
2006	Noda	[Nod+06]	0 to 4	0 to 4	20 mm $\times$ 20 mm

Table 1.1: 3-axis force MEMs sensors

without protection is about 4N). For most tactile applications, such as object manipulation in robotics manipulation tasks, the range of forces that the sensor should support must be at least 10 N [YBA11] (further explanation is presented in section 2.1).

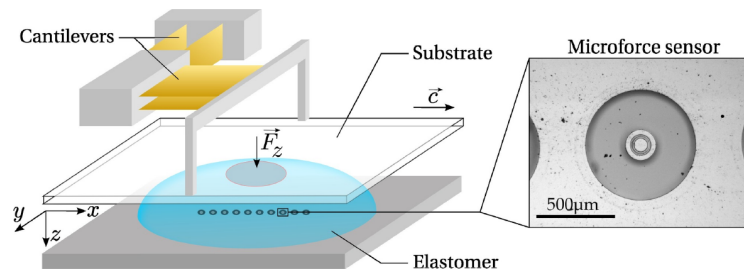
### 1.1.2 MEMS sensors protection

To solve the problem of measurement range, a solution consists in making bigger silicon based sensors with bigger supports. However, due to technology considerations, the size of the sensor can not be big enough to cover a large surface which doesn't solve the small sensitive area problem. In addition, using more silicon would significantly increase the sensor cost. Another possible solution consists in protecting the sensor with an elastic coating layer, this solution was applied in most of the listed research papers such as [CPD11], [Db10], [Ho+11], [Nod+06] and [Vá07]. This solution distributes the forces between the sensitive part of the sensor and the solid area around it which increases the sensor dynamic range. This solution provides protection to the sensor, increases the sensitive surface area and enables the sensor to be interfaced with an external frame for intrinsic tactile sensing such as presented in chapter 2.

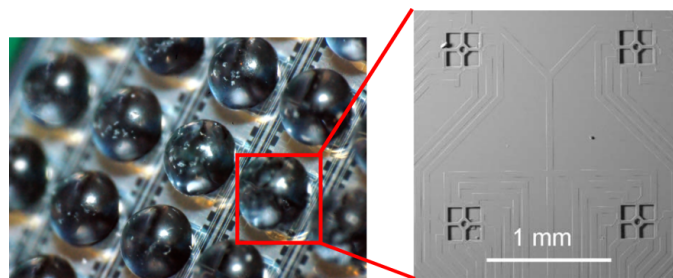
Coating the sensor can have many drawbacks such as the introduction of non linearity and hysteresis. Depending on the used elastic material, a relaxation phenomenon may appear and significantly change the sensor response to external load. The coating increases the dynamic measurement range by distributing the force between the sensor and the surface around which reduces the sensor resolution. Finally, the analysis of the forces applied on any point of the surface is complex.

In [CPD11] and [Vá07], the authors made an extended analysis of the behavior of an array of 3-axis force sensors covered by different types of elastic covers as shown in Figure 1.1. In [CPD11], they mold a sphere section to cover a line of ten 3-axis force sensors with PolyDiMethylSiloxane (PDMS) to investigate the mechanism of tactile transduction during active exploration. In [Vá07] the author creates a 3-axis force sensor and proposes different elastic covers, the first

one a plane parallel to the base of the sensors, and a second one of hemispheres in each sensor of the array as show in Figure 1.1b. The analysis of those arrays is based on the characterization of the behavior of the covered sensors with respect to the position and direction of the applied forces.



(a) Tactile system proposed by [CPD11]



(b) Tactile system proposed by[Vá07]

Figure 1.1: Coated 3-axis force sensors arrays

In [Bec+08], the authors protect a 3-axis force sensor with a polyurethane coating as shown in Figure 1.2. This system is used to detect slippage. The maximum supported force is 15 N for normal force and 11 N in tangential force. The system assume a constant force distribution in the surface.

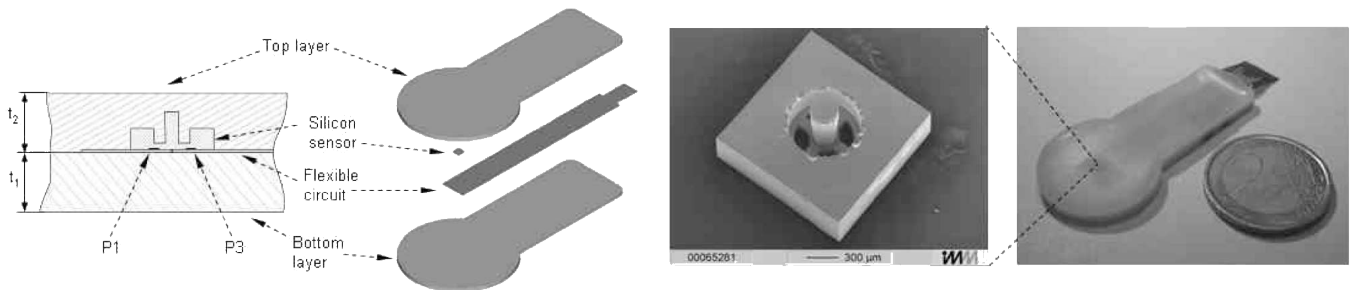


Figure 1.2: Protected 3-axis force sensor of [Bec+08]

In [Ho+11], the authors create a hemispherical soft fingertip, the system consists of a 6-axis force torque sensor embedded in a polyurethane rubber as shown in Figure 1.3. The system could estimate the forces applied during the contact with an external object. They also propose a model to find the position and direction of the applied forces.

In [Db10], the authors tests different types of coating for a 3-axis force sensor, between the ones shown in Figure 1.4. The goal of their research is the discrimination of textures using a normal force of 0.5 N. Therefore no maximal force was estimated, and no comparison between the coatings was made.

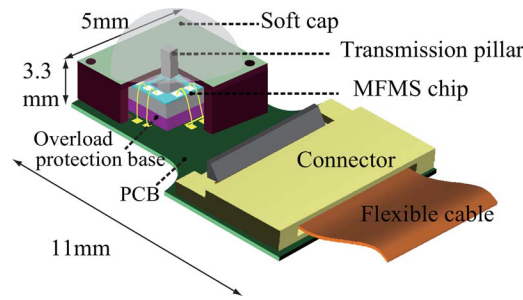


Figure 1.3: Protected 3-axis force torque sensor of [Ho+11]

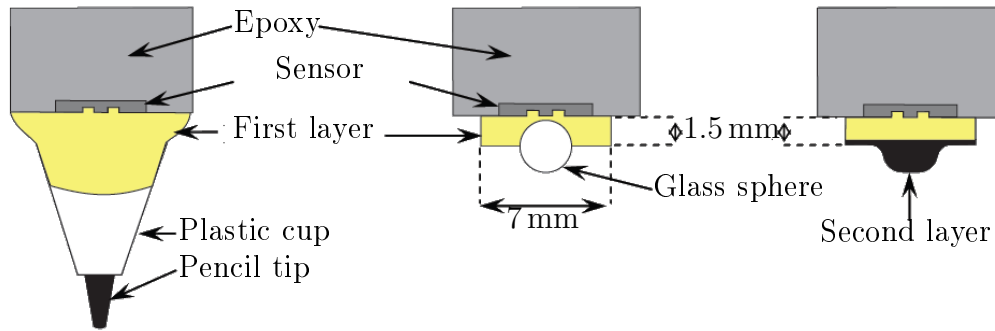


Figure 1.4: Protected 3-axis force sensor of [Db10]

### 1.1.3 Conclusion

The published articles related to the protection of MEMs force sensors such as [Db10],[Ho+11], [Bec+08] or [CPD11] do not give any comparison between the coatings. They did not discuss the effect of the specific coating shape, size and material. One goal of this chapter is to provide guidelines for the design and construction of the coating for MEMs force sensors supported with experimental results and comparison between various predefined coatings. The objective is to identify the coating shape, size and material that provides the lowest alteration to the sensor characteristics while increasing its dynamic range and providing protection against high forces.

## 1.2 Existing 3-axis force sensor

This section briefly describes the 3-axis force sensor developed by the CEA-Leti. This sensor is used in this chapter as the target MEMs sensor to protect.

### 1.2.1 Operation principle

The force sensor operates on the principle presented in [Yao+87]. This consists of eight strains of sensitive elements that are attached to a stem. All these elements are made of the same silicon crystal and have a geometry shown in the figure 1.5.

In this case the sensor is made of a monocrystalline silicon element, where the sensitive elements are eight piezoresistors, i.e. their resistance value varies according to their deformation. They are created by doping the underside of the silicon membrane. The piezoresistors are placed

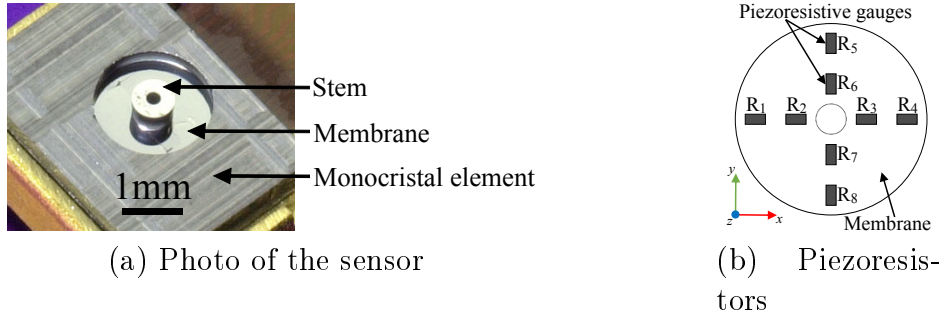


Figure 1.5: Sensor structure

in the  $xy$  plane. This plane is tangential to the membrane as shown in figure 1.5b. When the membrane is deformed, the piezoresistors are either compressed or stretched, depending on their position in the membrane. The resistance changes according to the equation of proportionality 1.1.

$$\frac{\Delta R}{R} = \sigma k_{\sigma} \quad (1.1)$$

Where  $\sigma$  is the stress applied to the material,  $k_{\sigma} = 138 \times 10^{-11} \text{ Pa}^{-1}$  is the constant of the p-doped material [KDR94],  $R$  is the resistance of the piezoresistance, and  $\Delta R$  is the change in resistance caused by the deformation of the membrane.

The eight piezoresistive elements have a similar resistance value  $R_i$  at rest, and are placed so that they are constrained symmetrically upon application of a force along an axis  $x$ ,  $y$  or  $z$ . The figure 1.6 shows schematically the deformation of the membrane during the application of a normal force  $F_z$  or tangential forces  $F_x$ ,  $F_y$  in the plane of the membrane. The stress  $\sigma_i$  to which each piezoresistor is subjected during deformation of the membrane can be decomposed into the sum of three different constraints  $\sigma_{F_x}$ ,  $\sigma_{F_y}$ ,  $\sigma_{F_z}$ , respectively proportional to the values of the three components  $F_x$ ,  $F_y$  and  $F_z$  of the force applied to the sensor. Therefore,  $\Delta R$  can also be decomposed in the sum of  $R_x$ ,  $R_y$ ,  $R_z$  and it is respectively proportional to the forces  $F_x$ ,  $F_y$  and  $F_z$ .



Figure 1.6: Transversal view of the sensor

The piezoresistors are associated to each other in a Wheatstone bridge arrangement, according to  $x$  and  $y$  axis, as shown in Figure 1.7. In the first instance, all resistors are considered to be of equal value, so  $R_i = R$ . When no force is applied, the voltage  $V_A$ ,  $V_B$ ,  $V_C$  and  $V_D$  is a fixed value close to  $V_{in}/2$  where  $V_{in}$  is the supply voltage of the bridges. Once a force is applied to the stem, the membrane is warped. This causes the compression or the stretching of the piezoresistors along the  $x$  and  $y$  axis, leading to a change in their resistance values. The resistance variation affects the potentials  $V_A$ ,  $V_B$ ,  $V_C$  and  $V_D$ . By a different set of midpoints, the three components  $F_x$ ,  $F_y$  and  $F_z$  of applied force can be found.

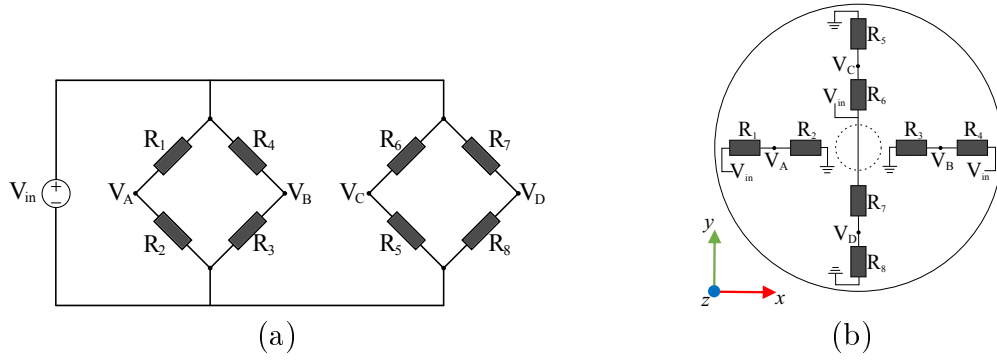


Figure 1.7: Configuration and distribution of the piezoresistors

Consider the case of a tangential force  $F_x$  applied to the stem in the direction of the x axis, as shown in Figure 1.6a. The piezoresistors  $R_1$  and  $R_3$  are stretched taking the resistance value  $R + \Delta R_x$ , while  $R_2$  and  $R_4$  are compressed taking the  $R - \Delta R_x$  value. Respectively, the voltages  $V_A$  and  $V_B$  are obtained:

$$\frac{V_A}{V_{in}} = \frac{R_2}{R_1 + R_2} = \frac{R - \Delta R_x}{2R} \quad (1.2)$$

In the same way:

$$\frac{V_B}{V_{in}} = \frac{R_3}{R_4 + R_3} = \frac{R + \Delta R_x}{2R} \quad (1.3)$$

Defining  $U_x$  according to equation 1.4 gives a voltage proportional to the force  $F_x$  applied along the x axis.

$$U_x = (V_B - V_A) = V_{in} \frac{\Delta R_x}{R} \quad (1.4)$$

In the same way, the voltage  $U_y$  can be defined proportional to the force  $F_y$  applied along the y axis.

$$U_y = (V_C - V_D) = V_{in} \frac{\Delta R_y}{R} \quad (1.5)$$

Now consider the case of a normal force  $F_z$  applied to the stem (see Figure 1.6b). Here the piezoresistors  $R_1$  and  $R_4$  are compressed while  $R_2$  and  $R_3$  are stretched. Similarly,  $R_5$  and  $R_8$  are compressed and  $R_6$  and  $R_7$  are stretched. Thus, for the voltages  $V_{A,B,C,D}$  we obtain:

$$\frac{V_A}{V_{in}} = \frac{V_B}{V_{in}} = \frac{R + \Delta R_z}{2R} \quad (1.6)$$

and

$$\frac{V_C}{V_{in}} = \frac{V_D}{V_{in}} = \frac{R - \Delta R_z}{2R} \quad (1.7)$$

Defining  $U_z$  as a voltage proportional to the force  $F_z$ ,

$$U_z = (V_B + V_A) - (V_C + V_D) = V_{in} \frac{2\Delta R_z}{R} \quad (1.8)$$

It may be noted that for a zero force  $f_z$ ,  $U_z = 0$  V, whatever the applied tangential force  $f_{x,y}$ . Similarly, for a zero tangential force,  $u_x = u_y = 0$  V whatever the normal force  $f_z$  applied. In the ideal case, given that the x, y and z axis are orthogonal,  $u_x$ ,  $u_y$  and  $u_z$  measure independently the components  $f_x$ ,  $f_y$  (tangential forces) and  $f_z$  (normal force) of force  $\vec{f}$ :

$$\vec{f} = \begin{bmatrix} f_x \\ f_y \\ f_z \end{bmatrix} = \begin{bmatrix} S_x & 0 & 0 \\ 0 & S_y & 0 \\ 0 & 0 & S_z \end{bmatrix} \begin{bmatrix} u_x \\ u_y \\ u_z \end{bmatrix} \quad (1.9)$$

where  $S_x$ ,  $S_y$ , and  $S_z$  are the sensitivities and  $f_x$ ,  $f_y$  and  $f_z$ , the forces. By symmetry, it is considered that the sensitivities along the axes x and y are identical, so  $S_x = S_y = S_{xy}$ .

### 1.2.2 Dimensions and characteristics of the sensor

The sensor, originally developed for other applications, was made in different sizes for different sensitivities. The sensitivities  $S_{xy}$  and  $S_z$  are mainly defined by the ratio between the radius of the membrane, the radius of the stem, and by the thickness of the membrane. The smaller the ratio between the membrane radius and the stem radius, the more sensitive the sensor will be. Besides, if the membrane is thin, the sensor is more sensitive and fragile.

The different variants of the sensor were characterized in normal and tangential forces as described in [Db10]. With the monocrystalline nature of the sensor and the elasticity of silicon, the sensor has a linear behaviour with respect to normal and tangential forces. Among all the sensors produced at LETI, we used an available variant of the sensor with the following characteristics:

- Membrane radius: 1000  $\mu\text{m}$
- Membrane thickness: 100  $\mu\text{m}$
- Stem radius: 575  $\mu\text{m}$
- $S_{x,y}$  Sensitivity :  $(8.5 \pm 0.3)$  mV/V/N
- $S_z$  Sensitivity:  $(3.0 \pm 0.5)$  mV/V/bar
- $P_z$  max pressure. before deteriorating: 15 bar
- $F_{x,y}$  max strength. before deteriorating: 1 N
- Maximum voltage variation before the deteriorating in tangential forces:  $\Delta U_{x,y}$  42.5 mV with a supply voltage of 5 V
- Maximum voltage variation before the deteriorating in normal forces:  $\Delta U_z$  225 mV with a supply voltage of 5 V
- The sensor is 5 mm long, 3.5 mm wide, and 0.8 mm high regardless of the stem.

These variants were developed for very specific applications that didn't need a high force sensitivity range. The robustness of such sensors is very low and not adapted for robotic manipulation tasks. To adapt the sensor for robotic manipulation, the maximum supported force (before breaking), as well as the maximum measurable force should be increased.

### 1.2.3 Processing the sensor signal

The sensor is connected to an analogue circuit which amplifies the signal and performs the operations described by the equations 1.4, 1.5 and 1.8, as shown in the diagram in Figure 1.8.

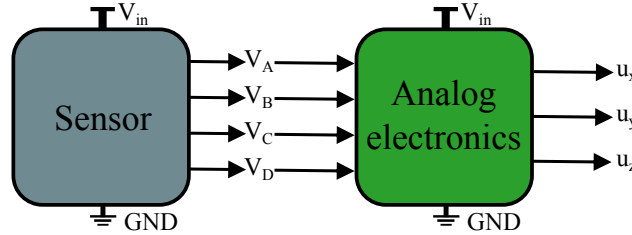


Figure 1.8: Analogue electronic

The input voltage is defined as  $V_{in} = 5\text{ V}$ . The tensions  $u_x$ ,  $u_y$  and  $u_z$  have a centered value of  $2.5\text{ V}$  at rest ( $\vec{F} = 0$ ). These tensions are respectively amplified by the factors  $\alpha_x$ ,  $\alpha_y$  and  $\alpha_z$ . The equations describing this system are as follow:

$$u_x = \alpha_x(V_B - V_A) + \frac{V_{in}}{2} \quad (1.10)$$

$$u_y = \alpha_y(V_C - V_D) + \frac{V_{in}}{2} \quad (1.11)$$

$$u_z = \alpha_z((V_B + V_A) - (V_C + V_D)) + \frac{V_{in}}{2} \quad (1.12)$$

Amplification values can be changed depending on the application. Taking into account the maximum variations given in section 1.2.2, to use the entire range of the sensor (assuming  $V_{in} = 5\text{ V}$ ) the values would be  $\alpha_{x,y} = 50$  and  $\alpha_z = 10$ .

All these calculations are performed with an identical value of the resistors  $R_i$ . In reality, however, the resistance values are not identical. A difference in the resistance would create an offset, i.e. as the voltage difference is not zero - for example if  $V_A - V_B \neq 0$  at rest - in the equation 1.10 this difference would be amplified. The voltage difference caused by the difference in resistance can be calculated as shown in the following equations:

$$0 = V_B - V_A + b'_x \quad (1.13)$$

$$0 = V_C - V_D + b'_y \quad (1.14)$$

$$0 = (V_B + V_A) - (V_C + V_D) + b'_z \quad (1.15)$$



where the values  $b'$  are the calculated offset values when no force is applied to the system. So the electronic analogue output can be written as:

$$u_x - b_x = \alpha_x(V_B - V_A) \quad (1.16)$$

$$u_y - b_y = \alpha_y(V_C - V_D) \quad (1.17)$$

$$u_z - b_z = \alpha_z((V_B + V_A) - (V_C + V_D)) \quad (1.18)$$

where  $b_x = b'_x\alpha_x + \frac{V_{in}}{2}$ ,  $b_y = b'_y\alpha_y + \frac{V_{in}}{2}$ , and  $b_z = b'_z\alpha_z + \frac{V_{in}}{2}$ . Then the equation to calculate the forces 1.9 can be rewritten as:

$$\vec{f} = \begin{bmatrix} f_x \\ f_y \\ f_z \end{bmatrix} = \begin{bmatrix} S_x & 0 & 0 \\ 0 & S_y & 0 \\ 0 & 0 & S_z \end{bmatrix} \begin{bmatrix} u_x - b_x \\ u_y - b_y \\ u_z - b_z \end{bmatrix} \quad (1.19)$$

Knowing that the axes of the sensor have a crosstalk, and that there is a linear relationship between the measured voltage and the forces (shown in [Db10]), then the equation 1.19 is rewritten as:

$$\begin{bmatrix} f_x \\ f_y \\ f_z \end{bmatrix} = \begin{bmatrix} S_{xx} & S_{xy} & S_{xz} \\ S_{yx} & S_{yy} & S_{yz} \\ S_{zx} & S_{zy} & S_{zz} \end{bmatrix} \begin{bmatrix} u_x - b_x \\ u_y - b_y \\ u_z - b_z \end{bmatrix} \quad (1.20)$$

or compact form

$$\vec{f} = \mathbf{S} (\vec{u} - \vec{b}) \quad (1.21)$$

where the vector  $\vec{u}$  are the proportional tensions to the applied forces  $\vec{f}$ ,  $\mathbf{S}$  is a sensitivity matrix and the vector  $\vec{b}$  is the offset signal.

The sensor exhibits several imperfections. For example, due to their nature, the piezoresistors found in the sensor can change their behaviour according to their temperature. In order to solve this problem, a temperature sensing resistance is incorporated inside the sensor. The second spotted problem is that, under certain circumstances, the piezoresistors behave like polarized resistances. This problem needs to be detected before assembling the sensor. The work presented in this document do not dive into temperature compensation. All experiments are conducted in a controlled environment, so the effects of temperature are negligible. As for the polarized resistance, only sensors who do not present polarized resistance symptoms have been used.

### 1.3 3-axis force sensor characterization

The characterization presented in section 1.2.2 was performed using sensor ideal conditions. But as shown in [Db10], this sensor does not have this behavior in practical use conditions.

For this reason, this section deals with characterization of the sensor in real conditions. The characterization of this sensor consists in finding the values of sensitivity matrix  $\mathbf{S}$ , and offset  $\vec{b}$  of the equation 1.21. For this experiment the same test system developed by [Db10] is used. The reference system for the characterization is presented in Appendix A.1.1. This system has only two measurements of force  $f_{zref}$  and  $f_{xref}$ . To characterize a three-axis sensor several measures must be performed considering different sensor orientations to get enough information on its behavior in each axis.

### 1.3.1 Sensor conditioning

To exert forces on the sensor with the system presented in the appendix A.1.1, it is necessary to condition the sensor. First, the sensor is mounted on a PCB (Printed Circuit Board). It should be stuck to the PCB with two different glues. Then the sensor is connected to the PCB via a wire bonding process as shown in figure 1.9. This process is well explained in [Db10]. Depending on the application, different types of PCB were created, mainly round and square. In this section, a square type of PCB is used.

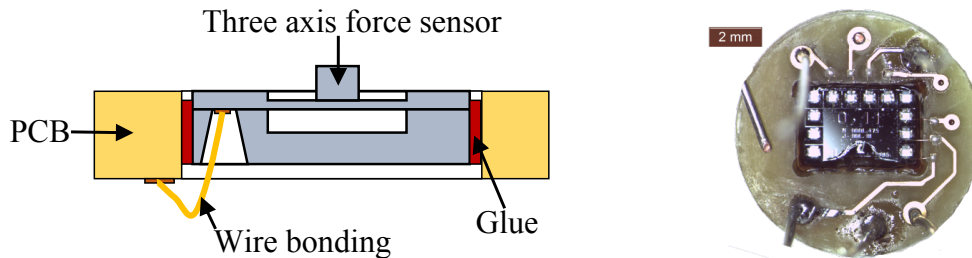


Figure 1.9: Sensor connection with the PCB

The difference in height between the stem and height of the sensor is very small. Thus, it was decided to extend the height of the stem as shows the figure 1.10.



Figure 1.10: Conditioned sensor

A drop of epoxy polymer is placed on top of the stem. This makes it easier to apply forces on the sensor. Three sensors of this type are subject to the same procedure as shown in figure 1.11.

Three sensors are used to test whether the results can be extrapolated, or if each sensor has its own sensitivity matrix. To attach the sensor to the system shown in Appendix A.1.1, the tested sensor is placed in a support made using a 3D printer as shown in Figure 1.12. The support is fixed with screws at the end effector of the test system.

This support is designed to be able to put the tested sensor in two positions:

- In the first position, the axes of the sensor aligned with the test system.
- In the second position, the sensor is rotated 90 degrees so that the y axis of the sensor is aligned with the x axis of the system.

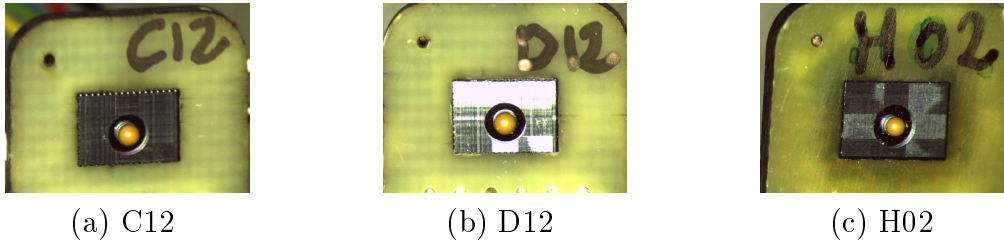


Figure 1.11: Conditioned sensors

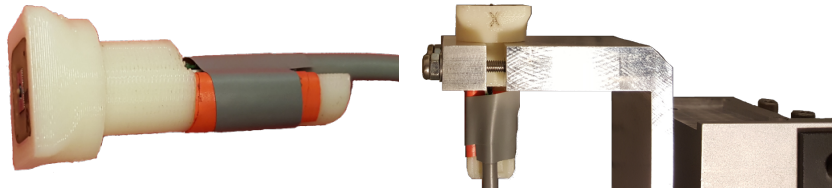


Figure 1.12: Sensor placed on support

### 1.3.2 Characterization methodology

The test system is only capable of measuring the force components  $f_{xref}$  and  $f_{zref}$  applied on the sensor. Thus, it is essential to do two measurement sets, in order to calibrate the sensor. The two positions provided by the support are used to perform those two sets of measurements. For the two sets of measurement, the following measurement methodology is performed:

- Fix the sensor to be characterized in its support;
- Without applying any force, start to acquire the sensor voltages  $\vec{u}$ . This part of the measures is used to calculate the offset  $\vec{b}$ ;
- Bring sensor and the rigid surface into contact by the precision screw, until a force of  $(0.8 \pm 0.2) \text{ N}$  is exerted, and is varied manually without exceeding 1 N force;
- Move two linear motors along a predefined path, to exert tangential forces on the sensor
- When the movement is done, the contact is automatically removed by a pneumatic actuator;
- After 30 seconds, stop the acquisition system.

The defined trajectory is designed to exert a wide range of forces in the different axes, i.e. explore both the positive and negative forces in the x and y axes without breaking the sensor. Unfortunately, the contact between the 3-axis force sensor and the rigid surface has a small friction coefficient, which does not allow to exert tangential forces through all the measurable force range. The trajectory is shown in Figure 1.13. Such a square trajectory permits to investigate the crosstalk between the axes when the forces do not change in the axis x and y.

Since two sets of measurements with different reference components ( $f_x, f_z$  and  $f_y, f_z$ ) are made, the rows of the sensitivity matrix are calculated separately using the corresponding measurements. The different rows can be estimated using a least squares as follows :

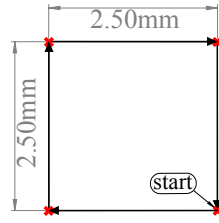


Figure 1.13: Trajectory for the sensor characterization

$$[\hat{S}_{xx} \quad \hat{S}_{xy} \quad \hat{S}_{xz}] = \underset{[S_{xx} \quad S_{xy} \quad S_{xz}]}{\operatorname{argmin}} \sum_{i=1}^n \left( f_{x\operatorname{ref}i} - [S_{xx} \quad S_{xy} \quad S_{xz}] \begin{bmatrix} u_{xi} - b_x \\ u_{yi} - b_y \\ u_{zi} - b_z \end{bmatrix} \right)^2 \quad (1.22)$$

$$[\hat{S}_{yx} \quad \hat{S}_{yy} \quad \hat{S}_{yz}] = \underset{[S_{yx} \quad S_{yy} \quad S_{yz}]}{\operatorname{argmin}} \sum_{i=1}^n \left( f_{y\operatorname{ref}i} - [S_{yx} \quad S_{yy} \quad S_{yz}] \begin{bmatrix} u_{xi} - b_x \\ u_{yi} - b_y \\ u_{zi} - b_z \end{bmatrix} \right)^2 \quad (1.23)$$

$$[\hat{S}_{zx} \quad \hat{S}_{zy} \quad \hat{S}_{zz}] = \underset{[S_{zx} \quad S_{zy} \quad S_{zz}]}{\operatorname{argmin}} \sum_{i=1}^n \left( f_{z\operatorname{ref}i} - [S_{zx} \quad S_{zy} \quad S_{zz}] \begin{bmatrix} u_{xi} - b_x \\ u_{yi} - b_y \\ u_{zi} - b_z \end{bmatrix} \right)^2 \quad (1.24)$$

where  $f_{x\operatorname{ref}i}$ ,  $f_{y\operatorname{ref}i}$ ,  $f_{z\operatorname{ref}i}$  are the reference measurement of forces ( $f_{y\operatorname{ref}i}$  is the measurement taken with the sensor turned  $90^\circ$ ), at sampling time  $i$ , and  $n$  the number of samples.

### 1.3.3 Characterization results

As presented in the previous section, at least two sets of measurements for each axis of each of the three mentioned sensors were made. This is shown in Appendix A.2.1. Half the measurements were used to calculate the sensitivity matrix, and the other half is used to validate the matrix. Figure 1.14, shows the results of the experiments. The left side of the figure presents the results for the measurement set used to calibrate the sensor. The right side of the figure presents the results for the measurement set used to validate the calibration. This figure shows the acquired data to the point where the contact was removed (the last 30s with no contact was removed). In fact, when the contact is released using the pneumatic actuator, the transducers begin to vibrate as shown in section A.1.1.1, so the last part of the acquired data of the measures was not used to calibrate the sensor since the reference is not correct.

Table 1.2 presents the error statistics between the reference system and the three axis force sensors.

Figure 1.15 shows the graphics of the relation between reference forces and the calculated forces, in order to show the characteristics of linearity and hysteresis.

As said before, the reference system vibrates when the contact is removed using the pneumatic actuator which makes its measurement unusable. So, to characterize the dynamic behavior of the sensor in the z axis, the reference data at the instant when the contact is released is replaced

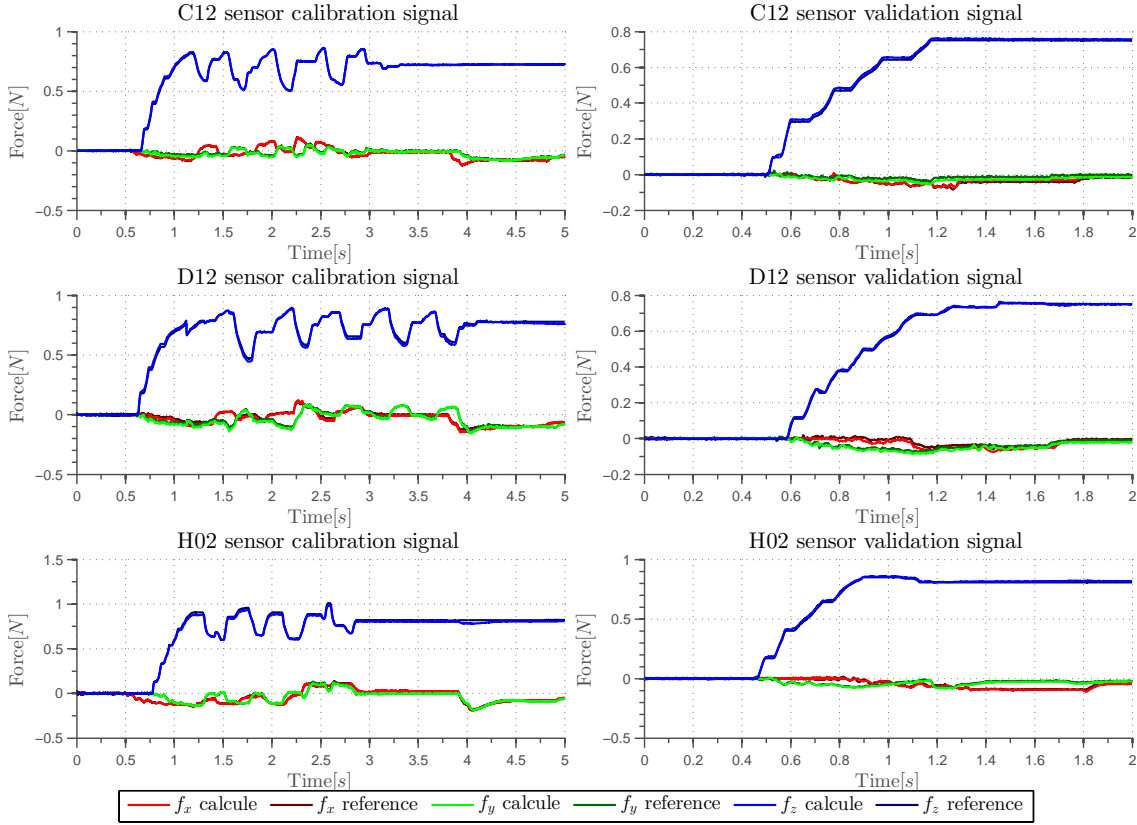


Figure 1.14: Results of the sensor characterization

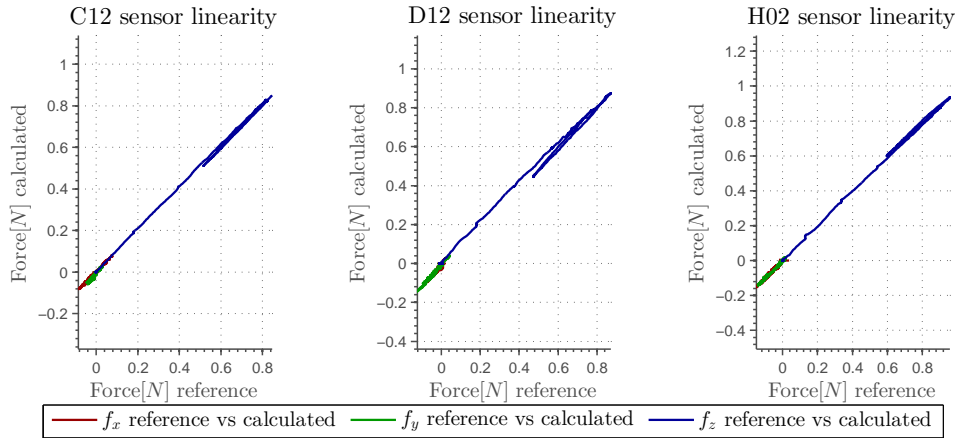


Figure 1.15: Graph of linearity

by a step function in the system input. Since no speed or acceleration of the actuator is known. The system transfer function is calculated using these signals based on the characteristic transfer function of a second order over-damped system as follows.

$$\frac{f_z(p)}{f_{z\text{real}}(p)} = \frac{K_p}{(1 + T_{p1}p)(1 + T_{p2}p)} \quad (1.25)$$

The values  $K_p$ ,  $T_{p1}$  and  $T_{p2}$  are found for each sensor. These values can be calculated in different ways. For example, by the method of Harriot for over-damped second order systems, or by minimizing the error between the input and output. We used the System Identification toolbox of MATLAB in order to easily determine these values. The computed values are :

	Measure	Mean error	Max error	Standard deviation
C12	$f_x$	-3.12 mN	23.20 mN	6.27 mN
	$f_y$	6.89 mN	26.82 mN	5.37 mN
	$f_z$	-5.67 mN	15.70 mN	4.31 mN
D12	$f_x$	4.83 mN	22.23 mN	5.89 mN
	$f_y$	3.19 mN	24.16 mN	4.74 mN
	$f_z$	-331.06 $\mu$ N	16.24 mN	4.03 mN
H02	$f_x$	2.29 mN	28.47 mN	5.66 mN
	$f_y$	3.25 mN	17.42 mN	4.24 mN
	$f_z$	-9.30 mN	22.72 mN	5.88 mN

Table 1.2: Error statistics sensor

C12	D12	H02
$K_P = 1$	$K_P = 1$	$K_p = 1$
$T_{p1} = 0.001936$	$T_{p1} = 0.001965$	$T_{p1} = 0.0018377$
$T_{p2} = 0.001985$	$T_{p2} = 0.002019$	$T_{p2} = 0.0018376$

The acquired signals of force and the calculated model are shown in Figure 1.16

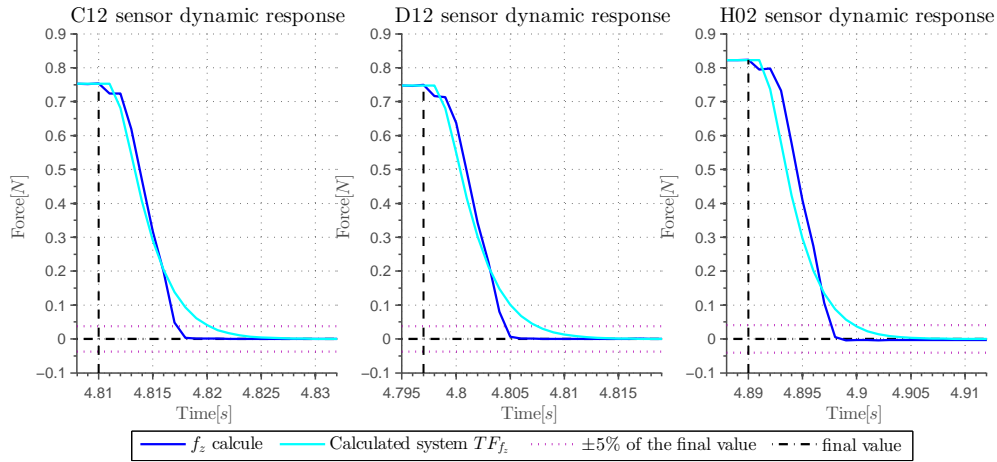


Figure 1.16: Dynamic response of the sensor when the exerted forces are released

### 1.3.4 Analysis of the results

Figure 1.14 and table 1.2 shows a high matching of the estimated forces in respect to the reference ones, with a maximum measured error of 28.47 mN with standard deviation about  $\approx 5$  mN. The reference system maximum error is 24.85 mN. Its standard deviation is 6.07 mN. Thus, it is possible to admit that the proposed sensor itself doesn't have a higher error than the reference system. A more precise reference could be used in order to get a more precise idea about the sensor precision.

The Figure 1.15 shows a linear behavior and a low hysteresis of the sensor. Unfortunately, the tangential forces exerted in this experiment are small since the surface of the epoxy added to the sensor is smooth and no enough friction was generated during the movement.

Bode diagram computed from the second-order systems presented in Figure 1.16, are shown in Figure 1.17

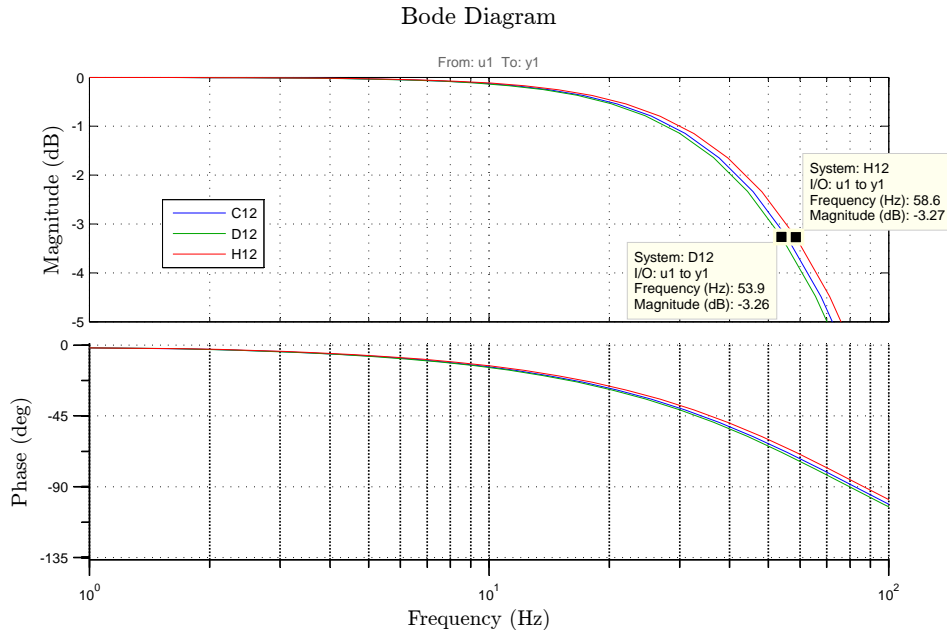


Figure 1.17: Frequency response and phase of the force sensors

The modeled behavior of the sensors shows a cut-off frequency about 55 Hz. The modeled performance of the sensors to a step signal is shown in Figure 1.18

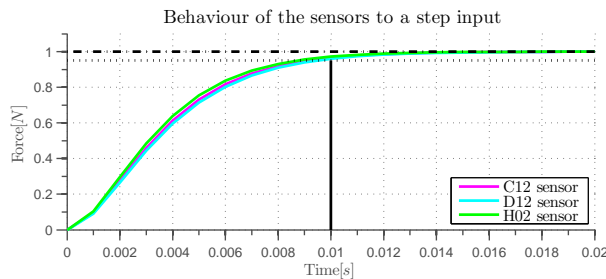


Figure 1.18: Behaviour of the force sensors to a step input

The modeled settling time for the three different systems for a step input of 1 N newton is 10 ms.

The three sensors showed very similar characteristics. This leads to the conclusion that the sensor manufacturing process is well controlled, the sensor is reliable and its behavior is repeatable.

## 1.4 Coating of the 3-axis force sensor

This section deals with the protection and of the 3-axis force sensor. Additionally, the protected system is characterized.

This section is divided in four subsections: First subsection describes the five different protections of the sensor made by coating in order to be compared. Second section describes the

method use to characterize the protected sensors. The third subsection shows the characterization of the protected systems. Finally the results of the characterization are shown and the conclusions are made.

### 1.4.1 Coating process

In order to protect the sensor and increase its sensitivity range, it is decided to protect the sensor in a similar way as shown in [Db10]. The protection is made by depositing an elastic material over the sensor so that the forces exerted on the material will be distributed between the sensor and its surrounding area leading to an increase in the maximum supported force at the price of decreasing the sensor resolution. But since the resolution of the bare sensor is already high, a good compromise can be made and the resulting sensor can still have a good resolution while resisting to greater forces.

The chosen elastic material is the polyurethane. This choice is entirely based on previous works results in determining the proper type of protection [Db10]. Following the same PCB mounting procedure shown in section 1.3.1, several protections were tested. In this document, 5 protections are considered as shown in figure 1.19

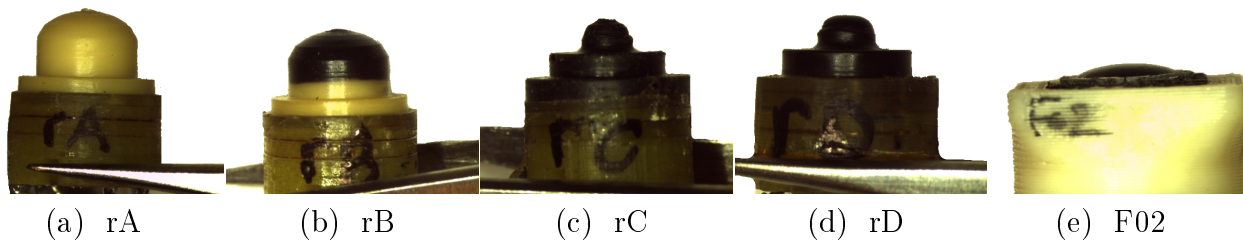


Figure 1.19: Conditioned coated sensors

These sensors were chosen to be tested in order to determine the following points:

- Which material should be used?  
The sensors are protected with two different polyurethane resins. The difference between the two tested materials is essentially in the hardness :
  - the black polyurethane has a hardness of Shore 80
  - the beige polyurethane has a hardness of Shore 40

The sensors rC, rD and F02 are protected with black polyurethane, rA with beige polyurethane, and the sensor rB is composed of half of each.
- What is the influence of coating height?  
Sensors rC and rD have the same shape, the same material but different height in order to establish a relationship between the coating height and the response of the sensor.
- What is the influence of the shape?  
Differences in behavior between the forms of protection.
- What is the best way to create the coating?  
Sensors rA, rB, rC and rD are made from a mold, and the protection F02 by pouring the material above the sensor



To easily manipulate the sensor, the support presented in the section 1.3.1 is used. Another support has also been created in order to handle round shaped PCB as shown in Figure 1.20.



Figure 1.20: Sensor placed on support

### 1.4.2 Coated sensor characterization

The same characterization used in section 1.3 has been applied to the coated sensors. Neglecting the non-linearity effects due to the coating, the equation  $\vec{f}' = \mathbf{S} \cdot (\vec{u} - \vec{b})$  describes the behavior of sensor. Here, the vector  $\vec{b}$  (in  $V$ ) is the bias. The matrix  $\mathbf{S}$  (in  $N/V$ ) is the sensitivity matrix. It transforms the voltage of the sensor  $\vec{u}$  into force  $\vec{f}'$  while taking into consideration the coupling effect caused mainly by the coating of the sensor.

### 1.4.3 Characterization results of the coated sensors

The force exerted during characterization of the coated sensors is about 1.3N. At least two measures of each axis for each of the five mentioned sensors were made at a frequency of 1000 Hz, the acquisition system is shown in Appendix A.2.1. As in the previous section, half measures is used to calculate the sensitivity matrix, and the other is used to validate the calibration.

In figure 1.21 the results of the experiments are shown in the same format as in section 1.3.

The table 1.3 presents the error statistics between the reference system and the three axis force sensors.

The graphics of the relation between the reference forces against the calculated forces are shown in figure 1.22. Here, the characteristics of linearity and hysteresis of the coated sensor are presented.

The system response have been studied exactly as presented in section 1.3.3. The signals and the modeled system response are shown in Figure 1.23.

As can be deduced from Figure 1.23, sensors rA and rB have a transfer function that fits with a second order transfer function 1.25. The other three sensors have a well pronounced relaxation phenomenon. The behavior of these sensors can be modeled by the function 1.26.

$$\frac{f_z(s)}{f_{z\text{real}}(s)} = \frac{a_1s + a_2}{s^2 + a_3s + a_4} \quad (1.26)$$

### 1.4.4 Result analysis and conclusions

From Figure 1.21 and table 1.3, it is clear that sensors rA, rB and rD have a similar behavior and good matching of the estimated forces in respect to the reference ones. However, sensors

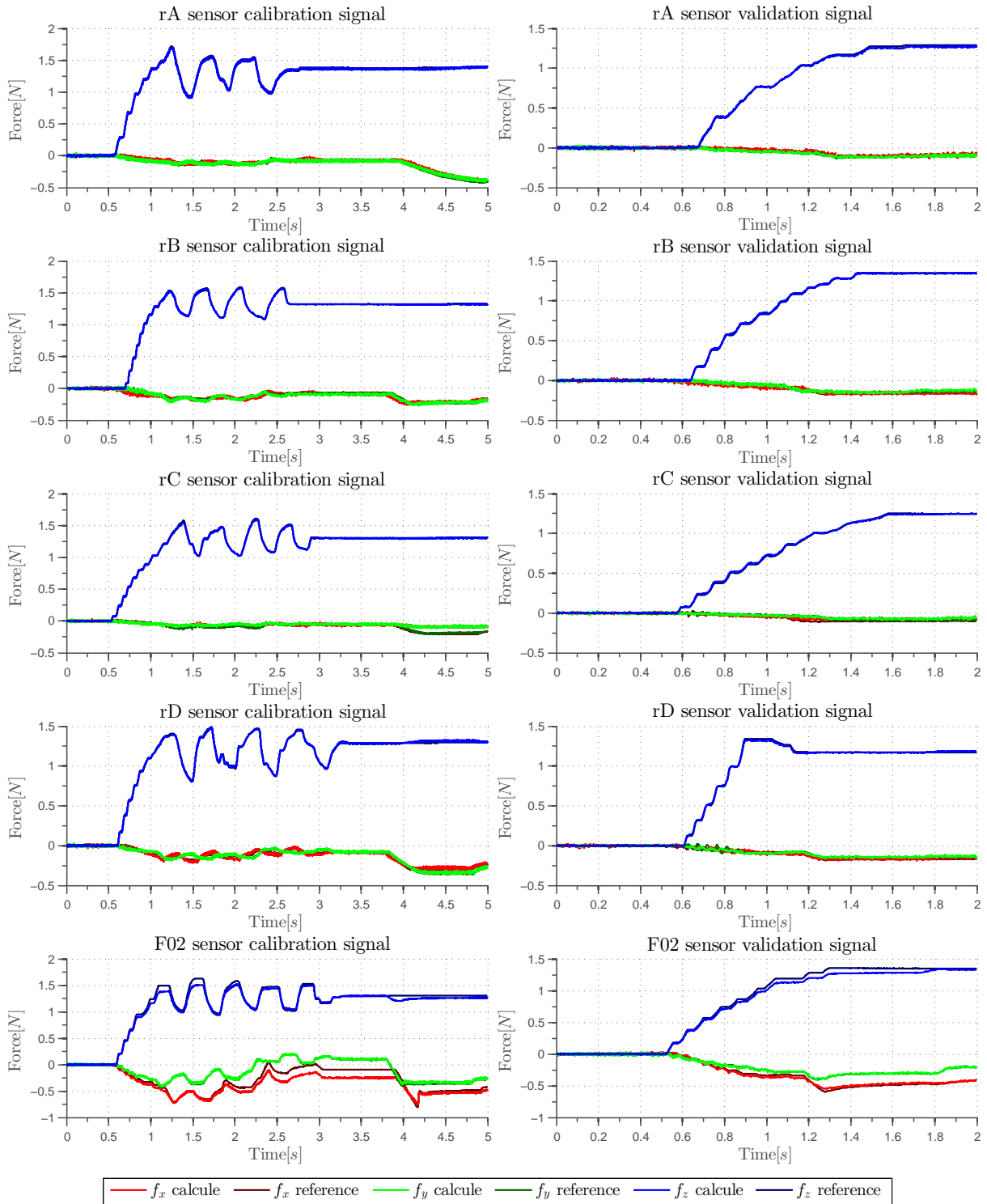


Figure 1.21: Results of the coated sensor characterization

rC and F02 have errors that are almost double compared to the others. Comparing tables 1.2 and 1.3, it is obvious that, in all cases, the coating has increased the error statistics compared to the unprotected sensors.

Figure 1.22 shows that sensors rA, rB and rD preserve the linear behavior between measurements.

Figure 1.23 shows that the sensors rC, rD and F02 have a non-negligible relaxation phenomenon.

	Measure	Mean error	Max error	Standard deviation
rA	$f_x$	-3.36 mN	46.31 mN	11.82 mN
	$f_y$	-8.44 mN	65.00 mN	15.67 mN
	$f_z$	13.89 mN	52.78 mN	11.98 mN
rB	$f_x$	-2.09 mN	64.19 mN	12.78 mN
	$f_y$	9.29 mN	70.34 mN	16.56 mN
	$f_z$	3.90 mN	33.42 mN	7.79 mN
rC	$f_x$	-19.85 mN	133.14 mN	40.70 mN
	$f_y$	-24.37 mN	144.11 mN	35.92 mN
	$f_z$	5.82 mN	37.65 mN	8.19 mN
rD	$f_x$	-3.77 mN	54.34 mN	18.17 mN
	$f_y$	-2.87 mN	51.63 mN	11.92 mN
	$f_z$	-1.52 mN	31.25 mN	11.56 mN
F02	$f_x$	72.81 mN	190.33 mN	63.86 mN
	$f_y$	-10.53 mN	69.15 mN	16.67 mN
	$f_z$	28.94 mN	135.17 mN	40.19 mN

Table 1.3: Error statistics coated sensor

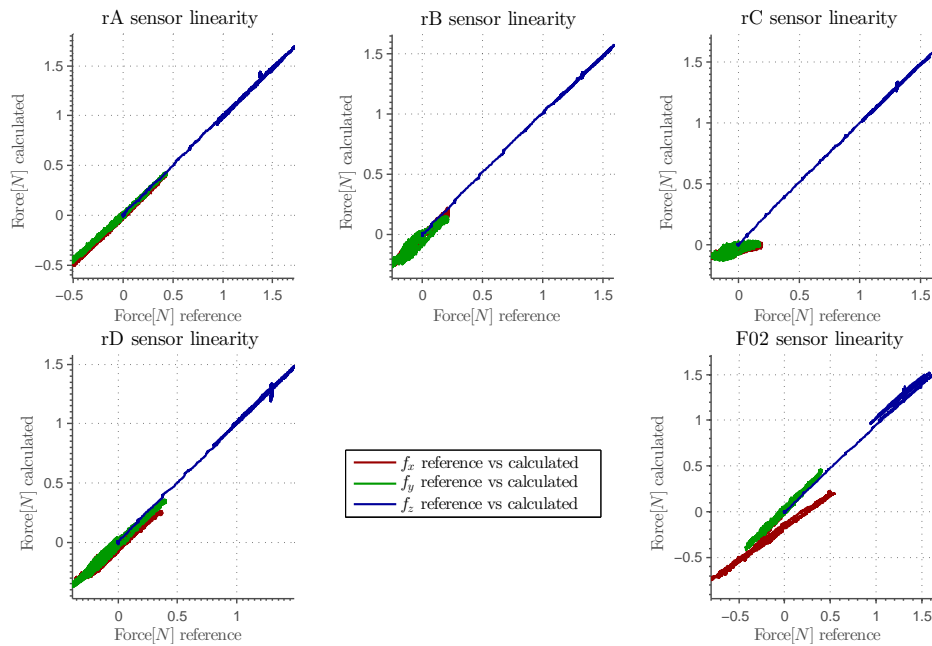


Figure 1.22: Graph of linearity of the coated sensors

Bode plot, calculated from systems presented in Figure 1.23, are shown in Figure 1.24.

The modeled cutoff-frequency of the sensors vary between about 30 Hz for the F02 and about 50 Hz for the rB. The theoretical performance of the sensors to a step signal is shown in Figure 1.25.

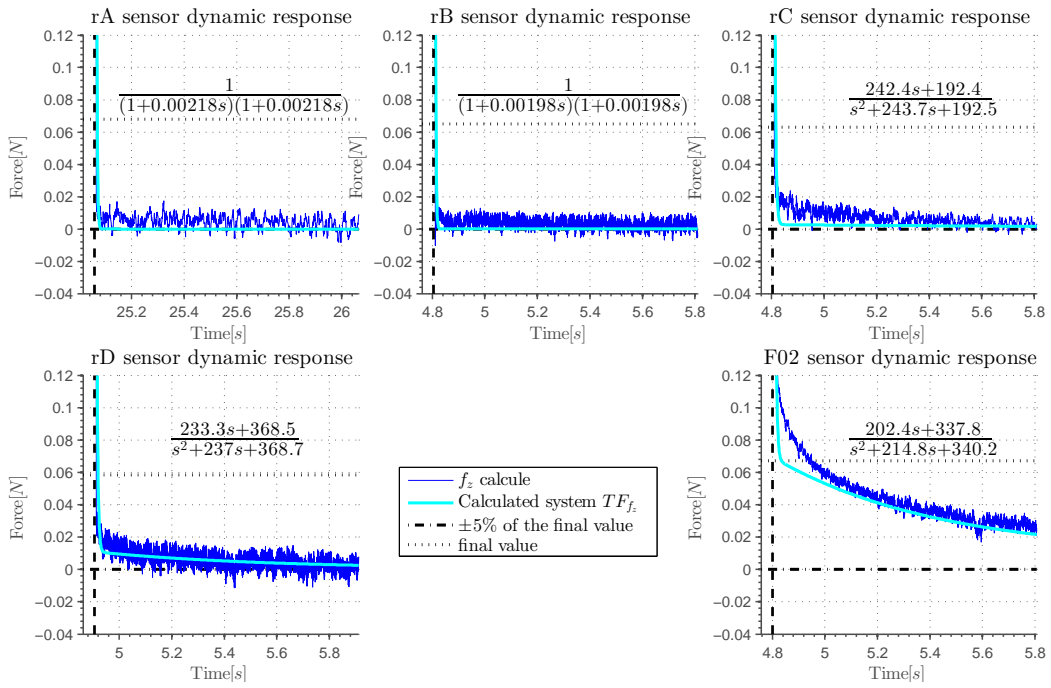


Figure 1.23: Dynamic response of the coated sensor when the exerted forces are released

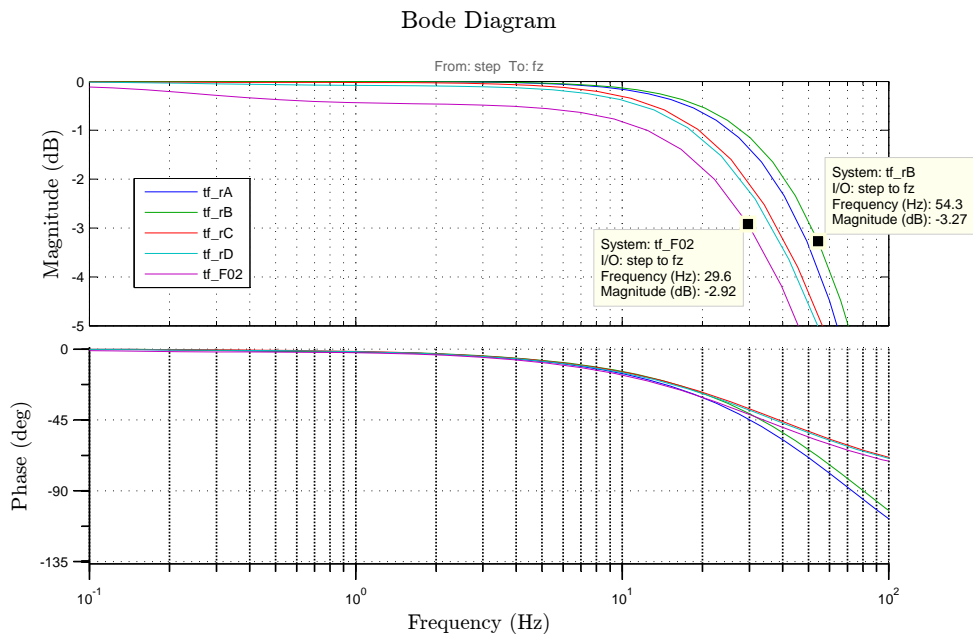


Figure 1.24: Frequency response and phase of the coated force sensors

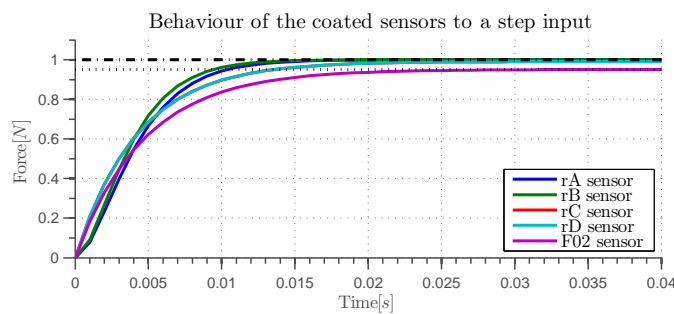


Figure 1.25: Behaviour of the coated force sensors to a step input

## 1.5 Resistance to high forces test

In this section the protected sensors are tested to measure the dynamic range. The goal of this test is to verify whether the coating preserves its characteristics for the range needed for object manipulation (about 10 N).

The coated sensors that present the best characteristics (rA and rD) are selected for the high force test. The test consists of repeating the same experiment presented in the previous section by applying a higher force range. The test bench system does not allow more than 9 N. In this test, at least 8 N was applied to the sensor. The results are shown in Figure 1.26.

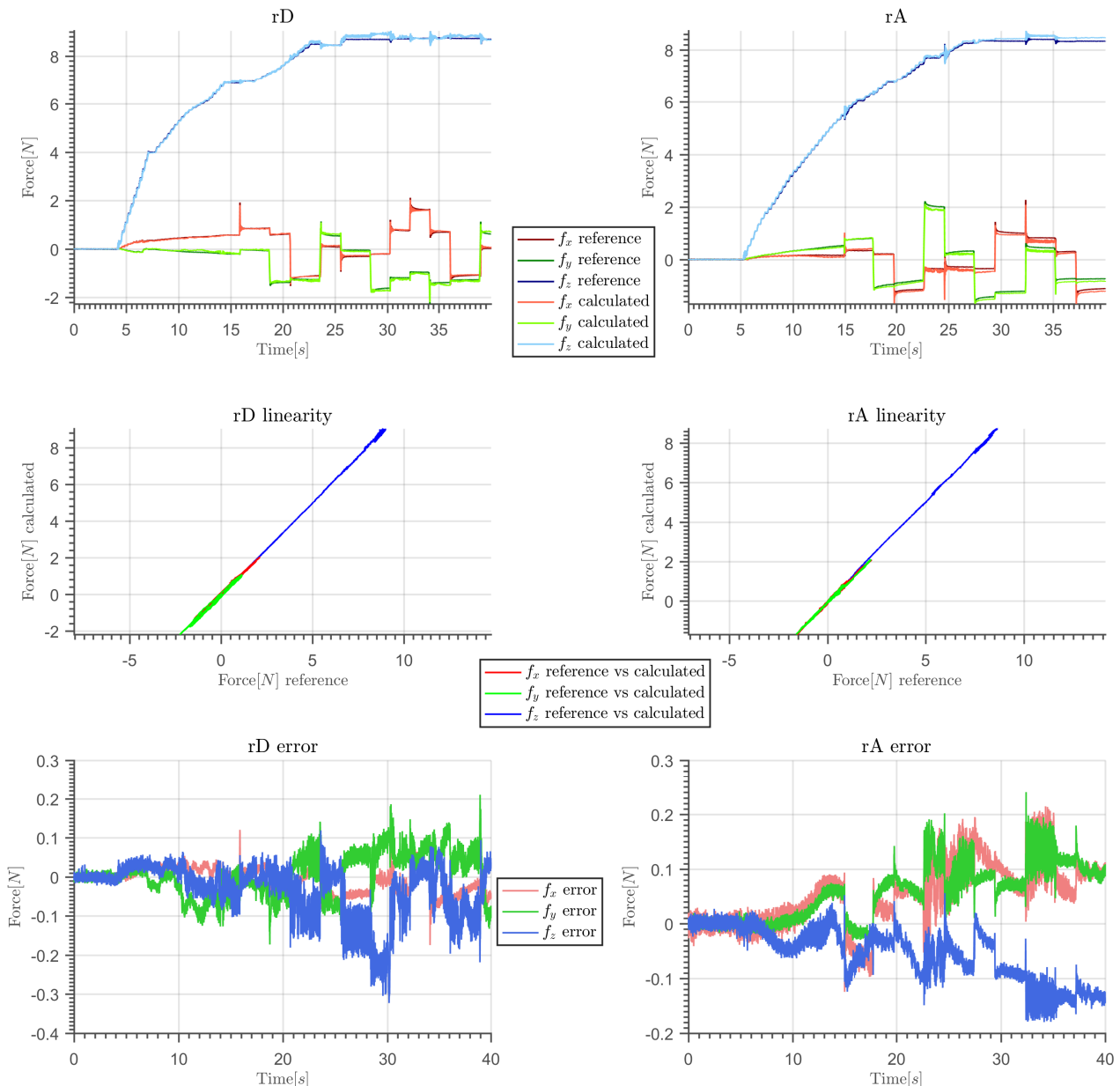


Figure 1.26: Results of the selected coated sensors

The figure shows that the sensors preserve their characteristics such as the linearity for the whole range of tested forces. The two systems resisted about 9 N without breaking. Clearly, they could go beyond this range without any problems. After the experiment, no hysteresis

was noticed nor was there a change in their sensitivity. A more robust test bench tool could be used to determine the maximum supported force.

## 1.6 Conclusion

This chapter presents an experimental procedure for designing a suitable coating for MEMS based 3-axis force sensors. Five different coatings with different shapes, sizes and materials were calibrated, tested and characterized in order to show the effect of the coating. The analyzed characteristics were the statistics of error in time, the linearity of the response as well as the impulse response of the system and the final sensitivity of the sensor.

The two sensors with the best characteristics are tested in a larger range showing that this type of coating is desirable for the protection of MEMs force sensors.

Regarding the set-points evoked in section 1.4, the following analyses are provided:

### **Coating Material : polyurethane Shore 40**

For the beige polyurethane with hardness of Shore 40, the relaxation phenomenon isn't considerable as is shown in Figure 1.21. Sensors coated directly with this material have a better dynamic behavior (rA and rB). When two materials are combined as for the sensor rB, the problem is that the forces are not distributed evenly in all directions (as shown in the linearity analysis figures).

### **Influence of height: A higher coating leads to lower sensor sensitivity to tangent forces**

Sensors rC and rD have the same shape and the same material. However they have very different behaviours. The bigger coating height in sensor rC reduces its sensitivity to tangential forces.

### **Influence of the shape: The shape must be symmetrical, and centered with respect the center of the sensitive area, the tip of the protection must be pointy to assure the that the forces are applied in this zone**

Three different basic shapes were tested. The coating used in rA and rD has the same best linearity. Those shapes gave the best results. The shapes of sensors F02 and rC have a wide base. This significantly decreases their sensitivity in the shear axes. One of the biggest problems of the coating shape used for the F02 is that the point where the forces are applied is not centered with the sensor.

### **Manufacturing type of protection: The coating should be created by molding**

The point of application of forces in the sensor must be well defined. The F02 sensor does not satisfy this condition. In fact, during the hardening process of the polyurethane, any disturbance in the angle affects the central point position.

The proposed guidelines can be used to create new coatings, with different range of forces and sensitivities. Consequently the force MEMs sensors can be applied in a larger set of applications.



# Intrinsic tactile sensing systems based on an array of 3 axis force sensors

---

## Contents

---

<b>2.1</b>	<b>State of the art . . . . .</b>	<b>30</b>
2.1.1	Tactile sensing . . . . .	30
2.1.2	Human tactile sensing . . . . .	30
2.1.3	Artificial tactile sensing . . . . .	33
2.1.4	Tactile sensing classification . . . . .	35
2.1.5	Theory of intrinsic measurements . . . . .	38
2.1.6	Conclusion . . . . .	40
<b>2.2</b>	<b>Intrinsic tactile sensing feasibility test . . . . .</b>	<b>40</b>
2.2.1	Design and assembly of the system . . . . .	40
2.2.2	Touch parameters estimation . . . . .	42
2.2.3	System calibration . . . . .	44
2.2.4	Accuracy analysis . . . . .	45
2.2.5	Tactile system validation . . . . .	47
2.2.6	Conclusion . . . . .	54
<b>2.3</b>	<b>Intrinsic tactile sensing system adapted to robotic finger implemen- tation . . . . .</b>	<b>55</b>
2.3.1	Design and construction of the system . . . . .	55
2.3.2	Touch parameters estimation . . . . .	58
2.3.3	Calibration method . . . . .	59
2.3.4	Experimental Set up . . . . .	60
2.3.5	Experimental results . . . . .	61
2.3.6	Conclusion . . . . .	63

---

## Context and motivations

In chapter 1, the coating of the 3-axis MEMs force sensor developed by the CEA-Leti was studied. An optimal coating has been chosen. At this point, the sensor is ready to be integrated in a robotic dexterous manipulation system. This chapter is dedicated to the design, characterization and test of a fully integrated tactile system based on the coated sensor.



## Chapter objective

The study of the integration of the 3-axis force sensor presented in chapter 1 in a robotic gripper intended for dexterous manipulation of objects.

## Outline of the chapter

This chapter is divided into three sections. The first section is the state of the art about tactile sensing systems. This section has the goal of guiding the research about to the best way to implement the 3-axis force sensor of chapter 1 in a tactile sensing system. With the conclusion and the system proposal of the first section, the second section is intended to prove and test the capabilities of the proposed tactile system. The last section is the creation of the proposed system for a robotic hand and the integration into a soft contact approach.

## 2.1 State of the art

This section gives an overview of tactile systems. It starts by a definition of tactile sensing. Followed by an explanation of the human tactile sensing system and its capabilities. Then, a short review of the history of artificial tactile sensing is given. Next, a classification of these systems is presented. Next, a specific focus on the intrinsic tactile sensing systems and the theory lying behind is made. The last subsection is a review of the existing sensors that could be used to create intrinsic sensing systems.

### 2.1.1 Tactile sensing

Frequently presented as a single sense, the human touch sense is, in fact, a combination of different senses. The human skin contains different sensing systems for measuring different physical properties. It is mainly divided into three groups: thermoception used to feel temperature of the object, mecanoception allows pressure sensing, and nociception which is responsible for pain sensing.

By definition, tactile sensing is a "system that can measure a given property of an object or contact event through physical contact between the sensor and the object". All properties that can be measured through contact, including the shape of an object, texture, temperature, hardness, moisture content, etc." [LN99] are considered.

### 2.1.2 Human tactile sensing

The human hand sensing capabilities were studied in robotic tactile sensing. The main object to learn the needed requirements for objects manipulation. In 1980 Harmon [Har80] proposed that the goal of tactile sensors is to achieve the same capabilities as humans. Dahiya affirms in his publication [Dah+10], that there is an "absence of any rigorous robotic tactile-sensing theory". Many surveys and papers about robotic tactile sensing as [How93] [YBA11] compares the systems with the human system characteristics. The human tactile sensing consists of three different senses, each of them have a different group of receptors distributed in the body in variable concentrations.

### 2.1.2.1 Mechanoception (Mechanoreceptors)

The mechanoreceptors are nerve cells that respond to mechanical interactions (pressure, vibration, deformation, etc.). There are four main types of mechanoreceptors in the human skin: Pacinian corpuscles, Meissner's corpuscles, Merkel's discs, and Ruffini endings, as shown in the figure 2.1. Each receptor has its own functionality. In [Dah+10] and [DN04], the authors present the capabilities of the human hand mechanoreceptors. Table 2.1 summarizes the characteristics of each mechanoreceptors.

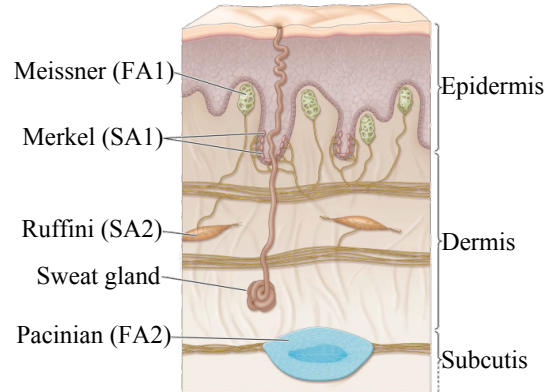


Figure 2.1: Cross section of the skin in the human hand [Wol06]

Receptor	Pacinian corpuscle	Ruffini Cor-puscle	Merkel Cells	Meissner's Cor-puscle
Type	FA II	SA II	SA I	FA I
Adaptation rate	Fast	Slow	Slow	Fast
Location	Dermis	Dermis	Epidermis	Epidermis
Stimuli frequency (Hz)	50 Hz – 1000 Hz	0 Hz – 15 Hz	0 Hz – 30 Hz	10 Hz – 60 Hz
Field diameter	3 mm – 4 mm	> 10 mm	3 mm – 4 mm	> 20 mm
Response threshold	0.54 mN	0.58 mN	1.3 mN	7.5 mN
Effective Stimuli	Temporal changes in the skin deformation	Sustained downward pressure; lateral skin stretch; skin slip	Spatial deformation; Sustained pressure; Curvature, edge, corners.	Temporal changes in skin deformation
Sensory function	High frequency vibration detection; dynamic texture; tool use	Finger position; Stable grasp; tangential force; Motion direction	Pattern/form detection; texture perception; tactile flow	Low frequency vibration and motion detection; grip control; Tactile flow perception

Table 2.1: Mechanoreceptors, adapted from [Dah+10] and [DN04]

### 2.1.2.2 Thermoception (Thermoreceptors)

Thermoreceptors are sensory receptors that provide the information about changes in skin temperature. There are two types of thermoreceptors: warmth fibers and cold fibers. The distribution of cold and warmth fibers varies across the body surface. In 1997, Caldwell published an article [CTW97] describing the following characteristics:

- Thermal fibers detect rate of change of temperature rather than the absolute temperature.
- The surface of the finger is at about 32 °C under 'normal' conditions but can vary over a large range.
- The reaction time for cold sensations for a temperature drop of greater than 0.1 °C s<sup>-1</sup>, is 0.3 s – 0.5 s.
- The reaction time for hot sensations with a temperature rise of greater than 0.1 °C s<sup>-1</sup> is 0.5 s – 0.9 s.
- Thermoreceptors can sense rates of change of temperature as small as 0.01 °C s<sup>-1</sup> (0.6 °C min<sup>-1</sup>), i.e. relative temperature sensing is accurately measured. The rate of change required to elicit sensation is smaller if the skin temperature at the time of stimulation is close to 20 °C or 40 °C.
- For small areas of the skin, the temperature range that can be adapted is from 20 °C–40 °C i.e. most of the absolute range is adapted. Never the less, it cannot be accurately gauged. Changes are most noticeable above 30 °C and below 25 °C.
- Below 20 °C, there is a constant cold sensation (full adaption does not occur) which gives way to cold pain below 3 °C.
- Above 40 °C, there is a constant hot sensation that gives way to burning sensation pain above 48 °C.
- Thermal cold pain is produced at a threshold of 3 although some researchers have put the cold pain threshold as high as 15 °C.
- The spatial threshold for the cold stimuli is lower than that for warmth. Cutaneous sensation provides local information necessary for good task performance such as surface texture, slip detection, thermal conductivity safety and local stiffness.

### 2.1.2.3 Nociception (Nociceptors)

There are sensory receptors that transmit information about noxious stimulation that causes damage or potential damage to skin. There are two groups of nociceptors:

- A-delta fibers: Intermediate-sized, myelinated sensory nerve fibers (faster);
- C fibers: Narrow-diameter, unmyelinated sensory nerve fibers (slower).

### 2.1.3 Artificial tactile sensing

#### 2.1.3.1 History

Tactile sensing in robotics emerged in the 1970s as a result to the appearance of new applications that require the measurement of physical quantities related to the contact of two or more objects. In the beginning, researchers tried to find the different transduction methods for the tactile sensors and started to create prototypes, for which, the main application was robotics.

The first researcher to review the robotic tactile sensing, was Harmon [Har80], in the early eighties. He proposed a definition for this term as "the continuous-varying sensing of forces in an array".

As this technology began to develop, several authors suggested that the robotic tactile sensors has to match the capabilities of the human sense of touch [DDR85]. The targeted application was multi-fingered robotic hands. Consequently the researchers proposed new methodologies for the development of tactile sensors, as well as new signal processing techniques [Jac+88].

Around 2000, new different types of touch sensors emerged and tactile sensing was redefined by [LN99] as "tactile sensor is a device or system that can measure a given property of an object or contact event through physical contact between the sensor and the object. We consider any property that can be measured through contact, including the shape of an object, texture, temperature, hardness, moisture content, etc".

Some authors proposed using tactile sensors in areas like medicine or agriculture. Some researchers created special sensors for minimal access surgery (or minimal invasive surgery) [DN04]. One great success of tactile sensing was tactile screens present today in all tablets and most smart phones.

The new miniaturization and packaging technologies of force sensors allowed producing sensors with better characteristics and smaller sizes.

A lot of research have been conducted on this subject producing hundreds of publications. Among them, several surveys and reviews such as [Dah+10] and [YBA11] were dedicated to reporting the history of tactile sensing as well as classifications of different types of sensors.

#### 2.1.3.2 Tactile sensors : Design guidelines

Human hand is the main tool to manipulate objects. Therefore, most of works in the field of robotic tactile sensing systems did focus on the characteristics of the sense of touch in human hand. Articles like [YBA11] and [Dah+10] have studied the characteristics of tactile sensors needed to achieve robotic dexterous manipulation of objects.

The general design criteria for tactile systems adapted from [Dah+10], [YBA11] and [Lee00] is presented as follows:

- Parameters to be measured: the pressure, the tangential force, torque, temperature, the distribution of forces, the point of contact, slip, texture, etc.
- Sensing surface: it can be a small area like fingerprinting, or a large surface as the palm of the hand.
- Spatial resolution: the minimum distance at which the sensor can differentiate some property (e.g. the distance between an applied force and other).

- Sensitivity range: the range in which the sensor can measure the physical quantity (e.g. 1 N – 10 N).
- Dynamic range (the ratio between the largest and smallest possible values of a changeable quantity): (e.g. 1000 measures for 1 N or 1000 : 1N).
- The resolution (the smallest change that can be detected in the measured entity): 1 mN.
- Response profile (the response of the sensor has to be identified): it can be of various types, linear or not, with or without hysteresis, stable, accurate, etc.
- Time response or frequency (how often the sensor measures) : typical frequency is around 1KHz.
- Stability (the degree to which sensor characteristics remain constant over time).
- Repeatability (the variation in measurements of the sensor, measuring the same quantity of a physical quality).
- Area of suitable use is the area or surface in one object that will interact with other objects.
- Integration and fabrication (the cost and production parameters of the sensor).
- Robustness.

### 2.1.3.3 Required characteristics of tactile sensors for dexterous manipulation

Based on the human hand characteristics, authors have found the required characteristics of the tactile sensing system to be adapted for dexterous manipulation. Table 2.2 present a summary of these characteristics.

Table 2.2: Summary of needed tactile sensor characteristics for dexterous manipulation (Adapted from [Dah+10], [YBA11], [Lee00])

Parameter	Guidelines
Parameters to be measured	three components of force, three components of torque, the distribution of forces, the point of contact, multi-touch, slip and texture
Sensing surface	all the hand with special attention to the fingerprints
Spatial resolution	1 mm – 2 mm in the fingerprint, and 5 mm in palm of the hand
Sensitivity range	0.01 N – 10 N
Dynamic range	100 : 1N (0.01 N
Response profile	Linear, stable, low hysteresis, large bandwidth, accurate.
Repeatability	Good
Area of suitable use	Fingerprints and exterior of a multifingered robotic manipulator (depends in the robotic task)
Integration and fabrication	Soft surface, simple mechanical integration, low power, low cost
Robustness	Withstand application, electronic and magnetic shielding

### 2.1.4 Tactile sensing classification

Tactile sensing systems can be classified in many ways : according to the measured parameters, the resolution, the sensitive area size, type of transduction technology... In this work, tactile sensing systems are classified into extrinsic, intrinsic and hybrid tactile systems.

#### 2.1.4.1 Extrinsic tactile sensing

The human skin is an example of extrinsic tactile systems. Such systems measure directly the force applied on their surface. Many artificial extrinsic tactile systems have been developed in the last thirty years. Commercial products ranging from the simplest pressure sensor placed on the surface of the system to the much more complicated arrays of touch sensors are available. This type of sensors have been developed with great success. There are companies like [Pre] and [Wei] that have a large offer of this type of systems as shown in figure 2.2. However, those systems do not measure tangential forces, nor do they measure the torque.

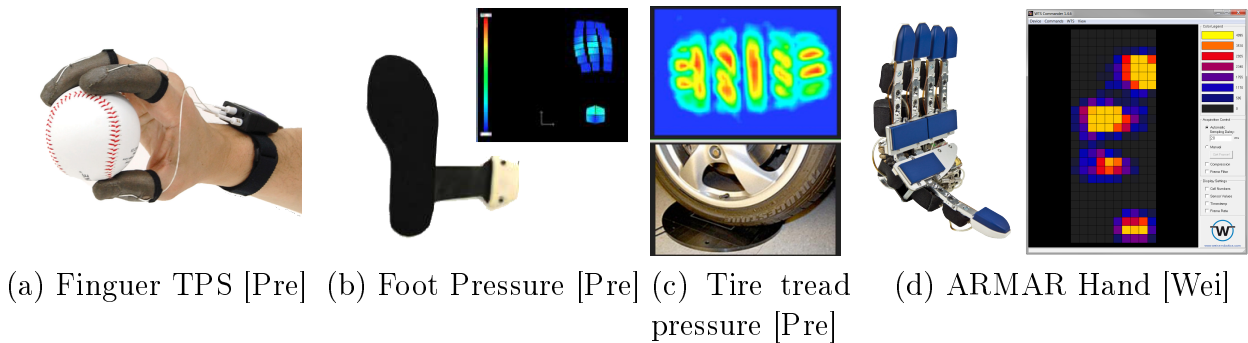


Figure 2.2: Motor and sensory homunculus

Some systems like [Lee+08] and [CPD11] are still in experimental status and do allow tangential forces measurement as presented chapter 1. Those systems are based on 3-axis force sensor arrays. This kind of system is able to measure all the parameters proposed in subsection 2.1.3.3. However, as shown in chapter 1, those systems have to be protected to assure the measure range. Besides, in order to respect the required spatial resolution, each sensor of the array must have a size of at most 2 mm by 2 mm. Given the size of human finger, the number of sensors may be large, which raises issues linked to the management of information stream and makes this system very difficult and expensive to implement.

**Using the 3-axis array force sensor CEA-Leti:** It should be noted that the sensor array used by [CPD11] and calibrated by [Alc+13] was also developed by the CEA-leti. This device, as presented in [Alc+13] has a maximum normal force of 80 mN, 25 times smaller than the 3-axis force sensor presented in chapter 1 without protection. As seen in figure 2.3, the signal management for a robotic finger with this array can be difficult. For those reasons, this system was not used as the transducer in this work.

**CEA-Leti 3-axis force sensor as extrinsic system:** The 3-axis force sensor presented in chapter 1 is not suitable for extrinsic applications, the single sensor is too big to respond to the 2mm spatial resolution and creating a dense array of this sensor suffers from the signal management problem.

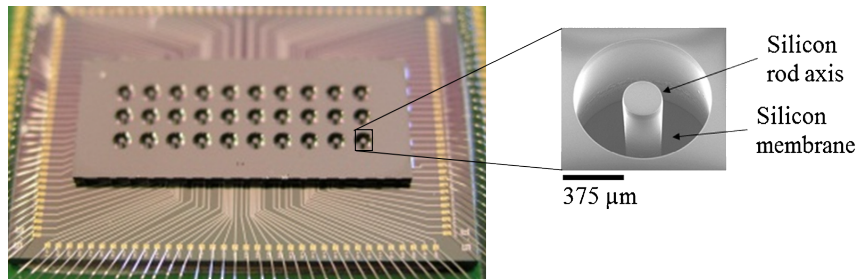


Figure 2.3: Array of 3-axis force sensor of [Alc+13]

### 2.1.4.2 Intrinsic tactile sensing

In intrinsic tactile sensing systems, the sensor is not placed directly on the touch surface. The tactile system estimates the position of the resultant forces and torques applied on a given surface from the measurements of force and torque in the supports of this surface.

In the late sixties, a tactile system able to calculate the position of the applied forces on a flat surface from forces over 3 or more pressure sensors was patented [For]. Later, a tactile system composed of a surface supported by a single six-axis force/torque sensor, under soft finger contact considerations was proposed in [BSB93]. The authors called it intrinsic tactile sensing.

Intrinsic tactile sensors can be integrated in two different ways. Either the sensor is part of the finger structure [ZSL96],[Son+12](see Figure 2.4-a), (i.e. the finger was designed with the sensor), or the sensor is externally attached to the finger [Bat+16] (see figure 2.4-b).

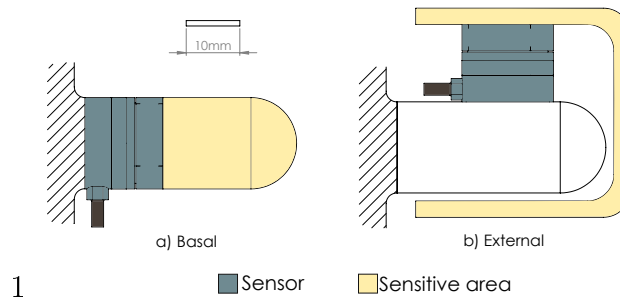


Figure 2.4: Different configurations to locate the ATI sensor in a robotic finger

The major limitation of this system is that, no matter where the sensor is located (see Figure 2.4), all the forces and torques are applied on this single sensor. Since torque increases with distance, a single sensor may break with small forces if they are applied far enough. All the mentioned systems [ZSL96],[Son+12] and [Bat+16] use the AtiNANO17 [Ati] sensor, because it is the only sensor in the market sufficiently robust, small and precise for application intended to designing actuators of the size of a human finger. Therefore, lately, alternatives to this type of sensors such as [Mel+14], [Sar+12] [DMNP12] and [Dao+01] have been developed. They are all based on a single centralized 6-axis force-torque sensor.

The concept of multiple sensors is reconsidered in publications such as [Vis+10], [HTA10]. This approach enables the use of larger contact surfaces. For example, the floor of a room [Vis+10], or a whole-body haptic sensing system [HTA10].

The concept can be generalized to  $k$  sensors. Limitless sensor distribution configurations can be imagined. Figure 2.5 presents two possible configurations for a robotic finger with  $k = 3$ .

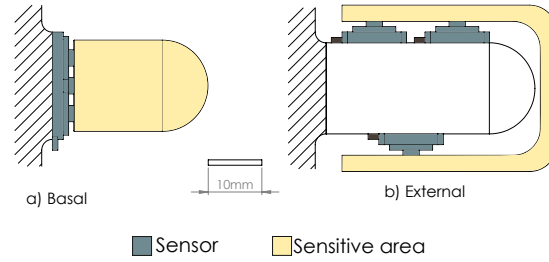


Figure 2.5: Two sensors configurations of three 3-axial force sensors for a robotic finger

When comparing figures 2.4 and 2.5, the space advantage gained by the option of multiple external MEMS based sensors is evident.

**3-axis force sensor CEA-Leti as intrinsic system:** The 3-axis force sensor presented in chapter 1 is suitable for intrinsic applications. The single sensor has good linearity and hysteresis properties and could be easily implemented in any surface.

### 2.1.4.3 Hybrid tactile sensing

Hybrid systems combine intrinsic and extrinsic techniques. For example, the main commercial tactile system of Syntouch called BioTac [Syn] (see figure 2.6) has an internal pressure system that can intrinsically measure the pressure exerted on a surface through a liquid. At the same time, the device measures the pressure distribution extrinsically by an array of electrodes. This device can also estimate the direction of shear forces by the difference of pressure in the electrodes made by the deformation of the external layer. This system has been implemented in a hand with three fingers. It could estimate all the parameters required to achieve dexterous manipulation. But only the normal force exerted on the system is accurately measured. The shear forces and positions are very rough estimates.

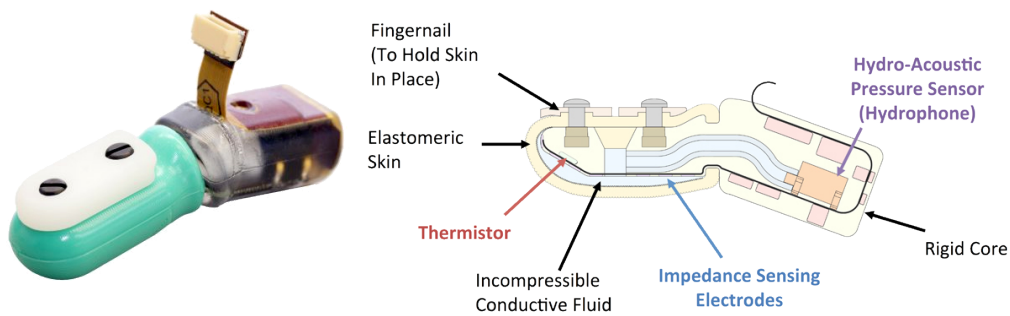


Figure 2.6: Biotac commercial system

Another intrinsic/extrinsic hybrid system is presented in [CM05] and [CM06] (see figure 2.7). The support of this system is a 3-axis force sensor that measures intrinsically, the normal and tangential forces. The distribution of forces is measured extrinsically by an array of electrodes. The main problem of this system is that it is not able to estimate the torque acting on the surface.

A perfect hybrid tactile system could be designed in order to match all the parameters required for dexterous manipulation of objects. The intrinsic part should enable the measurement of the three components of the net force, and the three components of the net torque applied on



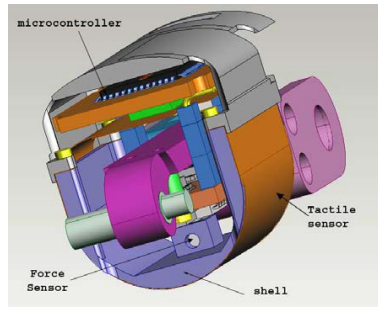


Figure 2.7: Hybrid system by [CM06]

the contact surface. The extrinsic part should measure the pressure distribution on the touch surface.

## 2.1.5 Theory of intrinsic measurements

### 2.1.5.1 Single sensor

In 1993, Bicchi presented a system with a defined surface attached to a 6 axis force/torque sensor [BSB93], as shown in figure 2.8. The sensor is located in the reference frame  $B$ . The measured forces and torques are respectively the vectors  $\vec{f}$  and  $\vec{m}$ .

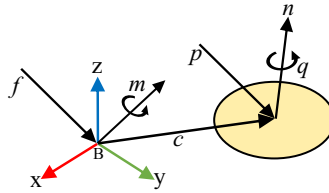


Figure 2.8: Intrinsic measure from six-axis force/torque sensor

The resultant of forces and torques applied onto the surface are respectively the vectors  $\vec{p}$  and  $\vec{q}$ . The vector pointing from the center of the sensor  $B$  to the contact centroid is  $\vec{c}$  (see Soft Finger Contact and the Contact Centroid subsection in [BSB93] for complete definition). From this system, the following relations are deduced:

- The surface of the object is represented by equation 2.1 where  $r$  is a point in space defined respect to the reference frame  $B$ .

$$S(\vec{r}) = 0 \quad (2.1)$$

- The sum of forces and torques is assumed to be static because the measurement interval is too short in comparison to the exerted forces dynamics and long enough compared to the interface dynamics, therefore:

$$\vec{f} = \vec{p} \quad (2.2)$$

$$\vec{m} = \vec{q} + \vec{c} \times \vec{p} \quad (2.3)$$

- The torque vector can only be perpendicular to the surface. This is due to the fact that the torque in a contact can only be created by force pairs thanks to friction:

$$\vec{n} \propto \vec{q} = \frac{K}{2} \nabla S(\vec{c}) \quad (2.4)$$

where the vector normal to the surface is  $\vec{n}$  and  $K/2$  is a scale factor.

By replacing the equations (2.2) and (2.4) in the equation (2.3), the problem is reduced to four non-linear equations with four unknowns. In [BSB93], the authors found two different ways to solve those equations in order to determine  $\vec{p}$ ,  $\vec{q}$  and  $\vec{c}$  from  $\vec{f}$ ,  $\vec{m}$  and  $S(\vec{r})$  :

- Solve the equations analytically with certain restrictions on the shape of the surface.
- Solve the equations numerically by an iterative method without restrictions on the shape of the surface.

### 2.1.5.2 Multiple sensors solution

In this section, the concept presented in [BSB93] is extended to the multi-sensors case (i.e. the sensitive surface is connected to more than one fixed sensor as shown in figure 2.9). Let  $k$  be the number of sensors. Each sensor is connected to the surface at a position  $l_i$  in the frame  $B$ . Assuming that a couple force/torque is applied on a point  $c$  on the surface, each sensor will receive a part of the applied force and torque depending on its position relatively to the point  $c$ .

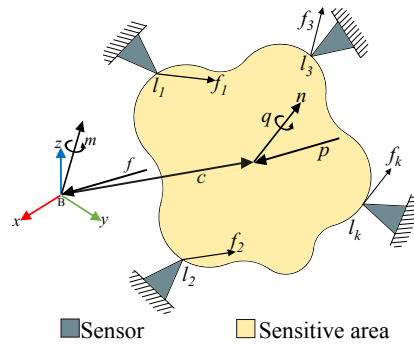


Figure 2.9: Intrinsic measure from multiple sensors

In the case  $k = 1$ , the system is exactly the same as proposed by [BSB93] and a 6-axis sensor is required. If  $k = 2$ , the system will require at least two sensors that measure the three components of force and only one component of the torque (the torque on the axis formed by a line linking the two sensors). If  $k = 3$ , only non aligned 3-axis sensors are required. It is possible to use more than three 3-axis sensors in order to enhance the robustness of the system or to increase the size of the sensitive surface. It is also possible to have a combination of three 3-axis sensors and other pressure, force or torque sensors to enhance the overall sensitivity of the system.

The transition time induced by the elasticity of the material of the surface is assumed to be negligible. In this case two new relations can be derived :

$$\vec{f} = \sum_{i=1}^k \vec{f}_i \tag{2.5}$$

$$\vec{m} = \sum_{i=1}^k \vec{l}_i \times \vec{f}_i \tag{2.6}$$

By substituting these equations in equations (2.2) - (2.3), it is possible to reuse the resolution method proposed in [BSB93] to solve this problem. In this case, the system has to determine  $\vec{p}$ ,  $\vec{q}$  and  $\vec{c}$  from  $\vec{f}_i$ ,  $\vec{l}_i$  and  $S(\vec{c})$ .

### 2.1.6 Conclusion

To integrate the 3-axis force MEMs sensor presented on chapter 1 on the fingertips of a robotic manipulator, the best option is to create an intrinsic tactile system. As shown in this section, the intrinsic tactile systems can measure most of the parameters required for dexterous manipulation of objects except for the pressure distribution. In the other hand an extrinsic system can be used in a hybrid system in order to overcome this problem.

Therefore, after reviewing the theory of intrinsic tactile sensing, this chapter presents an intrinsic tactile system used to verify the capabilities of this kind of system with an array of 3-axis MEMS force sensors. Then, an intrinsic tactile system is created to be implemented in a robotic hand including a soft surface.

## 2.2 Intrinsic tactile sensing feasibility test

In order to test the feasibility of an intrinsic tactile sensing system based on an array of 3-axis MEMS force sensors, this section shows a first test of a tactile system design with three 3-axis force sensors, reusing the protected sensors of the chapter 1.

This section is divided in six subsections: First subsection describes the design of the tactile system using three 3-axis force sensors and a structure created by a 3D printer. Second subsection shows the mathematical model used to estimate the contact parameters. Third subsection is dedicated to the calibration of the tactile system. In the fourth subsection, an accuracy analysis of the system is made. The objective is to determine the minimal force strength to be applied on the system required for estimating the position of contact accurately. In the fifth subsection, the tactile system is tested and validated. Finally results are analyzed and conclusions are made.

### 2.2.1 Design and assembly of the system

This section deals with the design and assembly of the intrinsic tactile system based on an array of 3-axis force sensors. The system is created with the coated sensors presented in the chapter 1.

### 2.2.1.1 Design

This system is intended to prove and test the capabilities of multi-sensor intrinsic sensing concept. Thus, the simplest surface form (flat) and the least number of required three-axis force sensors (three) have been used. In the end, a tactile system based on three 3-axis force sensors distributed on a flat surface has been designed as shown in Figure 2.10.

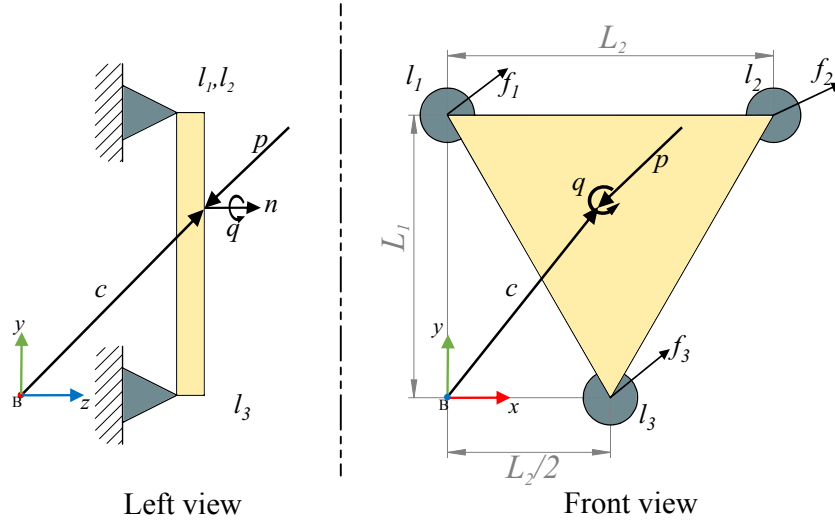


Figure 2.10: Tactile system configuration for the flat surface tactile sensor

The sensitive area is a lightweight flat surface linked onto three MEMS based 3-axis force sensors. Let the  $z$  axis of the reference frame be the vector normal to the sensitive surface. In this case, the equation of the surface is simplified to :

$$S(\vec{r}) = r_z - h = 0 \quad (2.7)$$

where  $h$  is the relative height of the touch surface plane with respect to the reference frame  $B$  and  $\vec{r}$  is a point from the touch surface. It is possible to apply a 3D force on the touch surface at any contact point of the plane described by  $S(\vec{r}) = 0$ . Here, if the contact is not punctual, the centroid of the contact area is assumed to be the contact point. In the particular case of a flat surface, only torques along the  $z$  axis (perpendicular to the touch surface) can be applied to the system. Indeed, to apply a torque to the surface, friction is needed. The forces involved in friction are parallel to the contact surface, which means that the resulting torque can only be normal to this surface. Since the surface is flat, the torque is along the  $Z$  axis.

### 2.2.1.2 Assembly

For this prototype, coated sensors are used. A simple assembly of coated sensors was made to rapidly create the system. The three sensors used in this system have been coated with the coating reference rC (as shown in previous section). The conclusions of the previous section placed this coating as the second best coating. Due to availability problems, the best coating was not used for this system. The rC coating was mainly chosen for its availability.

Each sensor is held by a support. The supports are attached by screws to a rigid plate as shown in figure 2.11. Each support has a clamp-type mechanism which ensures that the sensor does not move.

The dimensions of the system are expressed by  $L_1 = 60$  mm and  $L_2 = 55$  mm as shown in figure 2.11. Tactile system parts are built using a 3D printer with a resolution of  $250 \mu\text{m}$ .

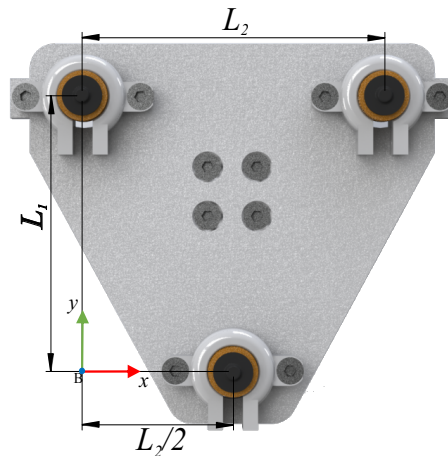


Figure 2.11: Top view of the base with the sensors

The three sensors have an apparently equal height. A rigid plate is glued to the upper end of the sensors as shows figure 2.12.

The system is designed to be modular in order to be able to easily replace the sensitive surface to test different types of surfaces. This is made possible by three screws that can connect the plate to the desired surface.

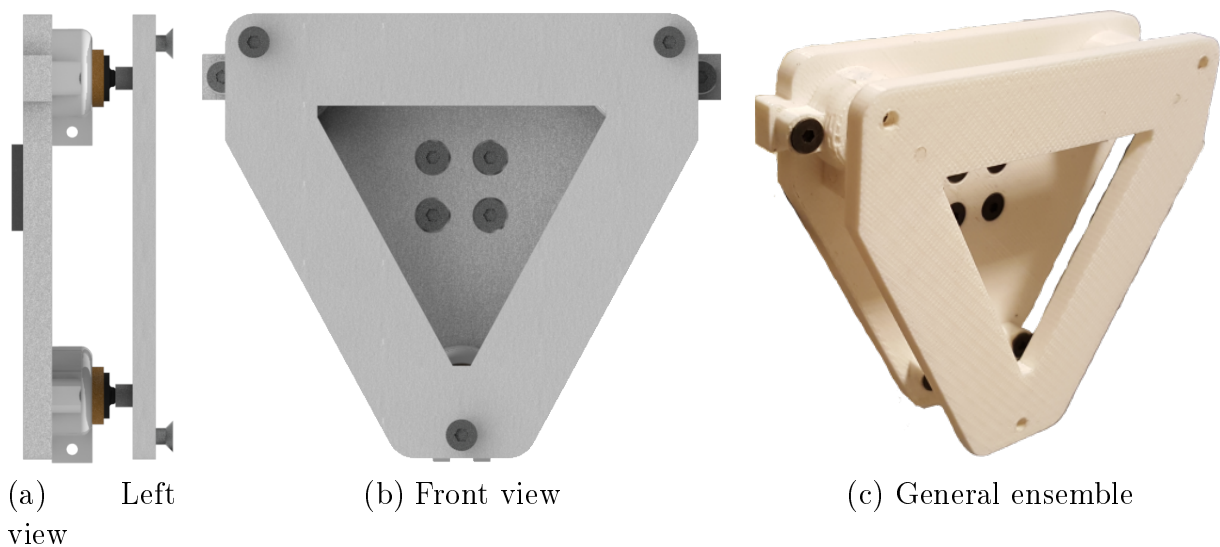


Figure 2.12: Flat surface system

The four screws located in the center of the base are used to fix the base to the reference system described in appendix A.1.2.

### 2.2.2 Touch parameters estimation

The touch parameters that can be estimated by this system are :

- Touch contact centroid position  $\vec{c}$

- Total applied force  $\vec{p}$
- Total applied torque  $\vec{q}$

In the particular case of the flat surface, the touch position has only two components  $c_x$  and  $c_y$  (because of the system geometry,  $c_z = h$ ), and the torque has a single component along  $z$  axis (as  $q_x = q_y = 0$ ). From equation 2.4, the scale factor is  $K = -2q_z$ . Thus the parameters to be estimated are :

- Touch contact position  $c_x, c_y$
- Total applied force components  $p_x, p_y, p_z$
- Total applied torque on the  $z$  axis  $q_z$

For each time sample  $t_i$ , the signals provided by the three sensors ( $\vec{u}_1, \vec{u}_2, \vec{u}_3$ ) are digitized. A low-pass filter is applied on the measured voltages in order to reduce the noise. The cutoff frequency of this filter is 50 Hz, the same cutoff frequency of the coated sensors. Then, by substituting equations (2.5), (2.6) and (2.7), in (2.2), (2.3) and (2.4) respectively, the system is reduced to 6 equations with 6 unknowns :

$$\vec{p} = \vec{f}_1 + \vec{f}_2 + \vec{f}_3 \quad (2.8)$$

$$\begin{bmatrix} 0 \\ 0 \\ q_z \end{bmatrix} + \begin{bmatrix} c_x \\ c_y \\ 0 \end{bmatrix} \times \vec{p} = \vec{f}_1 \times \vec{l}_1 + \vec{f}_2 \times \vec{l}_2 + \vec{f}_3 \times \vec{l}_3 \quad (2.9)$$

To obtain the force measurements  $\vec{f}_1, \vec{f}_2, \vec{f}_3$ , two operations are required. First a sensor calibration must be applied to obtain force values from the voltages :

$$\begin{bmatrix} \vec{f}'_1 \\ \vec{f}'_2 \\ \vec{f}'_3 \end{bmatrix} = \begin{bmatrix} \mathbf{S}_1 & 0 & 0 \\ 0 & \mathbf{S}_2 & 0 \\ 0 & 0 & \mathbf{S}_3 \end{bmatrix} \begin{bmatrix} \vec{u}_1 - \vec{b}_1 \\ \vec{u}_2 - \vec{b}_2 \\ \vec{u}_3 - \vec{b}_3 \end{bmatrix} \quad (2.10)$$

where the offset vectors are  $\vec{b}_1, \vec{b}_2$  and  $\vec{b}_3$ . The sensitivity matrices are  $\mathbf{S}_1, \mathbf{S}_2, \mathbf{S}_3$ . Then, the sensors measurements must be put in the same reference frame  $B$  as follows:

$$\begin{bmatrix} \vec{f}_1 \\ \vec{f}_2 \\ \vec{f}_3 \end{bmatrix} = \begin{bmatrix} \mathbf{R}_1 & 0 & 0 \\ 0 & \mathbf{R}_2 & 0 \\ 0 & 0 & \mathbf{R}_3 \end{bmatrix} \begin{bmatrix} \vec{f}'_1 \\ \vec{f}'_2 \\ \vec{f}'_3 \end{bmatrix} \quad (2.11)$$

where  $\vec{f}_i$  is the real force,  $\mathbf{R}_i$  is the rotation matrix between the frame of reference and the frame of the sensor  $i$ , and  $\vec{f}'_i$  is the force measured by each sensor expressed in its local frame.

The model describing the relationship between the measurements and the parameters to be estimated can be written in two different ways:

- The first model uses a non linear function that depends on the voltages measured by the force sensors:

$$\begin{bmatrix} p_x \\ p_y \\ p_z \\ c_x \\ c_y \\ q_z \end{bmatrix} = g \left( \vec{u}_1 - \vec{b}_1, \vec{u}_2 - \vec{b}_2, \vec{u}_3 - \vec{b}_3 \right) \quad (2.12)$$

- The second model applies a slight modification on the parameters to be estimated. This modification allows transforming the relationship expressed by equation 2.12 into a linear relation :

$$\begin{bmatrix} \vec{p} \\ c_x p_z \\ c_y p_z \\ q_z + c_x * p_y - c_y * p_x \end{bmatrix} = \mathbf{T} \begin{bmatrix} \vec{u}_1 - \vec{b}_1 \\ \vec{u}_2 - \vec{b}_2 \\ \vec{u}_3 - \vec{b}_3 \end{bmatrix} \quad (2.13)$$

where  $\mathbf{T}$  is a matrix of  $6 \times 9$  parameters. In this system, the applied force is directly estimated. The contact position as well as the torque can be deduced by combining the estimated parameters.

Both representations of the system require the positions of the sensors  $\vec{l}_i$ , the sensitivity matrices  $\mathbf{S}_i$  and the rotation matrix of each sensor  $\mathbf{R}_i$ , as well as the bias vector  $\vec{b}_i$ . Both models can be used to estimate the applied force  $\vec{p}$ , the contact position  $c_x, c_y$  and the torque  $q_z$ , from the sensors output tensions  $\vec{u}_1, \vec{u}_2$  and  $\vec{u}_3$ .

### 2.2.3 System calibration

As presented in the previous subsection, there are many parameters that must be known in order to be able to compute the touch parameters from the sensor's measurements. To do this, two different methods can be used:

- The first one consists in calibrating the sensors individually (estimate the sensitivity matrices  $\mathbf{S}_i$ ) before assembling the system and physically measure the geometric parameters  $l_i$  and  $\mathbf{R}_i$ . The bias is estimated using sensor's measurements when no load is applied to the assembled system. The main problem of this calibration procedure is that some of its parameters may change after the assembly. Typically, the sensitivity matrix can change after gluing the surface to the sensor which has an impact on the accuracy. Besides, if the system is assembled above a surface of unknown form, rotation matrices can be difficult to determine.
- The second way is to calibrate the system when it is already assembled. This requires a reference measurement of the applied force, torque and the touch position. It can be done in few steps: first, when no load is applied to the system, the offset vectors  $\vec{b}_1, \vec{b}_2$  and  $\vec{b}_3$  can be directly obtained from the output voltages of the tactile sensor system. This procedure removes all internal bias:

- the internal sensor bias;

- the bias produced by the coating;
- the bias produced by the gluing quality between the sensor coating and the touch surface;
- the effects of gravity on the touch surface.

After removing the bias, a force  $\vec{p}$  and torque  $q_z$  are applied on the surface at known locations  $c_x$  and  $c_y$ . The calibration aims to find the parameters values that minimizes the square of the error between the model (2.12 or 2.13) and the reference measurements.

In [HTA10], the authors used the first calibration method. The best average error they achieved is 7 mm.

### 2.2.3.1 Calibration using the linear model

Using the linear model simplifies the calibration process since all parameters to be estimated are contained in the matrix  $\mathbf{T}$  (see equation(2.13)). This matrix can be estimated using a least squares algorithm:

$$\mathbf{T} = \underset{\mathbf{T}}{\operatorname{argmin}} \sum_{i=1}^n \left( \operatorname{ref}_i - \mathbf{T} \begin{bmatrix} \vec{u}_1 - \vec{b}_1 \\ \vec{u}_2 - \vec{b}_2 \\ \vec{u}_3 - \vec{b}_3 \end{bmatrix}_i \right)^2 \quad (2.14)$$

where  $\operatorname{ref}_i$  is the reference measurement at sampling time  $i$ , and  $n$  the number of samples. This matrix contains the system dimensions  $l_i$  and the product of  $\mathbf{S}_i \cdot \mathbf{R}_i$ .

### 2.2.3.2 Calibration using the non-linear model

In the case of the nonlinear model, the calibration requires directly finding the system dimension parameters  $l_i$  and the product of  $\mathbf{S}_i \cdot \mathbf{R}_i$ . This calibration is done using a non linear mean squares minimization. The cost function is:

$$\{l_1, l_2, (\mathbf{S}_j \cdot \mathbf{R}_j)\} = \underset{l_1, l_2, \mathbf{S}_j \cdot \mathbf{R}_j}{\operatorname{argmin}} \sum_{i=1}^n \left( \operatorname{ref}_i - g \left( \begin{bmatrix} \vec{u}_1 - \vec{b}_1 \\ \vec{u}_2 - \vec{b}_2 \\ \vec{u}_3 - \vec{b}_3 \end{bmatrix}_i \right) \right)^2 \quad (2.15)$$

where  $j = 1, 2, 3$  is the sensor index.

## 2.2.4 Accuracy analysis

In the case of a flat surface perpendicular to the z axis, the force components  $p_x$  and  $p_y$  can only be generated by friction. Thus, it is possible to deduce from (2.9) that the position coordinates  $c_x$  and  $c_y$  are equal to:

$$c_x = \frac{-f_{1y}l_{1z} + f_{1z}l_{1y} - f_{2y}l_{2z} + f_{2z}l_{2y} - f_{3y}l_{3z} + f_{3z}l_{3y}}{p_z} \quad (2.16)$$

$$c_y = \frac{-f_{1x}l_{1z} + f_{1z}l_{1x} - f_{2x}l_{2z} + f_{2z}l_{2x} - f_{3x}l_{3z} + f_{3z}l_{3x}}{p_z} \quad (2.17)$$



If  $p_z = 0$ , the position cannot be computed. There is a minimum normal force value that enables the system to determine the touch position with the required accuracy. As shown in [Dah+10], the precision required to achieve dexterous robotic manipulation is around  $2mm$ . In order to find the minimum force required to achieve this precision, the sensitivity of the system must be computed. From equation (2.12), the position can be written as a function of the voltages  $\vec{u}_{1,2,3}$ . Let  $\Phi$  be the part of the function  $g$  that links the voltage measurements to the position  $\vec{c}$ :

$$\vec{c} = \Phi(\vec{f}_1, \vec{f}_2, \vec{f}_3) \quad (2.18)$$

The system sensitivity with respect to the position can be calculated analytically using the following formula:

$$\delta\vec{c} = \mathbf{J}_\Phi(\vec{f}_1, \vec{f}_2, \vec{f}_3) \cdot \delta(\vec{f}_1, \vec{f}_2, \vec{f}_3) \quad (2.19)$$

where  $\mathbf{J}_\Phi$  is the Jacobian matrix of the function  $\Phi$ . This function can be approximated to the resulting change in position from voltages as:

$$\Delta\vec{c} = \mathbf{J}_\Phi(\vec{f}_1, \vec{f}_2, \vec{f}_3) \cdot \Delta(\vec{f}_1, \vec{f}_2, \vec{f}_3) \quad (2.20)$$

where  $\Delta(\vec{f}_1, \vec{f}_2, \vec{f}_3)$  are the dynamic resolution of the 3-axis force sensor and the function  $\Phi$  and  $\mathbf{J}_\Phi$  can be calculated after calibration. To calculate the minimum required normal force, the function  $g^{-1}$  or  $\mathbf{T}^{-1}$  should be calculated or approximated:

$$(\vec{p}, c_x, c_y, q_z) \xrightarrow{g^{-1} \text{ or } \mathbf{T}^{-1}} (\vec{f}_1, \vec{f}_2, \vec{f}_3) \quad (2.21)$$

The theoretical voltage can be calculated from a known reference  $(\vec{p}, c_x, c_y, q_z)$ . The limits of our variables are:

$$-5N \leq p_x, p_y \leq 5N \quad (2.22)$$

$$\vec{c} \in \text{contact surface} \quad (2.23)$$

$$-100Nmm \leq q_z \leq 100Nmm \quad (2.24)$$

The limits of the calculated voltages can be deduced by applying the inequalities (2.22), (2.23) and (2.24) to equation (2.21). Finally, for different values of  $p_z$ , the function (2.20) is maximized (with constraints). The norm of the maximized function is the estimated maximum error given the normal force  $p_z$ .

As a matter of fact, a minimum normal force is required to calibrate the system, and a calibration is needed to calculate the required minimal normal force. To bypass this problem, an approximate sensitivity  $\mathbf{S}_i$  and rotation  $\mathbf{R}_i$  matrices as well as the system dimensions  $l_i$  have been used. The system dimensions have been measured manually, the rotations are approximated to identity, and each sensor default sensitivity  $\mathbf{S}_i$  has been used. Figure 2.13 shows the relationship between the maximum position error value as a function of the applied normal force  $p_z$ .

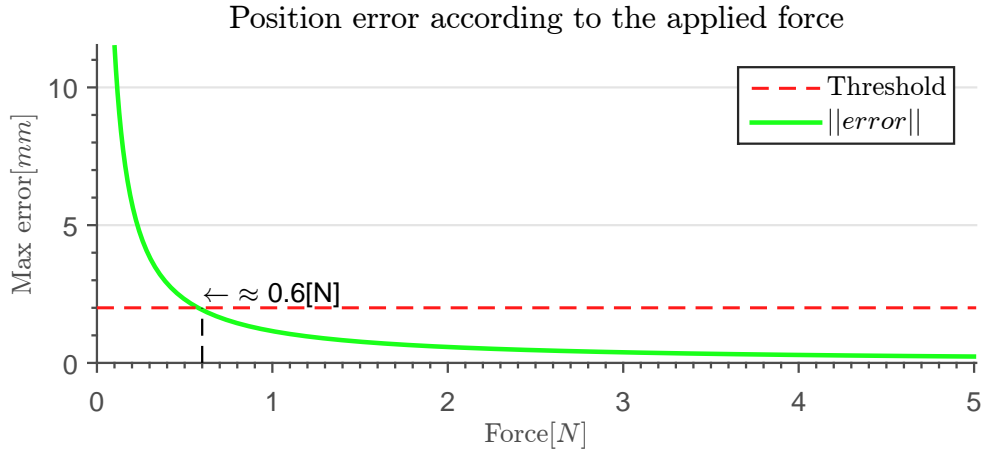


Figure 2.13: Minimal force applied with approximated calibration values

## 2.2.5 Tactile system validation

In this subsection, three experiments and their results are presented. These are made in order to calibrate the system and to test its accuracy. For each experiment, two sets of data are gathered. The first set is used to calibrate the system. The second set is used to validate the calibration.

In order to characterize and validate the developed tactile system, a testing assembly was created as shown in the appendix A.1.2. In this assembly, the support of the tactile sensing system is fixed to a reference force sensor. The sensor provides a reference measurement of the force  $\vec{p}$  applied on the surface of the tactile system. The standard deviation of the noise of the reference sensor is 10 mN.

Since this reference system does not have the position information in time, i.e. the reference of signal  $\vec{c}$  is unknown. Two different methods are developed: the first one is to reconstruct the position from the signal of force compared with the predefined path on motorized tables. This method is used in experiment 1. The second method is to fix several points of application of forces, as it is shown in experiment 2 and 3. With this reference system, the torque  $\vec{q}$  is also unknown. To be able to calibrate the system torque, the experiment 3 is proposed.

### 2.2.5.1 Experiment 1: force and position calibration

The experiment consists in reconstructing the position of contact and the contact forces from the sensors signals, having as reference the predefined path on motorized tables and a reference 3-axis force sensor.

#### Experimental Setup

A flat surface is placed on the tactile system through the three screws as shown Figure 2.14.

The forces  $\vec{p}$  are applied on the flat surface by a cone made of polyurethane. The cone tip is cut in order to obtain a planar surface of contact. This surface is a circle with a diameter of 1.5 mm. The cone can move in  $XY$  plane (X: horizontal, and Y: vertical) thanks to two motorized linear tables of the reference system.

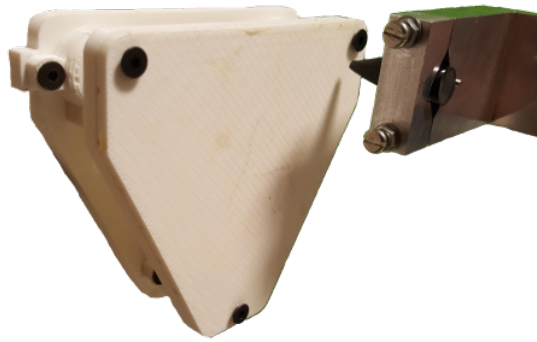


Figure 2.14: Setup of experiment 1

The testing process is performed as follows:

- The actuator (cone) is placed in the starting position of a predefined trajectory, and data acquisition is started.
- Precision screw is rotated, until approximately 1 N force is measured by the K3D40 along the Z axis.
- The actuator is moved on the surface following the defined trajectory.
- The motion of the actuator produces forces in the X and Y directions due to friction.
- At the end of the trajectory the contact is released and the acquisition of measurements stops.

Two trajectories are designed to test the system, as shown in Figure 2.15. The displacement speed of the contact point between the system and the actuator is  $2 \text{ mm s}^{-1}$ . When the actuator reaches each vertex of the trajectory, the motion stops for 4 s.

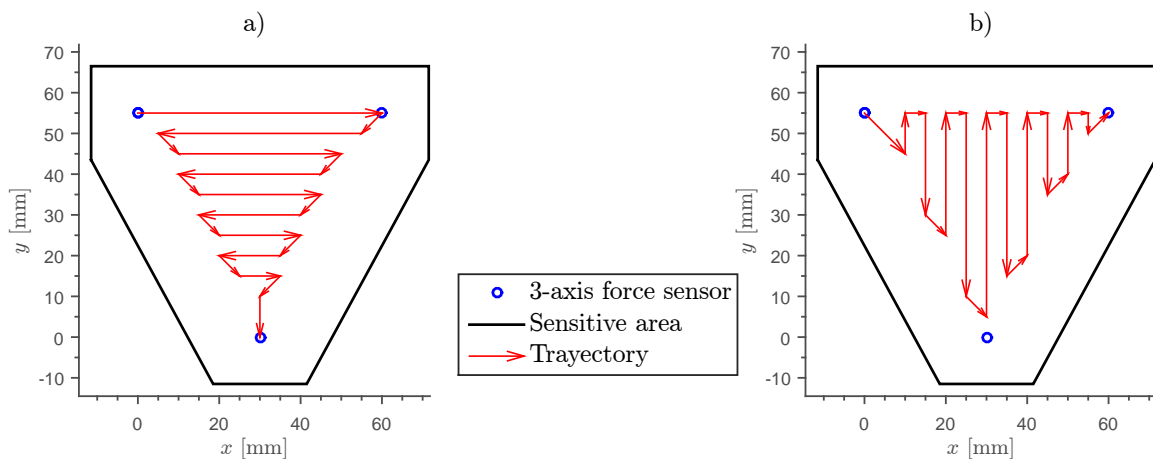


Figure 2.15: Trajectories used for sensor test

At the end of the experiment, two sets of position/force measurements are available:

- The reference measurements.
- The developed tactile system measurements.

This data is used to calibrate and determinate the precision of the developed system.

The measurements are made using the predefined trajectories presented in the previous section and in figure 2.15. The first one is used for the system calibration while the second allows checking the system accuracy. For this experiment, only the linear calibration is used. Once the system is calibrated, it is possible to use equation 2.13 to determine the parameters (i.e. the force  $\vec{p}$  and contact position  $\vec{c}$ ). Here the torque is null.

When the applied force is null (or very low), it is not possible to locate the contact point. For this reason, the estimation algorithm determines the tip position only when the normal component of the force ( $p_z$ ) exceeds a threshold. For the experiment, the threshold on the applied force has been set to 0.6 N, as the accuracy analysis shows it.

### Results

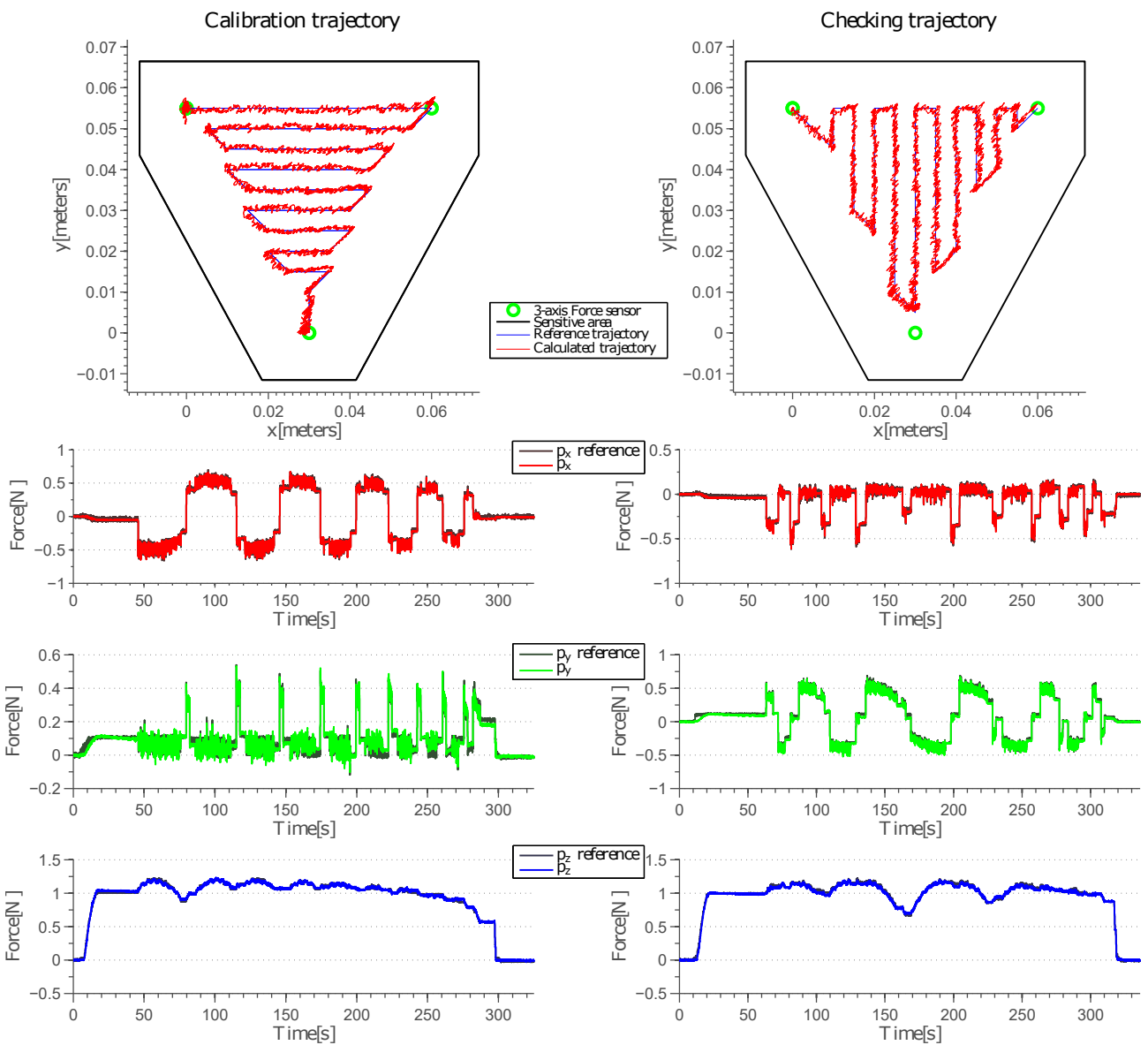


Figure 2.16: Experimental results of experiment 1

Table 2.3 presents the error statistics between the reference system and the developed tactile system.

Measure	Mean error	Max error	Standard deviation
$p_x$	8.18 mN	74.5 mN	17.6 mN
$p_y$	3.97 mN	67.8 mN	19.1 mN
$p_z$	-1.21 mN	67.7 mN	19.0 mN
$\vec{p}$	31.0 mN	89.9 mN	12.8 mN
$c_x$	28 $\mu\text{m}$	2.75 mm	0.52 mm
$c_y$	-96.5 $\mu\text{m}$	2.52 mm	0.54 mm
$\vec{c}$	0.661 mm	3.02 mm	0.37 mm

Table 2.3: Error statistics of experiment 1

### Results Analysis

The results of the first experiment (figure 2.16) show a high precision in estimating both force and contact position. The mean error for position estimation is about 0.7 mm (with standard deviation of 0.372 mm) which is lower than the spatial resolution required to achieve dexterous manipulation (see section 2.1.3.3). The mean error in force estimation is 31.9 mN (with standard deviation of 12.8 mN). The maximum error recorded in these tests was about 3 mm in position and 75 mN in force.

#### 2.2.5.2 Experiments 2 and 3

In these experiments, several points of application of forces have been fixed. With the reference in position fixed, the system can be characterized in force as shown the experiment 2 and torque as shown the experiment 3.

#### Experiment 2 setup: Static force and position calibration

The goal of the second experiment is to calibrate the system in order to get accurate static force  $\vec{p}$  and position  $c_x$  and  $c_y$  (no motion is involved). The surface of the sensing system is modified as shown in figure 2.17. This surface consists in a series of holes arranged in a matrix form. A screw can be fixed to each hole. Any force exerted on the screw will be applied within the circle formed by the cross section of the screw.

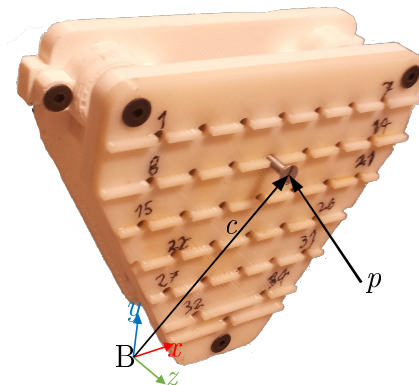


Figure 2.17: Setup of experiment 2

The experiment follows this protocol :

- Acquire sensor measurements and reference measurements for 3 seconds without applying any force.
- Fix the screw in a hole
- Apply a force manually on the screw head while acquiring both sensor measurements and reference measurements.
- Change the screw position, then repeat the experiment.

In the case of the linear model, this calibration enables finding the first 5 lines of the matrix  $\mathbf{T}$ . In the case of the non linear model, this calibration enables to determine the parameters of the first 5 nonlinear equations of the function  $g$ .

Tests have been made using both the linear and the non linear models. For each experiment, two sets of measurements have been made: the first was used to calibrate the system and the second was used to validate the calibration. The analysis made in section 2.2.4 is taken into consideration. Thus, the normal applied force  $p_z$  must be greater than 0.6 N during calibration.

### Experiment 3 setup: static torque calibration

The goal of the third experiment is to calibrate the system in order to get accurate torque  $q_z$ . Using the same surface created for the previous experiment, a stick is connected to the screw as shown in figure 2.18. A weight placed at the edge of the stick creates a torque depending on the force exerted by the weight  $p_y$  and the distance between the weight connection point and the center of the screw  $d_1$ .

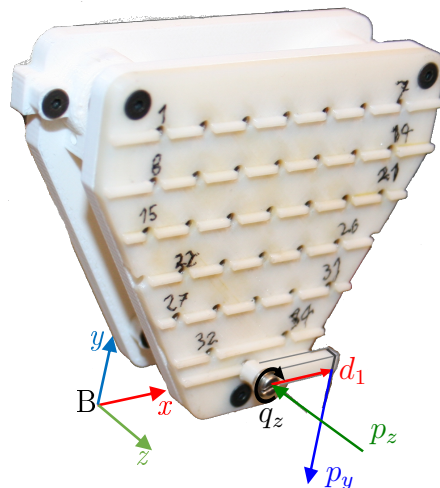


Figure 2.18: Setup of experiment 3

The experiment follows this protocol :

- Fix the screw and the stick in a hole.

- Fix the weight to the stick extremity in order to apply a torque on the screw and apply a force  $p_z$  of 1N on the screw. Acquire both sensor measurements and reference measurements.
- Change the screw position then repeat the experiment.

In the case of the linear model, this calibration enables finding the last line of the matrix  $\mathbf{T}$ . In the case of the non linear model, this calibration enables determining the parameters of the last nonlinear equation of the function  $g$ .

Experiments have been made using both the linear and the non linear models. Just like the previous experiments, two sets of measurements have been made for each experiment. The first was used for calibration and the second was used for validation. The applied force  $p_z$  was greater than 0.6 N during calibration.

### Results

Figure 2.19 presents the maximum touch position error through the surface as function of the applied normal force using both individual sensors calibration, and full system calibration. As in figure 2.13, for each force value, the maximum error on the entire surface is used.

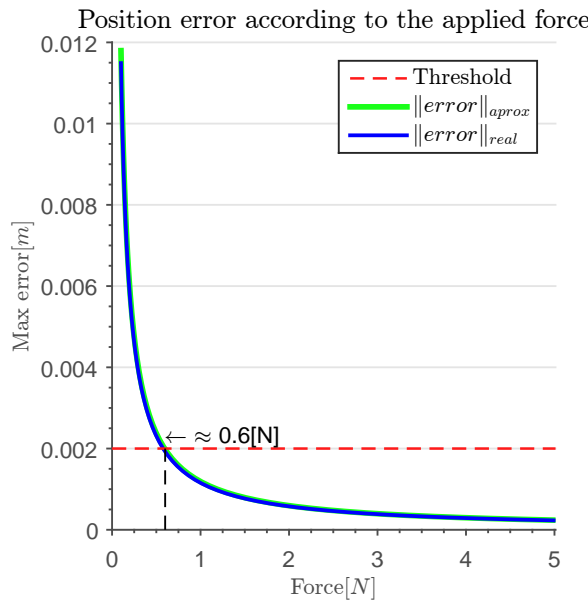


Figure 2.19: Minimal force applied with full system calibration

It is clear that the difference is very small between the minimal normal forces estimated using individual calibration and entire system calibration.

In figure 2.20 the results of the first experiment are shown. The left side of the figure presents the results for the measurement set used to calibrate the system. The right side of the figure presents the results for the measurement set used to validate the system.

Table 2.4 presents the error statistics between the reference system and the developed tactile system for both linear and nonlinear models.

Experiment 2 (Position and force estimation)

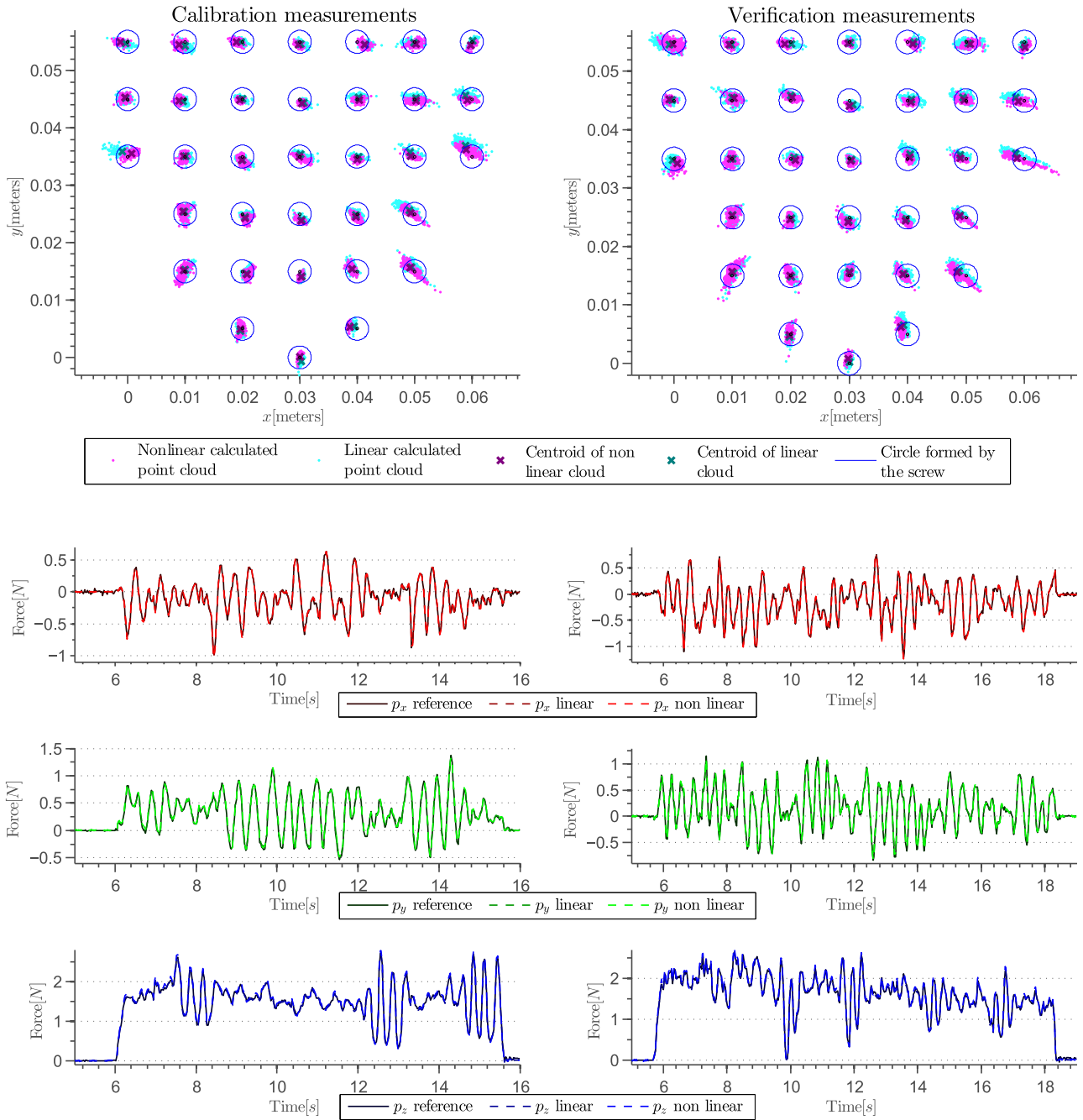


Figure 2.20: Experimental results of experiments 2 and 3

Result Analysis

The results of this experiment (figure 2.20) show a good matching of the estimated forces and the contact point with respect to the reference ones.



	Measure	Mean error	Max error	Standard deviation
nonlinear	$p_x$	-3.9 mN	200 mN	28 mN
	$p_y$	0.15 mN	150 mN	35 mN
	$p_z$	-1.0 mN	220 mN	38 mN
	$\vec{p}$	51 mN	370 mN	31 mN
	$c_x$	-0.26 mm	5.9 mm	0.82 mm
	$c_y$	1.7 $\mu$ m	3.3 mm	0.73 mm
	$\vec{c}$	0.93 mm	6.5 mm	0.58 mm
	$q_z$	52 $\mu$ N m	1.3 mN m	0.20 mN m
linear	$p_x$	1.8 mN	330 mN	28 mN
	$p_y$	1.8 mN	210 mN	34 mN
	$p_z$	-18 mN	180 mN	37 mN
	$\vec{p}$	51 mN	580 mN	32 mN
	$c_x$	-0.16 mm	4.7 mm	0.87 mm
	$c_y$	0.21 mm	4.7 mm	0.76 mm
	$\vec{c}$	0.99 mm	5.2 mm	0.67 mm
	$q_z$	-0.26 mN m	1.7 mN m	0.83 mN m

Table 2.4: Error statistics of experiments 2 and 3

The results for both models are quite similar. It shows a good precision in estimating force, position and torque. The mean error in estimating the position is about  $1mm$  (with standard deviation of  $0.6mm$ ) which is lower than the spatial resolution required to achieve dexterous manipulation. The mean error in estimating the force is  $50mN$  (with standard deviation of  $31.8mN$ ).

## 2.2.6 Conclusion

This section presented the design and implementation of an intrinsic tactile system based on three 3-axis force sensors. The system allows the estimation of the position, the force and the torque of a contact between an external object and the sensitive area of the system.

A specific configuration of the system has been studied and tested. The configuration consists in a planar distribution of sensors on which a triangular flat surface is glued.

Two different models of the system were presented : a linear model and a non linear model. The linear model is simpler to express and easier to calibrate. It has provided performances similar to those provided by the non-linear model.

The tests on different sets of data proved that the system calibration was well done and the achieved accuracy is within the precision required for dexterous object manipulation. Experiment 1 showed better results than the experiment 2. This is caused by the modified surface in the experiment 2. In fact, the applied tangential forces were not only caused by friction.

The torque calibration was inappropriate, because the applied torque have a direct relation with the applied forces in the y-axis. The best way to calibrate this system in with a 6-axis force-torque sensor and a reliable source of reference in position.

In this section, several facts have been neglected such as the weight of the screw and the stick

used to calibrate the system as well as the change in the z component of the touch position due to the screw length. All these factors could be removed by replacing the force sensor placed in the back of the system with a force-torque sensor and applying forces and torques using a mechanical system that guarantees a good knowledge of the touch position. Then, experiments 2 and 3 can be fused into one unique experiment in which all system parameters can be estimated at once.

The developed system structures was entirely made by a 3D printer. The silicon MEMS based 3 axis sensors was coated and glued to the surface manually. This process was quick and inexpensive. In addition, this system satisfies many of the characteristics presented in the requirements of tactile sensing presented in section 2.1.3.3:

- It can measure the three components of force, the perpendicular components of torque, and the position of the contact centroid;
- It provided a flat tactile sensing area of 4600 mm<sup>2</sup>;
- It has a sensitivity range between 50 mN and 10 N;
- It has a spacial resolution of 2 mm for 0.6 N and about 1 mm for 1 N;
- It has a dynamic resolution of 50 mN.

The spatial resolution can be further enhanced by reducing the size of the system. All these aspects were verified with experiments. The results shown herein demonstrate the feasibility of a high resolution artificial tactile system that enables measuring the touch position as well as the applied force and torque values.

## **2.3 Intrinsic tactile sensing system adapted to robotic finger implementation**

The system proposed in the previous section satisfies many of the characteristics desired for tactile systems in dexterous manipulation of objects. Some points, such as the soft surface, non planar surface, or the size of the system are still not accomplished. In this section, a new system more suitable for anthropomorphic robotic gripper implementation is designed. The system should be smaller, more robust and accurate than the one presented in the previous section.

This section is divided in six subsections: The first part describes the design and construction of the tactile system by incorporating four 3-axis force sensors. The second part shows the mathematical model used to estimate the contact parameters. The third subsection reports the calibration of the tactile system. In the fourth and fifth subsection the tactile system is tested and validated. Finally the results are analyzed and the conclusions are made.

### **2.3.1 Design and construction of the system**

#### **2.3.1.1 Design of the tactile system**

The design of this system uses four 3-axis force sensors fixed on a printed circuit board (PCB) that will be attached to the robotic finger. The 3-axis force sensors are protected with a coating

using the guidelines of chapter 1. Then, coatings are attached to a rigid frame. On the frame, different types of surfaces can be fixed. In this work a rigid frame with a soft layer is used as shown in the figure 2.21.

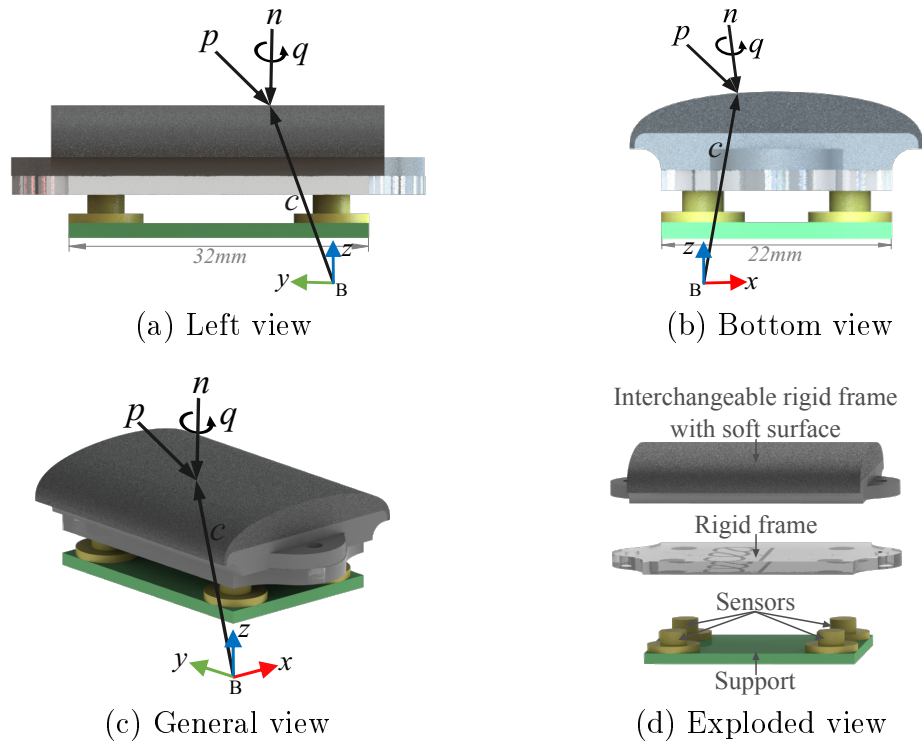


Figure 2.21: Design of the system

This design has one extra sensor compared to the system presented in the section 2.2. By adding one more sensor, the forces and torques applied to the system are distributed on more supports, which increases the maximal force that can be applied to the system. This redundant measurement for multi-variable sensors has already been investigated in publications such as [BC94].

### 2.3.1.2 Construction of the 3-axis force sensor array and its protection

The 3-axis force sensors used to build this system are based on MEMS (Micro Electro Mechanical System) technology. Four sensors are attached and connected to a printed circuit board (PCB), as shown in figure 2.22a.

To protect the sensors and to increase the maximum supported force and create an interface that could be glued to the rigid frame, each sensor is coated with a protection layer as shown in figure 2.22b. This coating is made by molding polyurethane directly on the sensors. The geometry of the coating is composed of two concentric cylinders. The largest one in the base assure the adherence of the coating and the support. The second is glued to the rigid frame. It is assumed that the plane on top of the cylinder is parallel to the rigid frame, consecutively it is assumed that the distribution of forces on the cylinder is constant, therefore a proportional force of the total force applied on the sensor is applied in the center of the coating as required by the proposition of the chapter 1.

The transducer function for each sensor is:

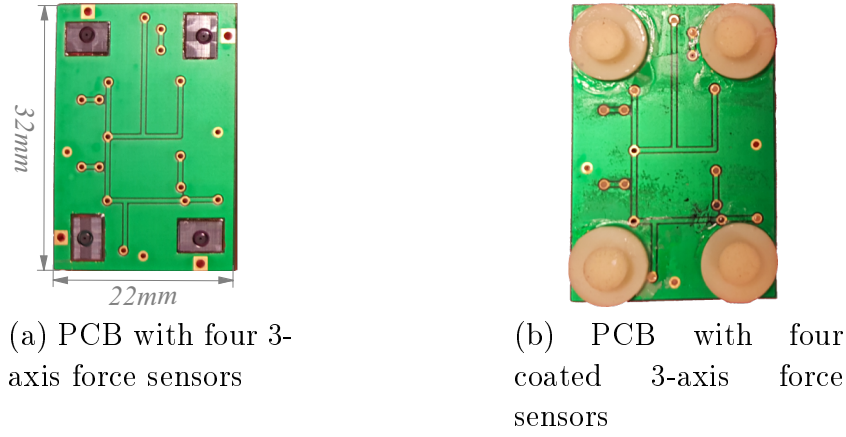


Figure 2.22: Mounted sensors in the PCB

$$\vec{f}_i = \mathbf{S}_i \cdot (\vec{u}_i - \vec{b}_i) \quad (2.25)$$

where the force vector measured by the sensor  $i$  is  $\vec{f}_i$ , the vector  $\vec{b}_i$  (in V) is a voltage bias. The bias is specific to each sensor. The voltages  $\vec{u}_i$  are the output voltages of the sensor. The matrix  $\mathbf{S}_i$  (in  $\text{N V}^{-1}$ ) is the sensitivity matrix. This matrix is expressed in Newtons by Volts, transforms the voltage into force while taking into consideration the coupling effect caused mainly by the coating of the sensor. This matrix changes depending on the point of application of the forces on the coating. For this reason, it cannot be estimated before the rigid frame is glued.

### 2.3.1.3 Rigid frame and interchangeable frame

To ensure that all sensors are linked by the same rigid frame, and the forces are well distributed on all the sensors, the first rigid frame is glued to the coated sensors, as shown in figure 2.23a. Then, the interchangeable rigid frame with soft surface is fixed by screws to the first rigid frame as shown in figure 2.23b.

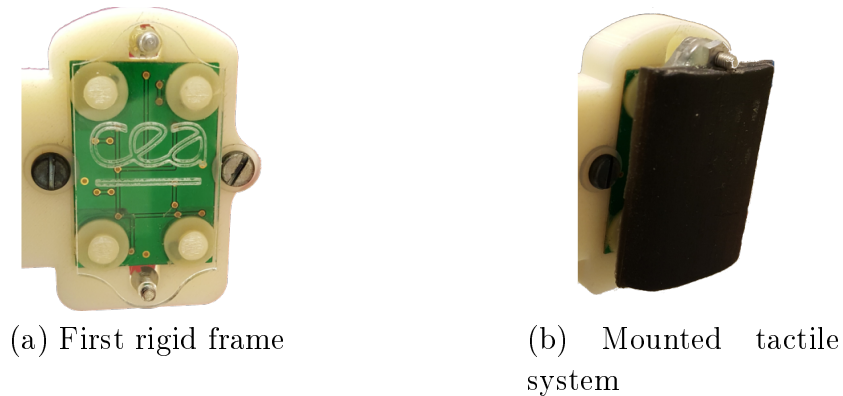


Figure 2.23: Mounted rigid frame and tactile system

The first rigid frame is made with acrylic. The interchangeable surface is made by multi-material 3D printing, with the following characteristics: the rigid material that serves as frame has a tensile strength between 50 and 65 MPa and a shore hardness scale D between 83 and 86.

The soft surface (the contact surface), has a tensile strength between 1 and 2 MPa and a shore hardness scale A of 50. The equation of the contact surface  $S$  is expressed as an ellipse in the plane  $(x, z)$  (i.e. the  $x$  and  $z$  coordinates are dependent on an elliptic form and independent of the  $y$  coordinate). The surface is defined with respect to the reference frame  $B$ . To simplify the equations, the reference  $B$  is placed in the center of the ellipse in  $(x, z)$  plane and in the middle of the segment separating the two sensor couples along the  $y$  axis. Therefore, the function of the surface is expressed by the following equation:

$$S(\vec{c}) = \frac{c_x^2}{a^2} + \frac{c_z^2}{b^2} - 1 = 0 \quad (2.26)$$

where  $a = 14$  mm and  $b = 5$  mm are the semi-axes of the ellipse. The constraints of positions for  $\vec{c}$  are:

$$-a \leq c_x \leq a \quad (2.27)$$

$$-16 \text{ mm} \leq c_y \leq 16 \text{ mm} \quad (2.28)$$

$$0 \leq c_z \leq b \quad (2.29)$$

### 2.3.2 Touch parameters estimation

The developed tactile system is able to estimate the following parameters: the contact position  $\vec{c}$ , the applied force  $\vec{p}$ , and applied torque  $\vec{q}$ . In this work, the test bench presented in section 2.24 has no means of generating or measuring torque. Since no torque reference nor torque generating system was available. The accuracy of torque estimation by the system was not guaranteed. The applied torque value  $\vec{q}$  is considered to be negligible in the following setup. Under these considerations, the model of contact used in this work is called point contact with friction, as explained in [Mur+94]. In fact, the presence of a reference torque measurement sensor would enhance the quality of system calibration and enables quantifying torque estimation accuracy.

Substituting equation (2.5) in equation (2.2) gives:

$$\vec{p} = \sum_{i=1}^4 \vec{f}_i \quad (2.30)$$

Consequently, replacing equation 2.30 and 2.6 in equation 2.3 and assuming that  $\vec{q} = 0$ , equation 2.3 becomes:

$$\sum_{i=1}^4 \vec{l}_i \times \vec{f}_i = \vec{c} \times \sum_{i=1}^4 \vec{f}_i \quad (2.31)$$

Along with equation 2.1, a system with four equations (2.31 and 2.1) and three unknowns (the position vector coordinates  $\vec{c}$ ) is obtained. The system has two different solutions. These equations calculate the intersection of the axis formed by the force vector or wrench axis with the surface. This axis intersects with the surface two times. The first intersection point corresponds to the force pointing from the object in contact with the system to the surface. The other intersection point corresponds to the force pointing from the surface to the object in contact. As mentioned in section 2.1.5, the forces are assumed to be compressive which means

that the object in contact with the surface can only push on the surface and can not pull the surface. By adding this constraint, the system has one unique solution. A method to solve this kind of problems was implemented in [BSB93]. In our paper, the system is solved as follows:

- The value  $c_z$  is solved from equation (2.1). Given the limits in equation (2.29) the result is:

$$c_z = \frac{b\sqrt{a+c_x}\sqrt{a-c_x}}{a} \quad (2.32)$$

- In equation (2.31), the value of  $c_z$  is replaced by the result in (2.32).
- Taking arbitrary two equations of 2.31, the values of  $c_x$  and  $c_y$  could be solved. Two possible solutions are found. Respecting the condition of compressive forces, a function that calculates the position  $\vec{c}$  is:

$$\vec{c} = h(\vec{f}_i) \quad (2.33)$$

This function depends on the measured forces, the ellipse parameters  $a, b$  and the distances  $\vec{l}_i$ .

After neglecting the torque, the parameters to be estimated are the applied force  $\vec{p}$  and the position of contact centroid  $\vec{c}$ . The input of the system are the voltages  $\vec{u}_i$  measured by each sensor. By replacing equation (2.25) in equations (2.30) and (2.33), and joining those two equations, a non-linear model for estimating the touch parameters is constructed:

$$\begin{bmatrix} \vec{p} \\ \vec{c} \end{bmatrix} = g \left( \vec{u}_1 - \vec{b}_1, \vec{u}_2 - \vec{b}_2, \vec{u}_3 - \vec{b}_3, \vec{u}_4 - \vec{b}_4 \right) \quad (2.34)$$

This model has, as inputs, the voltages  $\vec{u}_i$  without bias  $\vec{b}_i$  of each sensor and as outputs, the applied force  $\vec{p}$  and position  $\vec{c}$ . The model has as constants parameters: the surface constants  $a$  and  $b$ , the distances  $\vec{l}_i$  and the sensitivity matrices  $\mathbf{S}_i$ . The values of the distances  $\vec{l}_i$  are roughly known, and could be any point that is within the intersection between the coating and the rigid plate. The sensitivity matrix is unknown. The method to calibrate these parameter are shown in the next section. In this model, the losses in forces made by the elastic material are supposed negligible.

### 2.3.3 Calibration method

To calibrate the touch system, the values of bias  $\vec{b}_i$ , sensitivity matrix  $\mathbf{S}_i$  and the distances  $\vec{l}_i$  must be estimated. Because the bias could change with the temperature (sensor piezo-resistive nature [Bou+13], or expansion/contraction of the rigid frame), it is calculated every time the system starts. In fact, an average value is computed at the beginning of the test while no forces are exerted on the system. To estimate the rest of the values, a non linear mean squares minimization is used as follows:

$$\{l_i, \mathbf{S}_i\} = \underset{l_i, \mathbf{S}_i}{\operatorname{argmin}} \sum_{j=1}^n \left( \operatorname{ref}_j - g \left( \begin{bmatrix} \vec{u}_1 - \vec{b}_1 \\ \vec{u}_2 - \vec{b}_2 \\ \vec{u}_3 - \vec{b}_3 \\ \vec{u}_4 - \vec{b}_4 \end{bmatrix}_j \right) \right)^2 \quad (2.35)$$

where  $i = 1, 2, 3, 4$  is the sensor index,  $ref$  is the reference measurement at sampling time  $j$ ,  $n$  is the number of samples.

### 2.3.4 Experimental Set up

The experimental test bench used to calibrate and test the system is shown in appendix A.1.2, this system is conditioned as shown in figure 2.24.

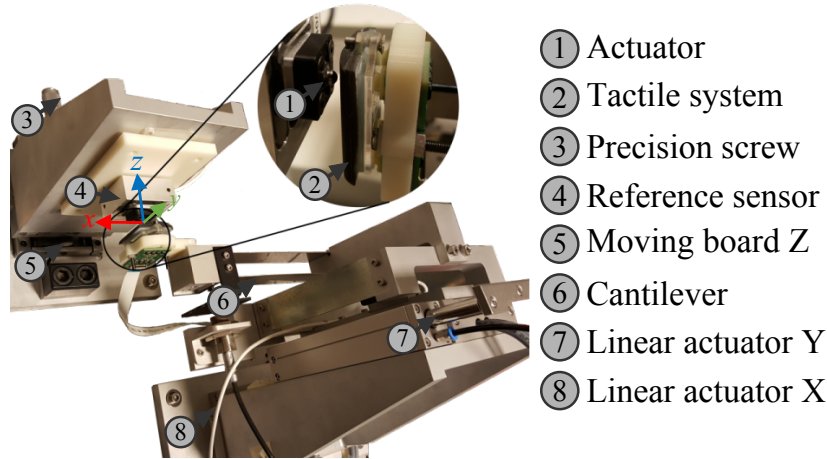


Figure 2.24: Intrinsic measures

This setup prevents from applying high strength forces on the system. The developed tactile system is placed at the end of the cantilever, and the system is aligned with x and y axis of the system. A reference 3-axis force sensor (the K3D40) is assembled on a moving board, in front and parallel to the tactile system. This board can move in the z axis by a precision screw that is actioned manually or by a pneumatic actuator. An actuator is fixed at the end of the reference sensor. The actuator is a metal sphere with a diameter of 4 mm. This shape helps to have the center of applied forces near the center of the sphere.

This setup was tuned in order to respect the following constraints: deformation of the cantilever or the coating of tactile system in the x and y axis are negligible. The reference sensor surface and the tactile system rigid surface are considered parallel during all the experiment.

The calibration of the system is made by applying a wide range of forces on a extensive set of positions in order to explore most of the sensing dynamics. To meet this requirement, the following calibration process is proposed:

- The system is placed at the starting position of a predefined trajectory as shown in figure 2.25, and data acquisition is started.
- Precision screw is rotated until the actuator exceeds a force of 1 N in the z axis. The reference of force is measured by the K3D40 sensor.
- The system is moved to follow multiple pre-defined trajectories as shown in the figure 2.25. The speed of the linear actuators during the displacement is  $2.5 \text{ mm s}^{-1}$ .
- At the end of each trajectory, the acquisition stops.

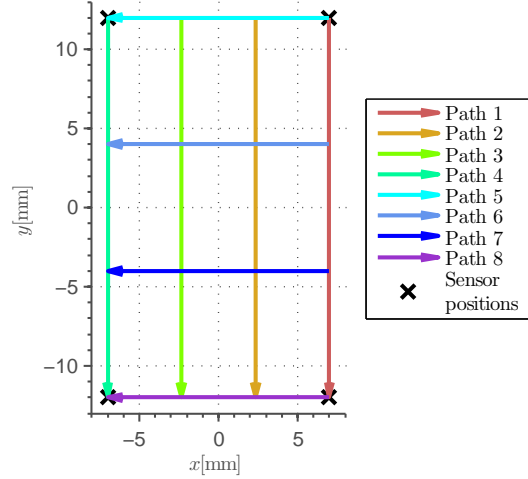


Figure 2.25: Trajectories for calibration

All incoming signals are amplified using a custom made analogous amplifier and then digitized at a frequency of 1 kHz. The signals are also filtered with a second order low pass filter with a cutoff frequency of 100 Hz.

### 2.3.5 Experimental results

All trajectories presented in figure 2.25 were applied two times: once for calibration and once for verification. Both the data measured by the system and the data measured by the reference system (position/force measurements) are synchronized. The calibration method explained in section 2.3.3 is applied. After the calibration, equation 2.34 is used to determinate the force  $\vec{p}$  and the contact position  $\vec{c}$ .

The minimal force that needs to be applied to accurately find the position depends on the resolution of the sensors as shown in [ZSL96]. As shown in the accuracy analysis in section 2.2.4, the estimation of the position is made when the norm of the applied force is greater that  $\|\vec{p}\| \geq 0.6 \text{ N}$ .

The results of this experiment are shown in figure 2.26. The error statistics compared to the reference for all the verification measurements are shown in table 2.5.

Measure	Mean error	Max error	Standard deviation	RMSE
$p_x$	1.20 mN	158.07 mN	29.21 mN	29.23 mN
$p_y$	-1.14 mN	108.65 mN	22.39 mN	22.42 mN
$p_z$	3.48 mN	206.88 mN	18.73 mN	19.05 mN
$\ \vec{p}\ $	37.79 mN	240.57 mN	17.07 mN	41.47 mN
$c_x$	-625.20 nm	611.13 $\mu\text{m}$	103.83 $\mu\text{m}$	103.83 $\mu\text{m}$
$c_y$	2.32 $\mu\text{m}$	520.08 $\mu\text{m}$	94.65 $\mu\text{m}$	94.68 $\mu\text{m}$
$c_z$	136.18 nm	79.05 $\mu\text{m}$	13.96 $\mu\text{m}$	13.96 $\mu\text{m}$
$\ \vec{c}\ $	118.64 $\mu\text{m}$	621.04 $\mu\text{m}$	76.58 $\mu\text{m}$	141.21 $\mu\text{m}$

Table 2.5: Error statistics for experiment 1



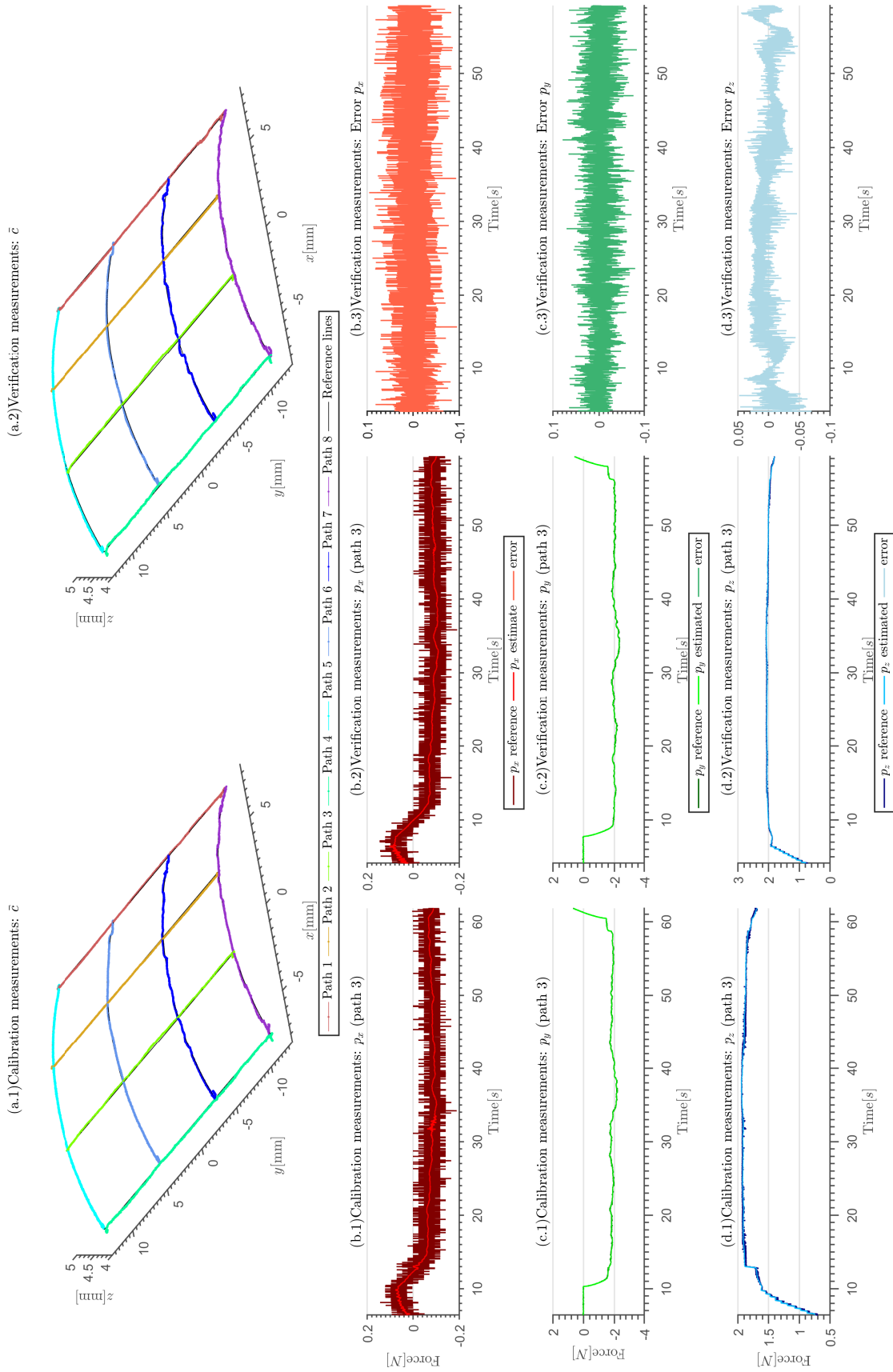


Figure 2.26: Experimental results

The force estimation, as shown in figures 2.26.b, 2.26.c, 2.26.d and in the table 2.5 shows a good matching with the reference. The noise of the estimated forces is significantly lower than the reference system. The measured standard deviation of the noise measured by the reference system in the absence of applied forces is 17 mN. The proposed tactile system has a measurement noise of only 2 mN. Consequently, the error is mostly dominated by the noise of the reference system.

The position estimation is as shown in figures 2.26.a, it follows all the eight reference paths without offset, as shown in table 2.5. The repeatability of the system is tested when two paths intersect, i.e. for different conditions in tangential forces, and different lapses in time, the sensor succeeds in having the same measurement in position.

### 2.3.6 Conclusion

This subsection deals with the design, construction, mathematical modeling and calibration of an intrinsic tactile sensing system designed to be implemented in a robotic anthropomorphic gripper, and to fulfill most of the requirements for dexterous manipulation of objects ([Dah+10]; [YBA11]):

- measured properties : The three components of the force and the three components of the torque applied to the surface. As well as the position of the contact centroid;
- sensing surface: Curved surface with soft cover;
- spacial resolution: About 150  $\mu\text{m}$  (for 1 N force);
- sensitivity range: 10 mN- 10 N;
- dynamic resolution: 20 mN (Standard deviation);
- response profile: Good stability and low hysteresis.

The system consists in an array of four 3-axis force sensors linked to a rigid frame covered with a soft surface. The mathematical model is a special case of the model proposed in [BSB93]. The calibration of the system is obtained by reducing the quadratic error between reference measurements and the estimated state of the mathematical model in order to find the unknown parameters of the system.

The tactile system can measure the three components of force, as well as contact position under the conditions of soft tactile sensing [BSB93]. This system is also able to measure the three components of the torque applied perpendicular to the surface but the necessary equipment to validate and qualify the accuracy of torque estimation was not available as explained in section 2.3.2.

This system is a considerable improvement compared to the system developed in the previous subsection 2.2. It has a non-planar soft surface. The base of the system is 22 mm wide by 32 mm long which is small enough to be implemented in the fingertips of a robotic manipulator, such as the manipulator presented in [GMP15]. The system can estimate the applied forces and the position of contact with great accuracy. Here, the maximum measured error in force is 240.57 mN and the root mean square error (RMSE) is 41.47 mN. The maximum measured error in position is 621.04  $\mu\text{m}$  and the RMSE is 141.21  $\mu\text{m}$ .

The force estimation error compared to the reference system is nearly the same as the one obtained using the previous system. In fact, this error is mainly dominated by the high noise level in the signals provided by the available reference system used in these experiments. A more accurate system with a significantly lower noise level will be used in further work in order to better qualify the designed system accuracy. On the other hand, the position estimation accuracy has been well enhanced using this system (the standard deviation of the position error is  $76\ \mu\text{m}$ ) compared to the previous one (the standard deviation of the position error is  $372\ \mu\text{m}$ ).

This system matches almost every requirement proposed in the section 2.1.3.3 for dexterous manipulation of objects with the exception of detecting the shape of the contact surface.

# Early slip detection for an intrinsic tactile system

## Contents

<b>3.1</b>	<b>State of the art: Limit surface . . . . .</b>	<b>66</b>
3.1.1	Assumptions . . . . .	67
3.1.2	Theory of limit surface . . . . .	67
3.1.3	Conclusion . . . . .	68
<b>3.2</b>	<b>State of the art: Contact models for soft fingers . . . . .</b>	<b>69</b>
3.2.1	Assumptions . . . . .	69
3.2.2	Power Law: Non linear elastic model . . . . .	69
3.2.3	Viscoelastic model . . . . .	71
3.2.4	Viscoelastic model with imposed displacement . . . . .	72
3.2.5	Viscoelastic model with imposed normal force . . . . .	74
3.2.6	Conclusion . . . . .	78
<b>3.3</b>	<b>Soft fingertips characterization . . . . .</b>	<b>78</b>
3.3.1	Intrinsic tactile system with soft fingertips design and construction . . . . .	79
3.3.2	Characterization test bench . . . . .	80
3.3.3	Characterization of the elastic response . . . . .	81
3.3.4	Characterization reduced relaxation function . . . . .	84
3.3.5	Relation between the radius $a$ and the deformation $\delta$ test . . . . .	88
3.3.6	Estimation of the parameter $k$ . . . . .	89
3.3.7	Conclusion . . . . .	92
<b>3.4</b>	<b>Slip detection using limit surface . . . . .</b>	<b>92</b>
3.4.1	Slippage test bench . . . . .	93
3.4.2	Construction of the limit surface . . . . .	94
3.4.3	Experiment . . . . .	94
3.4.4	Results and analysis . . . . .	95
3.4.5	Conclusion . . . . .	99

## Context and motivations

In previous chapter 2, an intrinsic tactile sensing system was developed. The system is intended to be integrated in a robotic gripper to enable it the performance of dexterous manipulation of objects. One of the objectives of the system is to detect and prevent object slippage. Thus, this chapter is intended to implement an algorithm for early detection of slippage using intrinsic tactile systems with soft surfaces.

The intrinsic tactile system used in the chapter is the commercial sensor 'Ati nano17'. In fact, the system presented in Chapter 2 was damaged during an experiment. One of the wire bonding connections is lost(see section 1.3.1). The construction of a new system would require more time than just using the commercial system. The work presented in this chapter can perfectly be applied to the system proposed in chapter 2.

## Chapter objective

This chapter is intended to review the state of the art necessary to implement an algorithm for early detection of slippage using an intrinsic tactile sensing system. On the basis of previous research, the algorithm would then be implemented on the tactile system in order to prevent slippage.

## Outline of the chapter

This chapter is divided into five sections: The first part describes the friction limit theory named limit surface. The second section reviews the viscoelastic contact model that is necessary to implement the limit surface theory on an intrinsic tactile sensing system. The third part shows the construction and characterization of soft fingers based on the viscoelastic model of contact. The fourth section reports the implementation of limit surface theory for early slippage detection on an intrinsic tactile system. Finally the results are analyzed and conclusions are made.

### 3.1 State of the art: Limit surface

In this section, the friction limit described by limit surface theory is presented. This concept draws the limit of friction in force and torque for two objects in contact.

The concept of limit surface was initially developed by Jameson [Jam86] in 1985, and it was later on enhanced by Goyal [GRP89] and [GRP91]. They also provided useful tools for characterizing the motion-force relationship.

The present description will draw fully on the concept of limit surface as presented in [HC96]. The construction of a limit surface involves an analysis of pressure distribution at each point of contact and the contribution of each point to the total frictional force  $\vec{f}_f$  and torque  $\vec{\tau}_f$ .

The limit surface can be constructed by solving the problem of computing the forces and torques for each possible translational and rotational motion. The limit surface supplies a mapping between applied forces and the resulting motions.

### 3.1.1 Assumptions

Three basic assumptions are made:

- A body undergoes fully developed sliding on a locally planar surface
- The distribution of normal force (or pressure) across the contact surface is known
- Friction force depends only on the local normal force applied and on slip direction, but not on the magnitude of slip velocity or slip history.

Also, the sliding criteria are based on the assumption that the relative velocity field through the contact area matches to a unique center of rotation (COR). For rigid bodies, the relative velocity field is always true. However, these criteria also apply to deformable bodies such as soft fingertips provided that the deformations of the contact area are slow compared to its sliding speed. Other restrictions apply. For further information, see [GRP89] and [GRP91].

### 3.1.2 Theory of limit surface

The direction of slippage for each contact point must be first found in order to obtain the direction of the friction force. From the point of view of kinematics, the instantaneous motion of a rigid body in a plane can always be described as pure rotation with respect to some point, referred to as the center of rotation (COR). The connection between frictional force, frictional torque and the sliding motion can be calculated by assuming an identified COR position, then adding the frictional force contribution at each point across the contact surface. Figure 3.1 shows the situation in the sliding plane.

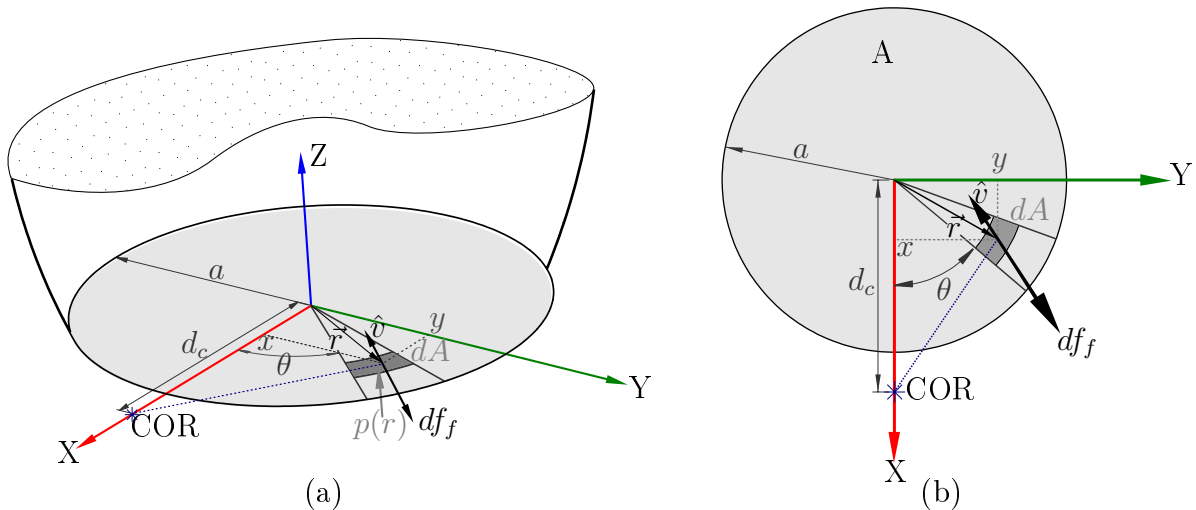


Figure 3.1: Representation of the COR and the local infinitesimal area  $dA$  where each force is calculated

A coordinate system is fixed to the contact plane. The origin of the coordinate system is located at the friction-weighted center of pressure  $(x_c, y_c)$ :

$$x_c = \frac{\int_A x \mu_s(x, y) p(x, y) dA}{\int_A \mu_s(x, y) p(x, y) dA} \quad (3.1)$$

$$y_c = \frac{\int_A y \mu_s(x, y) p(x, y) dA}{\int_A \mu_s(x, y) p(x, y) dA} \quad (3.2)$$

The  $x$  axis is directed to the COR. The vector  $\vec{r} = [x, y]'$  is a vector that points to the differential element of area  $dA$ . The vector from the COR to the differential of the area is expressed as  $r_{cor} = [d_c, 0]$ , so  $\vec{d} = \vec{r} - r_{cor} = [x - d_c, y]'$ . It is assumed that friction is independent of sliding speed, so velocity can be represented by the unit vector  $\hat{v}(\vec{r}) = \vec{v}(\vec{r})/|\vec{v}(\vec{r})|$ . Since each contact point is instantaneously rotating with respect to the COR, the velocity vector is perpendicular to  $d$ , and can be expressed as

$$\hat{v}(\vec{r}) = \begin{bmatrix} \frac{-dy}{|d|} \\ \frac{dx}{|d|} \end{bmatrix} \quad (3.3)$$

The normal force on any point of the contact area is expressed as  $df_N = p dA$ , where  $p(\vec{r})$  is a function that expresses pressure distribution, and  $dA$  is the infinitesimal area at point  $\vec{r}$ . The magnitude of the frictional force at this point is  $df_f = -\mu_s p dA$ , where  $\mu_s(\vec{r})$  is the local coefficient of friction. It is known that the direction of the frictional force is opposed to its velocity at a certain point. Then, the local frictional force vector can be expressed as  $df_f = -\mu_s p \hat{v} dA$ . The total frictional force can be found by integrating all the contact points on the surface of contact:

$$f_f = - \int_A \mu_s \hat{v} p(\vec{r}) dA \quad (3.4)$$

The impact on the frictional torque (resolved to the origin) is given by the cross-product of vector  $\vec{r}$  and the local frictional force. Since velocity is on the same plane as the contact points, torque is normal to the plane, and can be treated as a scalar. The total applied torque  $\tau_N$  is the integral of:

$$\tau_N = - \int_A \mu_s [\vec{r} \times \hat{v}] p(\vec{r}) dA \quad (3.5)$$

With equations 3.4 and 3.5 it is possible to find the total frictional force and torque for any motion, as well as for any given pressure distribution  $p(\vec{r})$  and coefficient of friction  $\mu_s(\vec{r})$ . By performing this calculation for a number of COR locations, the limit of friction for the force and torque can be generated. This result expresses the maximum force and torque that could be applied before sliding as shown in figure 3.2.

### 3.1.3 Conclusion

To implement limit surface theory as the limit of friction, it should be noted that the model depends on pressure distribution  $p(\vec{r})$  and the friction coefficient  $\mu_s(\vec{r})$ .

The friction coefficient  $\mu_s(\vec{r})$  depends on the materials in contact. On the other hand, pressure distribution depends on the type of contact. Therefore, the following section presents pressure distribution for soft fingers, and how said pressure distribution can be calculated from an intrinsic tactile system.

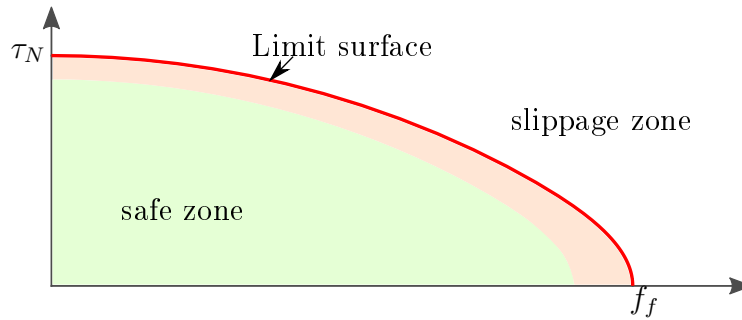


Figure 3.2: Representation limit surface

## 3.2 State of the art: Contact models for soft fingers

As shown in the previous section, it is necessary to know the pressure distribution to estimate the limit of friction. This section presents the different models used to characterize the behaviour of soft fingers in contact, including pressure distribution.

### 3.2.1 Assumptions

The following assumptions are made for this type of contact:

- The soft fingers have an hemispherical geometry
- The deformations generated in the soft finger are produced by a rigid object
- The deformation is vertical to the soft finger.

In this work the induced deformations are assumed vertical to the soft finger. In [IH03] the contact properties are analyzed for different directions of the deformation.

### 3.2.2 Power Law: Non linear elastic model

In 1999, [XK99] introduced a function for general pressure-distribution whose purpose was to capture material properties and contact geometry with various pressure profiles. Consequently, in the case of a soft finger with hemispherical geometry, pressure distribution in a circular contact area with radius  $a$  is written as follows:

$$p(r) = C_k \frac{N}{\pi a^2} \left( 1 - \left( \frac{r}{a} \right)^k \right)^{\frac{1}{k}} \quad (3.6)$$

where  $N$  is the normal force,  $a$  is the radius of contact,  $k$  determines the shape of the pressure profile, and  $C_k$  is a coefficient that adjusts the profile of pressure distribution over the contact area to satisfy the equilibrium condition. The function depends on the  $r$  variable. Since the contact area is assumed to be flat, and pressure distribution is symmetrical, the variable  $r$  can range from 0 to  $a$ . When  $k$  becomes larger, pressure distribution approaches uniform distribution, as shown in Figure 3.3.



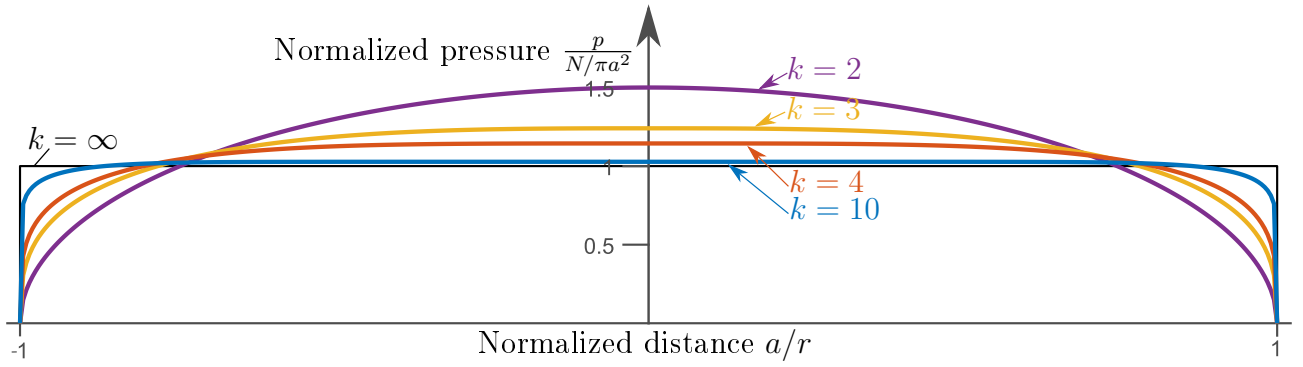


Figure 3.3: Power Law model of pressure distribution

The equilibrium condition to find the coefficient  $C_k$  is the following:

$$\int_A p(r) dA = \int_{\theta=0}^{2\pi} \int_{r=0}^a p(r) r dr d\theta = N \quad (3.7)$$

The coefficient  $C_k$  in the pressure-distribution equation 3.6 can be determined using equation 3.7. The result obtained by [XK99] is:

$$C_k = \frac{3}{2} \frac{k \Gamma\left(\frac{3}{k}\right)}{\Gamma\left(\frac{1}{k}\right) \Gamma\left(\frac{2}{k}\right)} \quad (3.8)$$

For further details, see [XK99]. The gamma function  $\Gamma$  is defined for real  $x > 0$  by the integral:

$$\Gamma(x) = \int_0^{\infty} e^{-t} t^{x-1} dt \quad (3.9)$$

### 3.2.2.1 Limit surface based on the Power in law model

Figure 3.4 illustrate what is the influence of the normal force  $N$ , the radius of contact  $a$  and the shape parameter  $k$  in the limit surface.

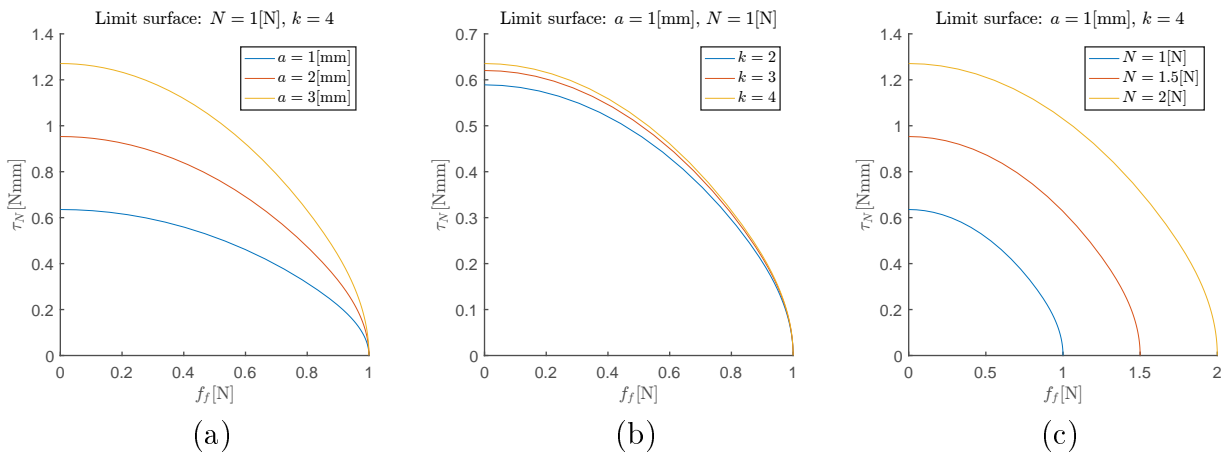


Figure 3.4: Limit surface based on the Power in law model

The coefficient of friction  $\mu$  affects the limit surface in the same way that the normal force i.e., the coefficient of friction and the normal force multiply the limit surface as a scale factor.

An intrinsic tactile system is able to measure the normal force  $N$ . However, the radius of contact  $a$  and the parameter  $k$  should be estimated. The next subsection explains one method used to estimate the radius of contact  $a$  and the parameter  $k$  in terms of the normal force  $N$  and/or time  $t$ .

### 3.2.3 Viscoelastic model

As shown in section 3.1, the friction limits of force and torque of two surfaces in contact depend on the distribution of pressure  $p(r)$  and, as said in the previous subsection 3.2.2, the distribution of pressure is a function of the normal force  $N$ , the radius of contact  $a$ , and the shape parameter  $k$ .

The goal of this section is to present the viscoelastic model of contact. In this model, the deformation  $\delta$  and the normal force  $N$  are related. Furthermore, as proposed by [Bar+04] and [TK07], the radius of contact  $a$  - as shown in Figure 3.5 - is expressed in terms of the deformation  $\delta$  as:

$$a^2 = R^2 - (R - \delta)^2 \quad (3.10)$$

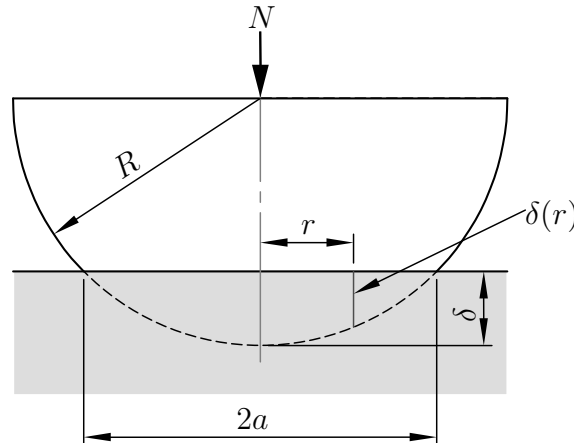


Figure 3.5: Viscoelastic model of contact

For rubber materials and the human finger, the deformation  $\delta$  and normal force  $N$  are time-dependent functions. For the viscoelastic model of contact, two different time behaviours should be studied: relaxation and the creep phenomena. A general approach proposed by Findley [FD76] considers that force and deformation can be related. The "relaxation function" is as follows:

$$N(t) = \mathcal{G}(\delta, t) \quad (3.11)$$

In the general case of non-linear viscoelasticity, the relaxation function specifies the response of force  $N$ , as time elapses, to a step deformation with respect to the undeformed configuration.

The "creep compliance" function is the following:

$$\delta(t) = \mathcal{H}(N, t) \quad (3.12)$$

This function gives the deformation  $\delta$  response to the force with respect to the unreformed configuration. Those two behaviours of viscoelastic materials are related as shown in [FD76]. If it is assumed that for small deformations the applied normal force is proportional to said deformation  $N \propto \delta$ , the functions  $\mathcal{G}$  and  $\mathcal{H}$  become only a function of time, as:

$$N(t) = \mathcal{G}(t) \delta \quad (3.13)$$

$$\delta(t) = \mathcal{H}(t) N \quad (3.14)$$

Authors like [PH99], [Bia+05] and [TK07] adopt the hypothesis of [Fun93] for the general case of nonlinear viscoelasticity. This hypothesis isolates the elastic response from the temporal response. This approach allows for the use of different models of elastic response for soft fingers, notwithstanding the temporal response for viscoelastic contacts. Viscoelastic contact modeling can be understood as the linking of a function of deformation  $\delta$  or the magnitude of the normal force  $N$  with the temporal response as a function of time  $t$ .

### 3.2.4 Viscoelastic model with imposed displacement

In 1993, Fung [Fun93] proposed a model for the "relaxation function". This model has two main elements: an immediate elastic response  $N^{(e)}(\delta)$ , which is the amplitude of the force instantaneously generated by a deformation  $\delta$ , and a reduced relaxation function  $g(t)$  which describes the time-dependent behaviour of the material.

$$\mathcal{G}(\delta, t) = N^{(e)}(\delta) g(t) \quad \text{with} \quad g(0) = 1; \quad (3.15)$$

The differential change of the force response  $dN(t)$  to an infinitesimal change in deformation  $d\delta$ , superposed in a state of deformation  $\delta$  at an instant of time,  $\tau$ , for  $t > \tau$ , is described as:

$$dN(t) = g(t - \tau) \frac{\partial N^{(e)}[\delta(\tau)]}{\partial \delta} d\delta(\tau) \quad (3.16)$$

As discussed in [FD76] and [PR68], the superposition principle is applied to this model. Then, the total force at the instant  $t$  is the sum of contributions of all the past changes.

$$N(t) = \int_{-\infty}^t g(t - \tau) \frac{\partial N^{(e)}[\delta(\tau)]}{\partial \delta} \frac{\partial \delta(\tau)}{\partial \tau} d\tau \quad (3.17)$$

It is assumed that the motion starts at  $t = 0$  and the finger applied forces and deformations for any time  $t < 0$  are zero, i.e.  $N^{(e)}(t < 0) = 0$  and  $\delta(t < 0) = 0$ .

$$N(t) = \int_0^t g(t - \tau) K^{(e)}[\delta(\tau)] \dot{\delta}(\tau) d\tau \quad (3.18)$$

where  $K^{(e)}(\delta) = \frac{\partial N^{(e)}}{\partial \delta}$  is the elastic stiffness and  $\dot{\delta}(\tau)$  is the rate of deformation.

### 3.2.4.1 Reduced relaxation function $g(t)$ :

Following the hypothesis of Fung as shown in equation 3.15, the reduced relaxation function  $g(t)$  decreases over time, and it is normalized to 1 at  $t = 0$ . It can be expressed as ([PH99] [FD76]):

$$g(t) = \sum_{i=0}^r c_i e^{-v_i t} \quad \text{with} \quad \sum_{i=0}^r c_i = 1 \quad \text{and} \quad v_0 = 0 \quad (3.19)$$

where  $c_i$  depends on the material. This function is composed of a linear combination of exponential functions, and the exponents  $v_i$  are the rates of the relaxation phenomena.

### 3.2.4.2 Elastic response $N^{(e)}(\delta)$ :

As said before, this function is the amplitude of the instantaneous force generated by a deformation of the viscous material. The elastic response is a non-linear function that has been modeled differently. This function can be found by integrating the contact stiffness. The non-linear contact stiffness of a soft finger is defined as the ratio of change in vertical depression at the contact surface. The two main models of elastic stiffness  $K^{(e)} = \frac{dN}{d\delta}$  are:

$$K^{(e)}(\delta) = m e^{b\delta} \quad (3.20)$$

$$K^{(e)}(\delta) = p \delta^q \quad (3.21)$$

where  $b$ ,  $m$ ,  $p$  and  $q$  are parameters that depend on both the geometry and the material. Those models were used widely. Pawluk [PH99] and Barbagli [Bar+04] use the equation 3.20 to simulate the contact of the human finger. In [HK99] they use both models 3.20 and 3.21 to analyse the stiffness of the human fingertip. Kao [KY04] continued with his work [XK99] and derived an expression that can be related to the equation 3.21. Other authors as [MO99] and [KK97] model this function as a non-linear spring parallel to a non-linear damper as proposed by [HC75], where the stiffness of the spring is expressed by equation 3.21.

As said before, the function  $N^{(e)}(\delta)$  can be found by integrating the contact stiffness (equations 3.20 and 3.21):

$$N^{(e)}(\delta) = \frac{m}{b} (e^{b\delta} - 1) \quad (3.22)$$

$$N^{(e)}(\delta) = \frac{p}{q+1} \delta^{q+1} \quad (3.23)$$

### 3.2.4.3 Block-scheme representation

The model shown in this section can be represented in a block diagram as seen in [Bia+05]. The model is represented by the equation 3.18 that depicts the signal  $K^{(e)}(\delta) \dot{\delta}$  filtered by the system:

$$G(s) = \mathcal{L}\{g(t)\} \quad (3.24)$$

where  $\mathcal{L}$  indicates the Laplace transform. The block representation is shown in Figure 3.6a.

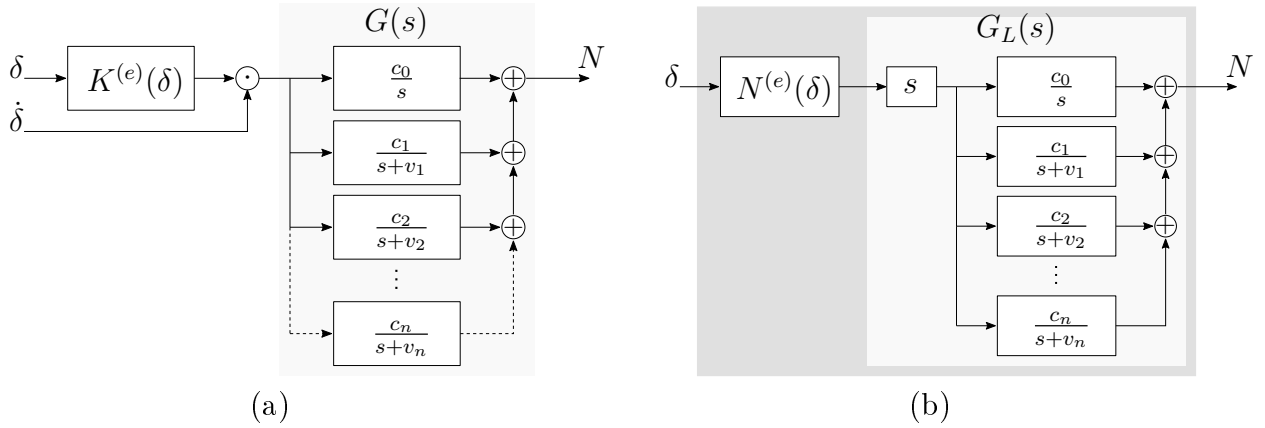


Figure 3.6: Block model of the equation 3.18

The block diagram can be simplified by noticing that the input signal can be rewritten in the following form:

$$K^{(e)}(\delta) \dot{\delta} = \frac{\partial N^{(e)}[\delta]}{\partial \delta} \dot{\delta} = \frac{\partial N^{(e)}[\delta(t)]}{dt} \quad (3.25)$$

The simplified system is shown in Figure 3.6b, where the transfer function  $G_L(s)$  can be expressed as follows:

$$G_L(s) = s \left( \frac{c_0}{s} + \frac{c_1}{s+v_1} + \frac{c_2}{s+v_2} + \dots + \frac{c_r}{s+v_r} \right) = \frac{(\sum_{i=0}^r c_i) s^r + \dots + c_0 (\prod_{i=0}^r v_i)}{s^r + \dots + (\prod_{i=0}^r v_i)} \quad (3.26)$$

### 3.2.4.4 Pressure distribution

As presented in section 3.2.2, the pressure distribution depends on the normal force  $N$ , the radius of contact and the shape parameter  $k$ . As shown in equation 3.18 the force depends on time and deformation  $\delta$ . Consequently, equation 3.6 can be rewritten as:

$$p(r, t) = C_k \frac{N(t)}{\pi a^2} \left( 1 - \left( \frac{r}{a} \right)^k \right)^{\frac{1}{k}} \quad (3.27)$$

Is also known that the radius  $a$  can be expressed in terms of the deformation as shown in 3.10. Therefore, the pressure distribution can be estimated in terms of the radius of contact  $a$  and the shape parameter  $k$ . Therefore, . By substituting the equation 3.18 and 3.19 into 3.27:

$$p(r, t) = \frac{C_k}{\pi a^2} \left[ 1 - \left( \frac{r}{a} \right)^k \right]^{\frac{1}{k}} \int_0^t \left[ c_0 + \sum_{i=1}^r c_i e^{-v_i(t-\tau)} \right] K^{(e)}[\delta(\tau)] \dot{\delta}(\tau) d\tau \quad (3.28)$$

where the elastic stiffness  $K^{(e)}$  can be expressed by the equations 3.20 or 3.21.

### 3.2.5 Viscoelastic model with imposed normal force

In 1993, Fung [Fun93] proposed a model for "creep compliance". This model, as proposed in [FD76], has two main components: an immediate elastic response  $\delta^{(e)}(\delta)$ , which is the am-

plitude of the deformation instantaneously generated by a force  $N$ , and the reduced creep compliance function  $h(t)$  that is time-dependent. As made for the viscoelastic model with imposed deformation, the creep compliance  $\mathcal{H}(N, t)$  for an step input is supposed to be in the form of:

$$\mathcal{H}(N, t) = \delta^{(e)}(N) h(t) \quad \text{with} \quad h(0) = 1; \quad (3.29)$$

Similar to Section 3.2.4, the equation for the deformation in relation to time can be rewritten as:

$$\delta(t) = \int_0^t h(t - \tau) \frac{\partial \delta^{(e)}[N(\tau)]}{\partial N} \frac{\partial N(\tau)}{\partial \tau} d\tau \quad (3.30)$$

Which can be rewritten as:

$$\delta(t) = \int_0^t h(t - \tau) C^{(e)}(N(\tau)) \dot{N}(\tau) d\tau \quad (3.31)$$

where  $\dot{N}(\tau)$  is the speed of change of the normal force, and  $C^{(e)}$  is the elastic compliance that is the inverse of  $K^{(e)}$  (the elastic stiffness represented by equations 3.20 and 3.21).

### 3.2.5.1 Elastic response $\delta^{(e)}(N)$

The immediate elastic response  $\delta^{(e)}(N)$  can be deduced by solving the variable  $\delta$  from the equations 3.22 and 3.23, in which case the equations become as follows:

$$\delta^{(e)}(N) = \frac{1}{b} \ln \left( \frac{b}{m} N + 1 \right) \quad (3.32)$$

$$\delta^{(e)}(N) = \left( \frac{q+1}{p} N \right)^{\frac{1}{q+1}} \quad (3.33)$$

The elastic compliance  $C^{(e)}$  is the inverse of  $K^{(e)}$ :

$$C^{(e)} = \frac{d\delta^{(e)}}{dN} = \frac{1}{K^{(e)}} \quad (3.34)$$

By computing the equations 3.20 and 3.21, it is found that:

$$C^{(e)}(N) = \frac{1}{bN + m} \quad (3.35)$$

$$C^{(e)}(N) = \frac{1}{p} \left( \frac{q+1}{q} N \right)^{-\frac{q}{q+1}} \quad (3.36)$$

### 3.2.5.2 Reduced creep compliance function $h(t)$

As proposed in [FD76], the reduced creep compliance function  $h(t)$  is:

$$h(t) = 1 + \sum_{i=1}^n b_i (1 - e^{-\eta_i t}) \quad (3.37)$$

where the constants  $b_i$  and  $\eta_i$  depend on the material properties, and the exponents  $\eta_i$  are the rates of the creep phenomena.

### 3.2.5.3 Block-scheme representation

The model shown in this section can be portrayed in a block diagram. The model is represented by the equation 3.31 that expresses the signal  $C^{(e)}(\delta) \dot{N}$  filtered by the system:

$$H(s) = \mathcal{L}\{h(t)\} \quad (3.38)$$

where  $\mathcal{L}$  indicates the Laplace transform. The block scheme is shown in Figure 3.7a.

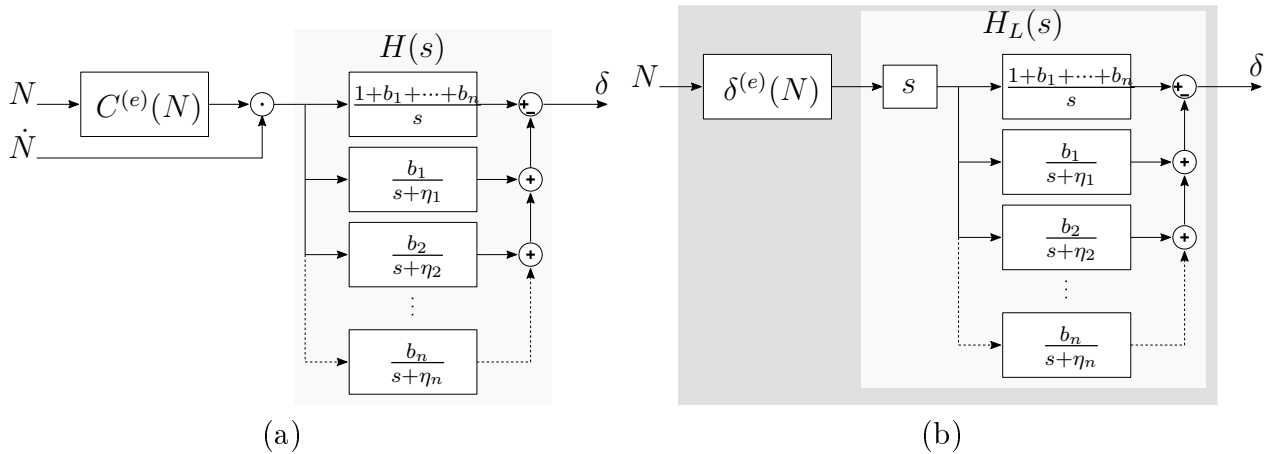


Figure 3.7: Block model of the equation 3.31

The block diagram can be simplified by noticing that:

$$C^{(e)}(N) \dot{N} = \frac{\partial \delta^{(e)}[N]}{\partial N} \dot{N} = \frac{\partial \delta^{(e)}[N(t)]}{dt} \quad (3.39)$$

The simplified system is shown in Figure 3.7b, where the transfer function  $H_L(s)$  can be expressed as follows:

$$H_L(s) = s \left( \frac{1 + b_1 + \dots + b_n}{s} - \frac{b_1}{s + \eta_1} - \dots - \frac{b_n}{s + \eta_n} \right) \quad (3.40)$$

### 3.2.5.4 Pressure distribution

If the normal force  $N$  applied to the hemispherical viscoelastic finger is constant, the deformation  $\delta$  will grow over time as a consequence of the creep phenomena [FD76]. Moreover,

by maintaining the normal force constant, the pressure distribution of viscoelastic contact will progressively become more uniform due to relaxation (as shown in [JJ87] and [Yan66]). Also, it is well known that as deformation increases, the radius of contact increases as well.

Then, pressure distribution also changes because the normal force is constant but the area of contact increases. Consequently, the radius of the area of contact  $a$  and the parameter  $k$  are time-dependent. Therefore, the equation 3.6 can be modified as proposed by Tiezzi and Kao in [TK07], as follows:

$$p(r) = C_{k(t)} \frac{N}{\pi a(t)^2} \left( 1 - \left( \frac{r}{a(t)} \right)^{k(t)} \right)^{\frac{1}{k(t)}} \quad (3.41)$$

where  $C_{k(t)}$  symbolizes the coefficient  $C_k$  as a function of  $k(t)$ . The maximum pressure on the contact surface takes place at  $r = 0$ , resulting in

$$p_{max}(t) = p(0, t) = C_{k(t)} \frac{N}{\pi a(t)^2} \quad (3.42)$$

As the area increases, the maximum pressure decreases. Substituting the pressure distribution equation 3.41 into the equilibrium integral 3.7, the resulting equation is

$$\frac{2C_{k(t)}}{a(t)^2} \int_0^{a(t)} r \left[ 1 - \left( \frac{r}{a(t)} \right)^{k(t)} \right]^{\frac{1}{k(t)}} dr = 1 \quad (3.43)$$

In [TK07], an analysis between the radius of contact  $a$  and the parameter  $k$  is made. They propose that these parameters are correlated, since they depend on the material properties and the geometry of the fingertip. Consequently, they proposed two different coupling equations. The first coupling equation is based on the pressure distribution. The second equation is based on the creep compliance. Those equations were created for a step of normal load as the input to the system. In this work, this relation is not completely useful. The coupling equations are based on the following hypothesis:

**Relation between contact radius  $a$  and deformation  $\delta$ :** The authors of [TK07] assume that the relationship between the radius of contact  $a$  and the deformation  $\delta$  is:

$$a^2 \cong 2R\delta \quad (3.44)$$

This assumption is made by neglecting the term  $-\delta^2$  of the equation 3.10. They argue that this approximation is better because of the conservation of the volume.

**Relation between  $a$  and  $C_k$ :** the radius of contact and the value of  $C_k$  are related, as follows:

$$a \propto \frac{1}{\sqrt{C_k}} \quad (3.45)$$



### 3.2.6 Conclusion

To integrate the limit surface theory as the friction limit for an intrinsic tactile system, it is necessary to know the pressure distribution as shown in equations 3.4 and 3.5. The pressure distribution is modeled by the Power Law model (equation 3.6). This model is useful when all the parameters of contact are known (the normal force  $N$ , the radius of contact  $a$ , and the shape of the pressure distribution represented by  $k$ ).

However, most tactile systems are not able to measure all the required parameters. Therefore, for intrinsic tactile systems, the viscoelastic model of contact as proposed by [TK07] can be used to estimate the deformation  $\delta$  from the normal force  $N$ . Then by applying the assumption of the equation 3.44 that the radius of contact  $a$  can be estimated from the estimated deformation  $\delta$  for hemispherical surfaces. As shown in figure 3.8.

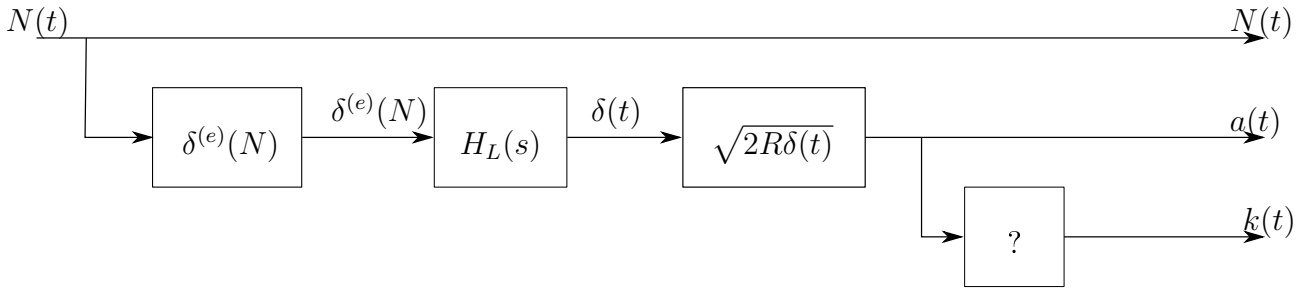


Figure 3.8: Block-scheme initial representation normal force  $N$  to radius of contact  $a$  and the parameter  $k$

Additionally, the parameter  $k$  could be estimated from the radius of contact  $a$  through the relation expressed by equation 3.45. Nevertheless, the direct relation proposed by [TK07] is proposed for a step normal force. Therefore a new relation should be proposed.

Therefore, after reviewing the state of the art, for an intrinsic tactile system, the parameters of the viscoelastic model of contact should be determined to be able to estimate the deformation  $\delta$  from the normal force  $N$ . Then, the assumption 3.44 should be tested. In addition, a relation to estimate the parameter  $k$  from the prior knowledge should be proposed. Thus the limit surface theory could be applied. Consequently, the following section refers to the estimation of the parameters of a viscoelastic finger, the test of the assumption about the radius of contact and the proposition of a function to estimate the parameter  $k$ .

## 3.3 Soft fingertips characterization

As concluded in the previous section, to be able to implement the limit surface theory as limit of friction in intrinsic systems, it is necessary to know pressure distribution in terms of the measured forces and torques of the tactile system. For this reason, the viscoelastic model with imposed normal force could be applied as presented in subsection 3.2.5.4. This function depends on the characteristics of the material. For this reason, an intrinsic tactile system with soft surface is presented, and the necessary parameters to estimate pressure distribution are characterized for two different soft surfaces.

In this section, the intrinsic tactile system used is the commercial sensor Ati Nano17.

The viscoelastic model used in this section uses the same assumptions as presented in section 3.2: the soft fingers have an hemispherical geometry. The deformations generated in the soft

finger are produced by a rigid object. The deformation is vertical to the soft finger.

This section is divided into six subsections. The first subsection describes the design and construction of the soft fingers. The second part shows the test bench used to acquire the measurements for the characterization. The third subsection describes the characterization of the elastic response of the soft fingers. The fourth part presents the characterization of reduced creep compliance function of the soft fingers. The fifth subsection presents the test made to compare the radius of contact and the deformation. The seventh subsection presents a proposed function to estimated the parameter  $k$ . Finally, the results are analyzed and conclusions are made.

### 3.3.1 Intrinsic tactile system with soft fingertips design and construction

In the state of the art, many artificial soft fingers were created: [Bia+05], [IH03], [XK00] and [XK99]. Most of them are made of polyurethane or silicon rubber. Also, most of them have a hemispherical geometry.

#### 3.3.1.1 Soft fingertips design

For simplicity and to be able to use equation 3.6 of pressure distribution, the geometry of the finger is a hemisphere, as presented in Figure 3.9a.

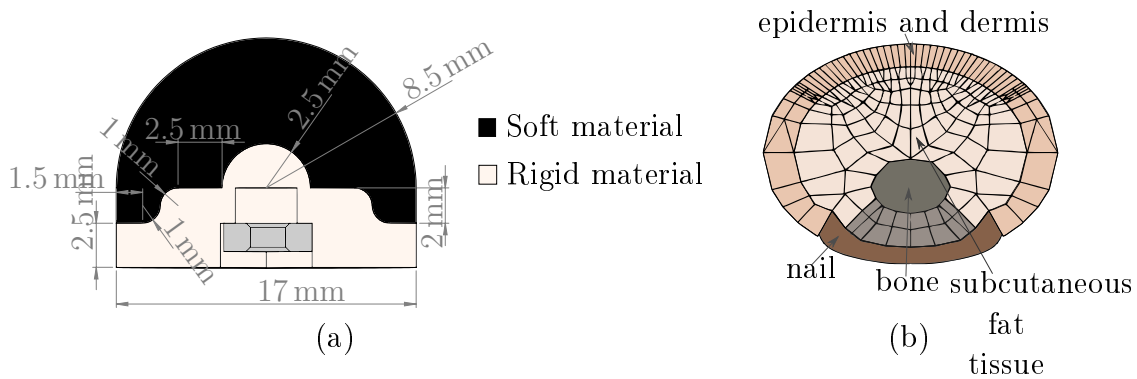


Figure 3.9: Soft fingertips design 1

Additionally, the rigid base is inspired by the human finger, where the bone and the nail create a rigid support for the finger. This finger is mounted on the 6-axis force/torque sensor Ati Nano 17, as shown in Figure 3.10.

The base of the soft fingertips is attached to a nut.

#### 3.3.1.2 Soft fingertips construction

Several soft fingers were constructed. However, for reasons of time, just two different soft fingers are presented in this chapter, as shown in table 3.1. The soft fingers presented were selected because they are made of different materials. Consequently, their physical properties, such as relaxation, are different. The soft finger properties are shown in table 3.1.

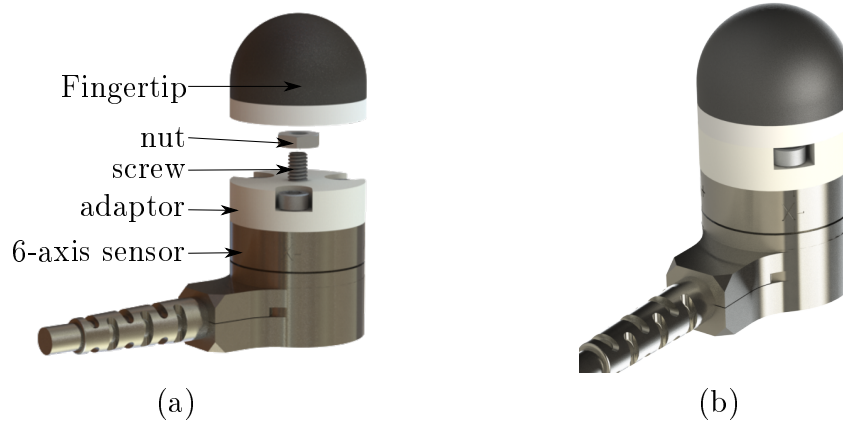


Figure 3.10: Intrinsic system with soft surface

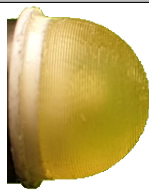

Image	Name	Material	Hardness	Construction
	A	polyurethane	Shore A 40	Mold
	B	SEBS	Shore A 27	3d printing

Table 3.1: Soft finger properties

### 3.3.2 Characterization test bench

In order to characterize the soft fingers, a test bench is made as presented in figure 3.11a and 3.11b. The test bench uses the same structure as that of the systems presented in Annex A.1.1. However, the placement of the precision screw and the motorized table have been changed as presented. Additionally, a rigid acrylic surface is placed on the linear motors. This system allows for the measurement of the distance between the rigid surface and the soft finger with a telemeter sensor of reference ILD1700, which has a resolution of  $0.5\ \mu\text{m}$ . Consequently, by knowing at which distance the soft finger touches the rigid surface, the system is able to measure the deformation of the soft finger  $\delta$ . With the 6-axis force sensor, the system is able to measure the applied forces  $\vec{f}$  and torques  $\vec{\tau}$ . The force resolution is  $1/320\ \text{N}$  and the torque resolution is  $1/64\ \text{N mm}$ .

Furthermore, a camera with a frame rate of 120 frames per second is placed perpendicular to the rigid surface and parallel to the force torque sensor. As shown in figure 3.11c, the camera signal is segmented and some characteristics of the video are subtracted. The red marker helps to estimate the deformation, and the green screen allows to reconstruct the shape of the soft finger as shown in figure 3.11e. After the video processing, the diameter of contact ( $2a$ ) can be estimated as shown in figure 3.11f. The calculated precision of the diameter is  $100\ \mu\text{m}$ .

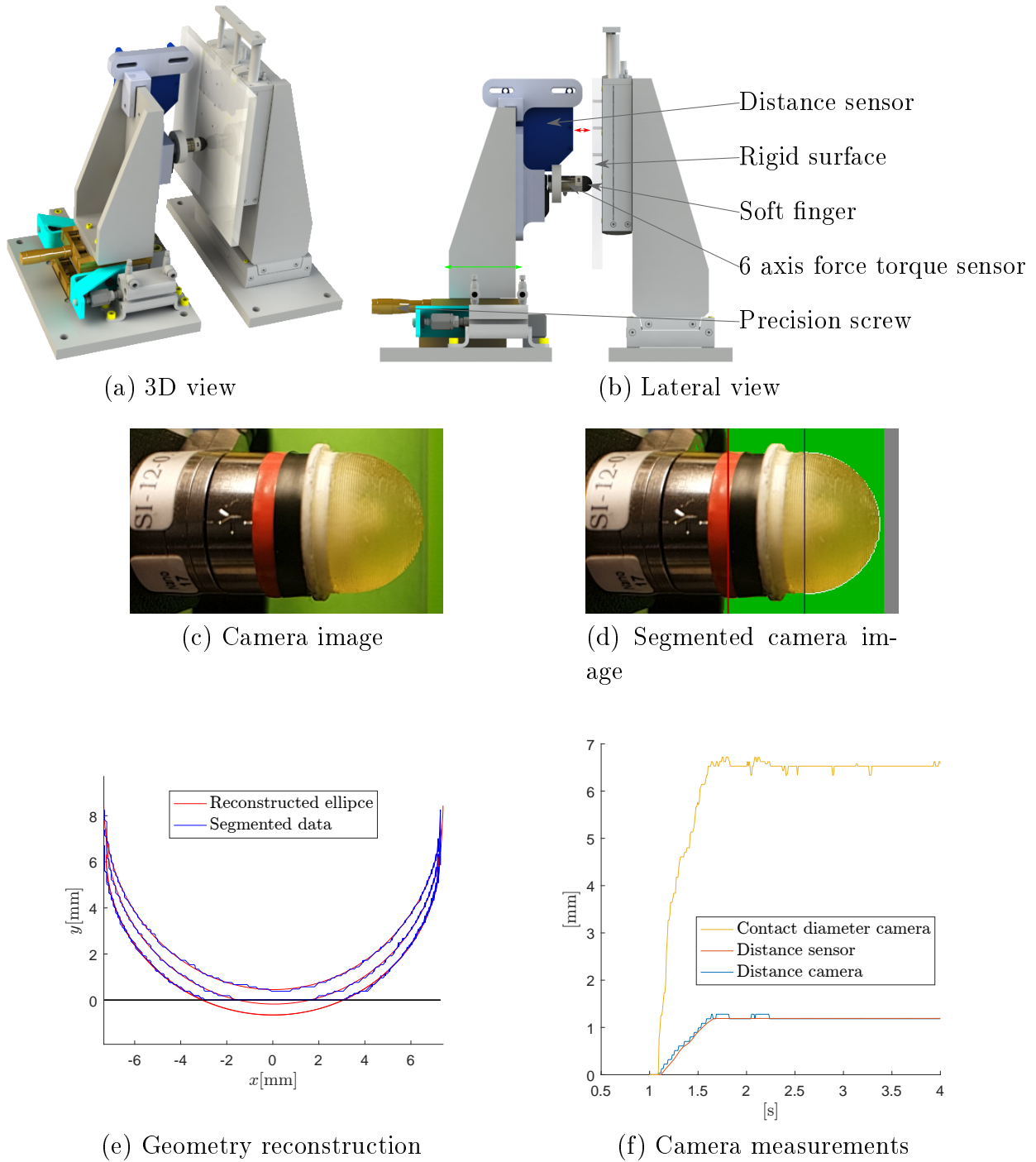


Figure 3.11: Test bench: Viscoelastic characterization

### 3.3.3 Characterization of the elastic response

In order to estimate the deformation  $\delta^{(e)}$  from the normal force  $N$  as presented in the schema 3.12, the characterization of the parameters of the material should be done. For this reason, this subsection presents the characterization of the elastic response.

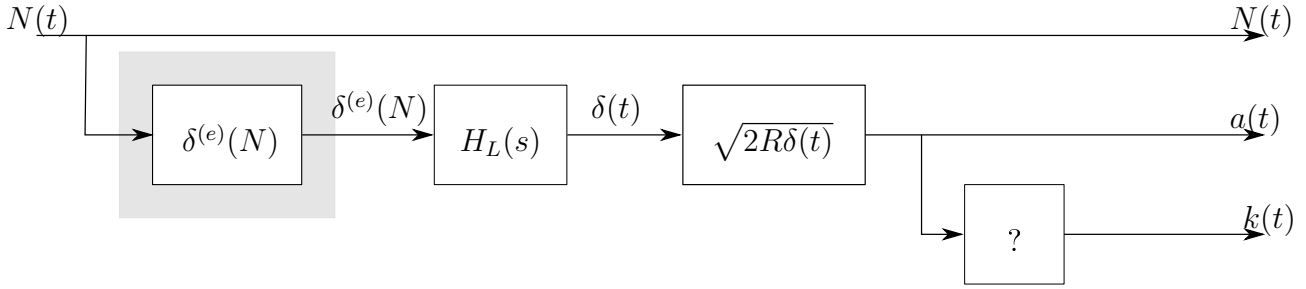


Figure 3.12: Block-scheme representation normal force  $N$  to radius of contact  $a$  and the parameter  $k$  v2

### 3.3.3.1 Characterization parameters

The elastic response of the viscoelastic model of contact is represented by the function  $N^{(e)}(\delta)$ , for the model with imposed displacement. Likewise, the function  $\delta^{(e)}(N)$  represents the elastic response for the model with imposed normal force. The relaxation functions as shown in section 3.2.3 have two different representations. For the first function, the parameters are  $b$  and  $m$ . For the second one, they are  $q$  and  $p$ . Those functions are shown in table 3.2

Table 3.2: Elastic functions

	Parameters	
	$m$ and $b$	$p$ and $q$
Relaxaction	$N^{(e)}(\delta) = \frac{m}{b} (e^{b\delta} - 1)$	$N^{(e)}(\delta) = \frac{p}{q+1} \delta^{q+1}$
Creep compliance	$\delta^{(e)}(N) = \frac{1}{b} \ln \left( \frac{b}{m} N + 1 \right)$	$\delta^{(e)}(N) = \left( \frac{q+1}{p} N \right)^{\frac{1}{q+1}}$

Therefore, the goal of this subsection is to identify the parameters  $b$ ,  $m$ ,  $q$  and  $p$  for each material.

### 3.3.3.2 Calibration method

In order to estimate the parameters of the elastic response the authors in [PH99] and [Bia+05] use a "ramp-hold test". They consider that a fast ramp test could be considered as an step input. By considering that  $g(t=0) = 1$ , the force obtained from a fast deformation is a good approximation of the elastic response. In their experiments the characterized function is  $N^{(e)}(\delta)$ . Therefore, the same experiment is made in this subsection.

The characterization is made by the minimization of the error between the measured normal force  $N_{ref}$  and the calculated elastic response  $N^{(e)}(\delta)$ . Should be said that the estimated parameters of the elastic response  $N^{(e)}(\delta)$  have the same value and physical representation that in the function  $\delta^{(e)}(N)$ .

The minimization is made only in the measured points where the speed of the deformation  $\dot{\delta}$  is larger than  $30 \text{ mm s}^{-1}$ . The minimization functions are shown as following:

$$\{m, b\} = \underset{m, b}{\operatorname{argmin}} \sum_{j=1}^n [N_{ref} - N^{(e)}(\delta)_{\{m, b\}}]^2 \quad (3.46)$$

$$\{p, q\} = \underset{p, q}{\operatorname{argmin}} \sum_{j=1}^n [N_{ref} - N^{(e)}(\delta)_{\{p, q\}}]^2 \quad (3.47)$$

### 3.3.3.3 Characterization methodology

The methodology of the characterization is:

- The soft finger is mounted on the reference sensor
- The system remains without contact for some minutes
- Signal acquisition starts
- Precision screw is rotated to exert forces on the soft finger
- The contact is removed and signal acquisition is stopped

Two measurements using the proposed test bench are made for each soft finger. The first measurement could be in the form of an step of deformation. The second measurement is used as a verification signal.

### 3.3.3.4 Characterization results

The left side of figure 3.13 presents the results for the measurement set used to calibrate the system. The right side of the figure presents the results for the measurement set used to validate the system. As shown in figures of  $\delta$  vs  $N$ , the elastic response shows a good match with the rising edge of the measured force.

As the figure shows, both soft fingers can be modeled with the proposed model. On the one hand, the equation containing the parameters  $m$  and  $b$  is more useful for estimating the force applied in the system A made of polyurethane. On the other hand, the equation containing the parameters  $q$  and  $p$  works better for the printed soft finger.

The estimated parameters for the characterization are shown in table 3.3

Table 3.3: Elastic response  $N^{(e)}(\delta)$  parameters

Name	b	m	q	p
A	1.7391	4.2935	0.9060	22.4296
B	0.8600	3.7035	0.4914	9.0925

In [Bia+05], the estimated parameters of the elastic response for a polyurethane finger are  $b = 2.51$ ,  $m = 0.806$ ,  $p = 0.2636$  and  $q = 2.39$ . Even if the finger used in said study is similar to the finger used in this work, the parameters obtained in the former differ from the estimated parameters presented in table 3.3. This could be because both fingers had different characteristics, for example the rigid support had a different geometry.

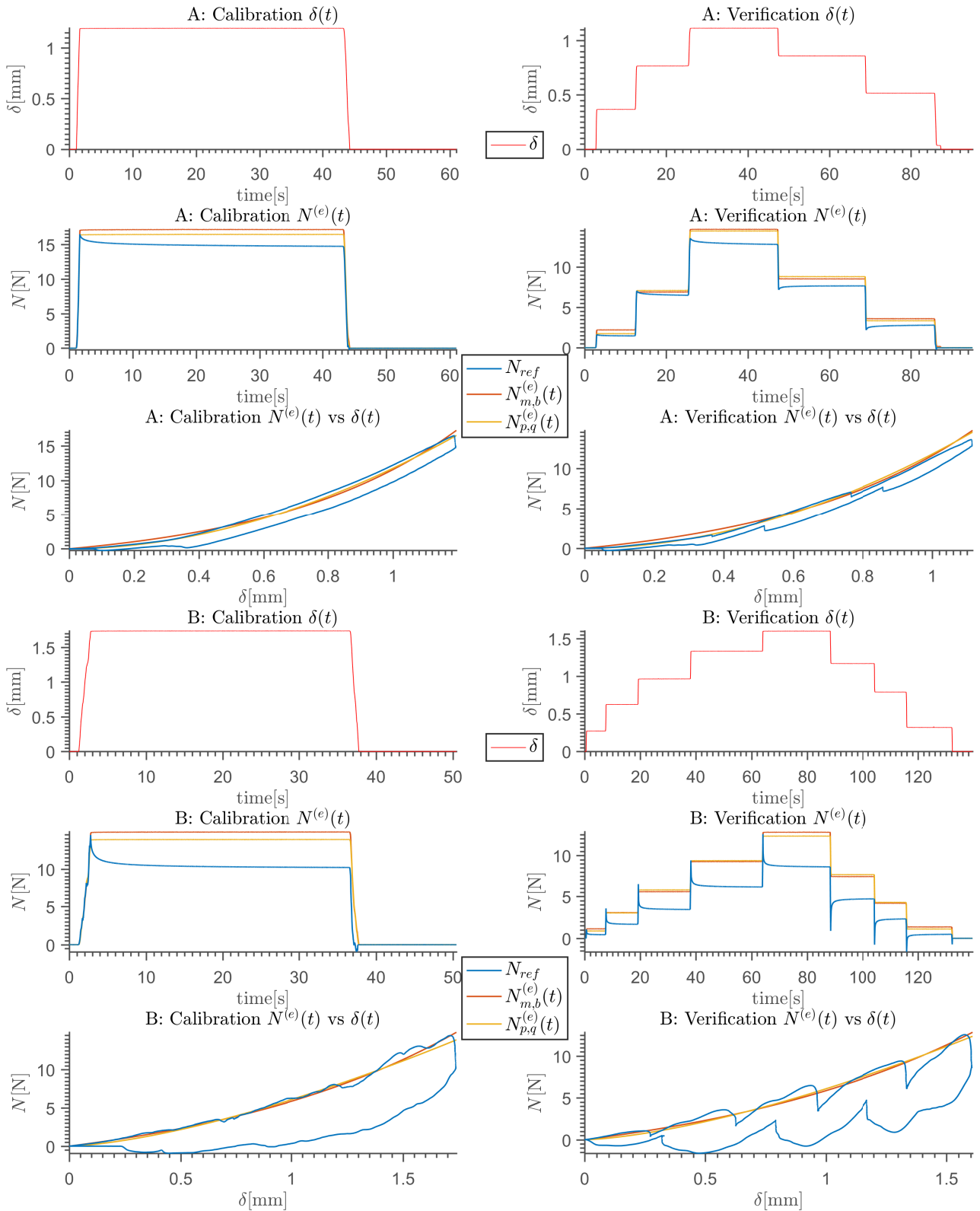


Figure 3.13: Results

### 3.3.4 Characterization reduced relaxation function

The material dependent parameters of the reduced creep compliance function  $h(t)$  should be estimated in order to estimate the total deformation  $\delta$  from the normal force  $N$ . The sim-

plified representation of the relaxation function as shown in figure 3.14 is represent by the function  $H_L(s)$ . Conclusively, this subsection is intended to characterize the temporal response represented by the function  $H_L(s)$ .

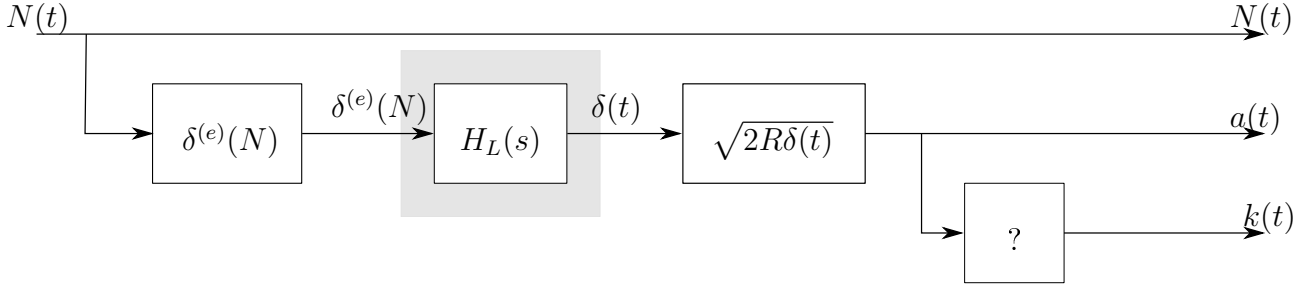


Figure 3.14: Block-scheme representation normal force  $N$  to radius of contact  $a$  and the parameter  $k$  v3

The block representing the function  $H_L(s)$  is shown in figure 3.15.

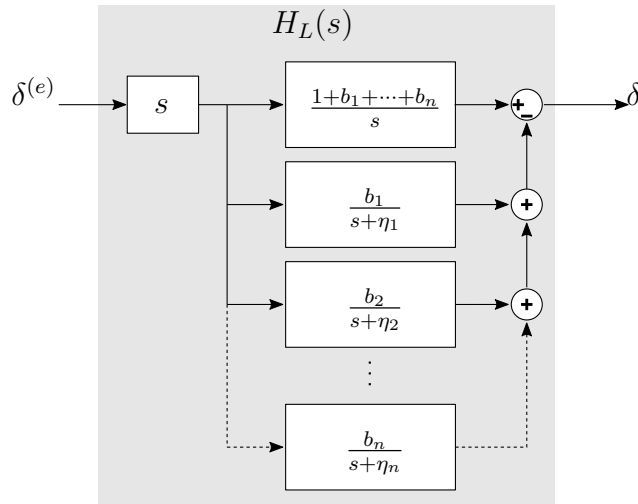


Figure 3.15: Function  $H_L(s)$

### 3.3.4.1 Characterization parameters

The parameters to estimate are the parameters for the reduced creep compliance function  $h(t)$ .

$$h(t) = 1 + \sum_{i=1}^n b_i (1 - e^{-\eta_i t})$$

The parameters are  $b_i$  and  $\eta_i$ . The number of pairs  $i$  change depending in the creep phenomena. In this work the relaxation function  $h(t)$  is characterize for  $i = 1, 2, 3$ .

### 3.3.4.2 Calibration method

The calibration for the reduced creep compliance function  $h(t)$  is done for individually for each group of parameters  $b_i$  and  $\eta_i$  for  $i = 1, 2, 3$ . The elastic response with the parameters  $b$  and  $m$  shown in the equation 3.32 is used to estimate the parameters. Only one elastic response



function is used because when the normal force in equation 3.36 is near zero, the function tends toward infinity.

The characterization is made by the minimization of the error between the measured normal force  $\delta_{ref}$  and the calculated deformation response  $\delta_{cal}$ . The parameters are estimated as shows the following cost functions:

$$\{b_1, \eta_1\} = \operatorname{argmin}_{b_1, \eta_1} \sum_{j=1}^n [\delta_{ref}(j) - \delta_{cal}(j)_{\{b_1, \eta_1\}}]^2 \quad (3.48)$$

$$\{b_1, b_2, \eta_1, \eta_2\} = \operatorname{argmin}_{b_1, b_2, \eta_1, \eta_2} \sum_{j=1}^n [\delta_{ref}(j) - \delta_{cal}(j)_{\{b_1, b_2, \eta_1, \eta_2\}}]^2 \quad (3.49)$$

$$\{b_1, b_2, b_3, \eta_1, \eta_2, \eta_3\} = \operatorname{argmin}_{b_1, b_2, b_3, \eta_1, \eta_2, \eta_3} \sum_{j=1}^n [\delta_{ref}(j) - \delta_{cal}(j)_{\{b_1, b_2, b_3, \eta_1, \eta_2, \eta_3\}}]^2 \quad (3.50)$$

### 3.3.4.3 Characterization methodology

The verification measurements from the previous section 3.3.3 are used as the calibration measurements. Additionally, one measurement using same methodology and test bench is made for each soft finger. The new measurement is intended to test the elastic and temporal response. Therefore, the measurement should have a part where the deformation changes constantly. This allows to test the elastic response. The measurement should have a part where the temporal response is settle for different normal forces.

### 3.3.4.4 Characterization results

The results for the characterization of the soft fingers are shown in figure 3.16.

The left side of figure figure 3.16 presents the results for the measurement set used to calibrate the system. The right side of the figure presents the results for the measurement set used to validate the system.

The estimated parameters for the reduced relaxation function  $h(t)$  are shown in table 3.4.

Table 3.4: Creep compliance function  $h(t)$  parameters

Name	$i$	$b_1$	$b_2$	$b_3$	$\eta_1$	$\eta_2$	$\eta_3$
A	$i = 1$	0.0759			0.0667		
	$i = 2$	0.2653	-0.1964		0.1018	0.11078	
	$i = 3$	0.1282	0.0570	-0.11058	2.7262	0.0522	1105
B	$i = 1$	0.2966			0.9122		
	$i = 2$	0.0816	0.2154		1.2412	0.8038	
	$i = 3$	0.0657	0.0111	0.2167	1.1567	1.8408	0.8071

The normalized root mean square error of the verification measurements is shown in table 3.5. The statistical method is used to qualify the goodness of fit between test and reference data.

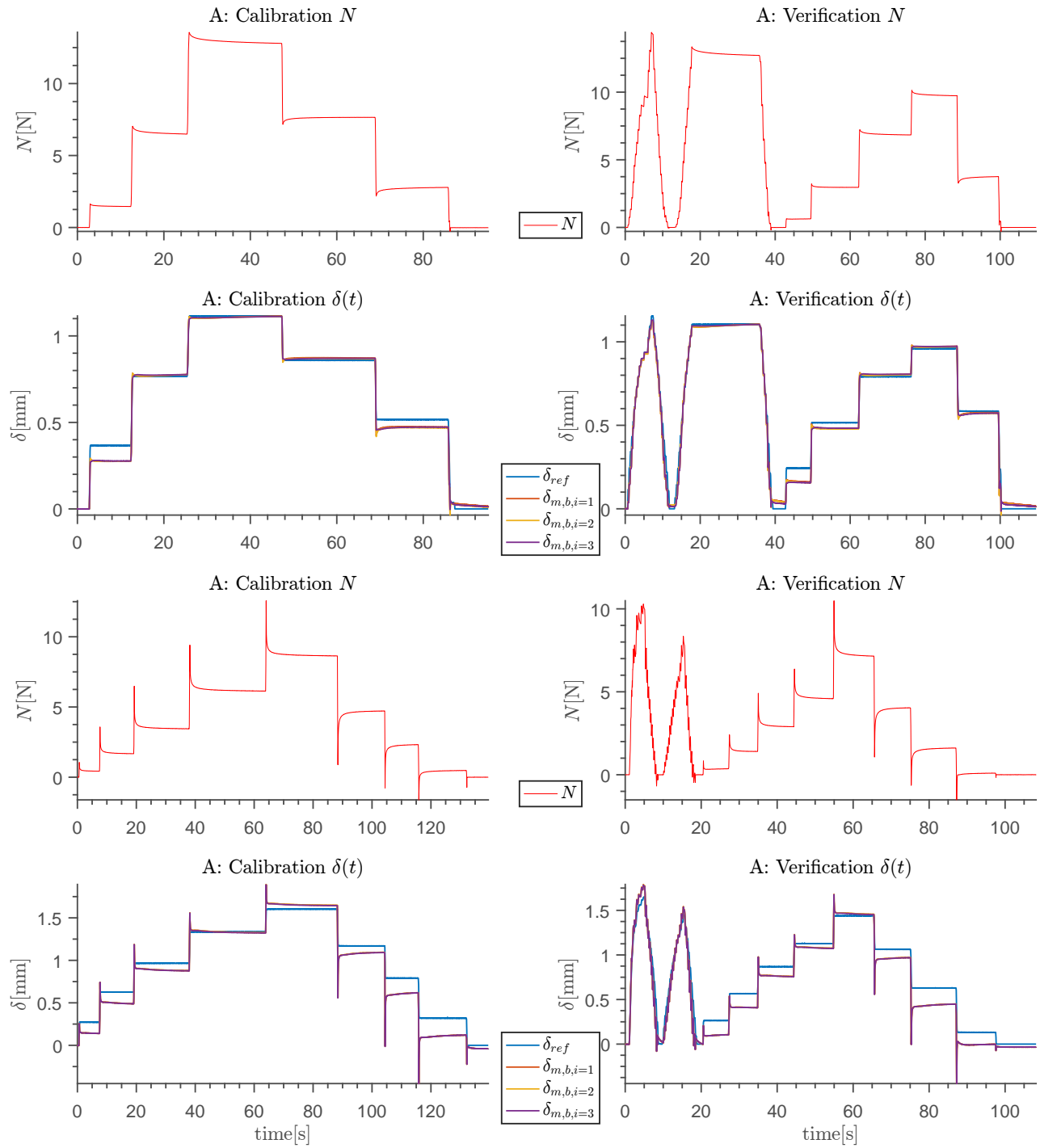


Figure 3.16: Results

The estimated deformation for the finger A made from polyurethane has a good matching with the reference deformation as shown in figure 3.16 and table 3.5.

The estimated deformation for the finger B made by a 3D printer made a regular estimation. The normalized root mean square error is approximately 74.5%. The proposed model does not reduce sufficiently the relaxation effect.

There are not any considerable difference between the different functions  $h(t)$  based on the number of parameters  $i$ .

Table 3.5: Goodness of fit reduced relaxation function (NRMSE)

	Parameters $h(t)$		
	$i = 1$	$i = 2$	$i = 3$
A	90.28%	90.09%	90.31%
B	74.52%	74.57%	74.42%

Table 3.6: Goodness of fit radius of contact (NRMSE)

	$a(t)$ calculated from	
	$\delta(t)_{ref}$	$N(t)_{ref}$
A	91.35%	86.92%
B	92.98%	69.21%

### 3.3.5 Relation between the radius $a$ and the deformation $\delta$ test

As presented in the subsection 3.2.5.4 the authors in [TK07] assume that the relationship between the radius of contact  $a$  and the deformation  $\delta$  is  $a^2 \cong 2R\delta$ . This relation is the simplification of the equation 3.10 ( $a^2 = R^2 - (R - \delta)^2$ ). Therefore, this subsection is intended to test this assumption.

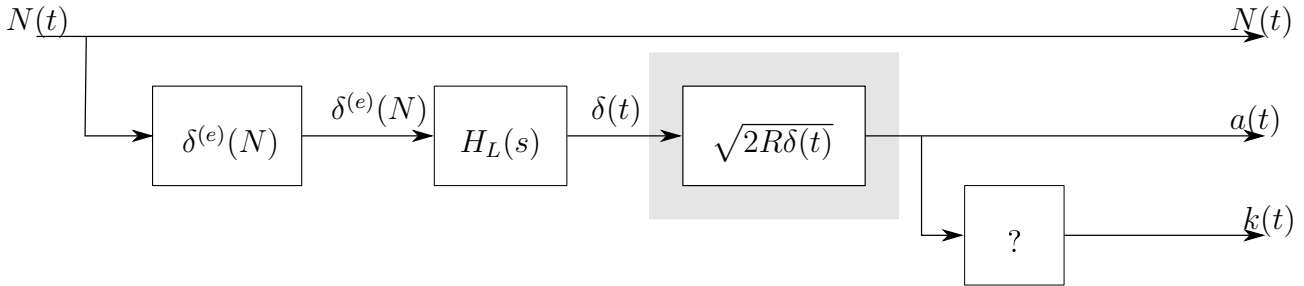


Figure 3.17: Block-scheme representation normal force  $N$  to radius of contact  $a$  and the parameter  $k$  v3

#### 3.3.5.1 Test methodology

The verification signals presented in previous section 3.3.4 are used to test the assumption.

#### 3.3.5.2 Test results

The assumption  $a^2 \cong 2R\delta$  made by [TK07] does not coincide with the experimental data. However, the assumption that the square radius is proportional to the deformation  $a^2 \propto R\delta$  is valid as shown in the figure 3.18.

The proportional parameter  $u$  as shown in equation 3.51 for the two soft fingers is 1.03.

$$a(t)^2 = uR\delta(t) \quad (3.51)$$

The normalized root mean square error of the verification measurements is shown in table 3.6. The statistical method is used to qualify the goodness of fit between test and reference data.

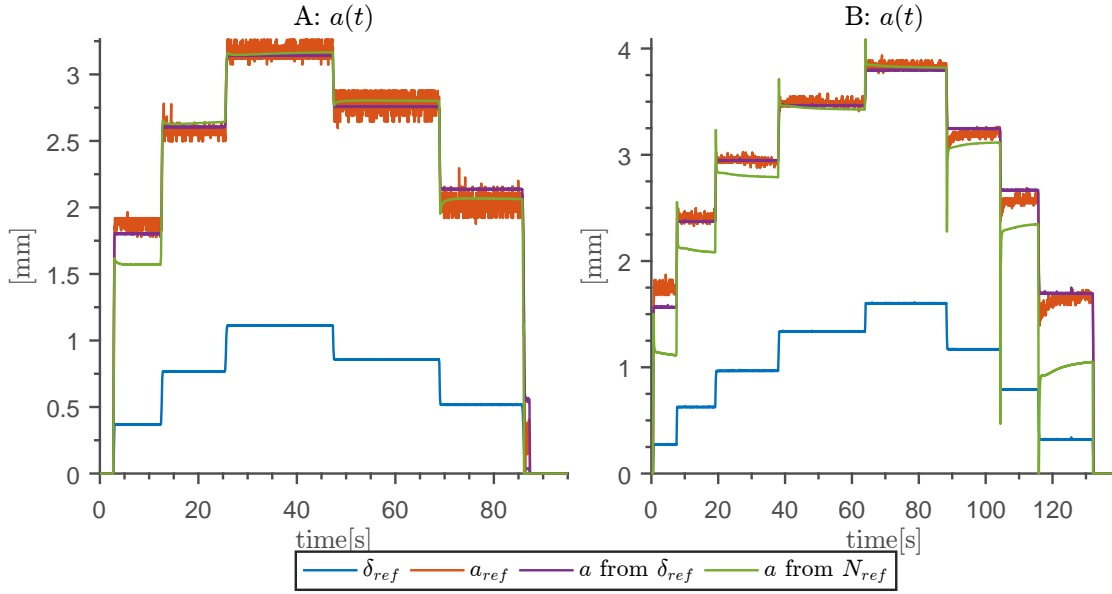


Figure 3.18: Results

As expected the estimation of the radius of contact from the measured deformation shows a good estimation for both fingers.

From the results of the previous section it is known that the maximum accuracy expected is 90% for the finger A, and 74.5% for the finger B. The accuracy to the reference is 90%. Therefore the results presented in table 3.6 are the expected value (diminution in accuracy of 5%).

### 3.3.6 Estimation of the parameter $k$

To estimate the pressure distribution from the normal force is the parameter  $k$  is needed. Therefore, this section is intended to suggest a function of  $k$  in terms of the prior knowledge.

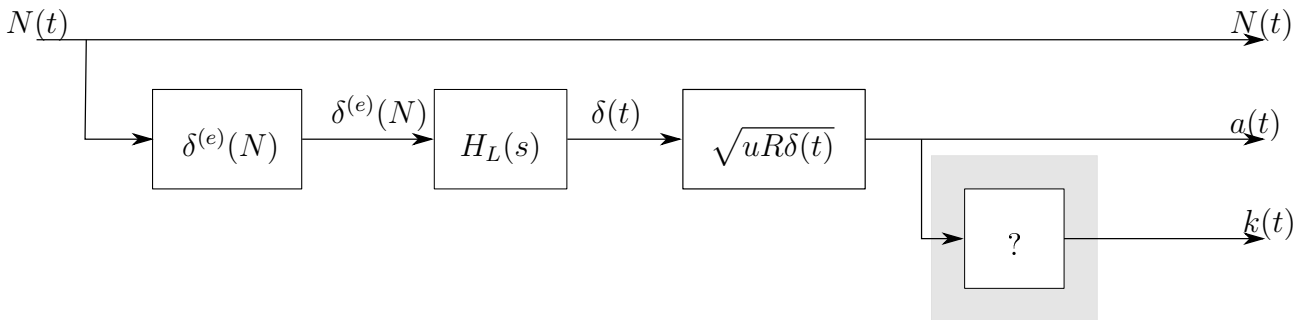


Figure 3.19: Block-scheme representation normal force  $N$  to radius of contact  $a$  and the parameter  $k$  v4

As presented in the subsection 3.2.5.4 the authors in [TK07] assume a correlation between the radius of contact  $a$  and function  $C_k$ . This relation is  $C_k \propto \frac{1}{a^2}$ . They proposed that for an step input of normal force the parameter  $k$  is:

$$k(t) = \left[ \frac{C_{k0}}{h(t)} - 1 \right]^{-0.556} \quad (3.52)$$

where  $C_{k_0} = C_k(k|_{t=0})$ , and  $h(t)$  is the reduced creep compliance function. This function is created for an step normal force as the excitation of the system. The value of  $k$  should be generalized for any kind of input. Consequently, a new function of parameter  $k$  should be introduced.

Additionally to the observations made in the by [TK07] the following observation is made: The parameter  $k$  is related to the creep compliance function as shown in equation 3.52. As presented, the value of  $k$  is minimal when the elastic response is predominant i.e., the normal force is increasing fast. In the other hand,  $k$  increases when there is no change in the contact forces and the material is in the creep response.

If the parameter  $k$  depends on the creep compliance function and is related to the radius of contact  $a$ . Therefore, the calculated area of contact  $a(t)$  compared to the elastic area of contact  $a^{(e)}(t) = \sqrt{uR\delta^{(e)}} [N(t)]$  should reflect the behavior of  $k$  in the time. Figure 3.20 shows the radius of contact  $a(t)$  and the estimated elastic radius of contact  $a^{(e)}(t)$  for the soft fingers.

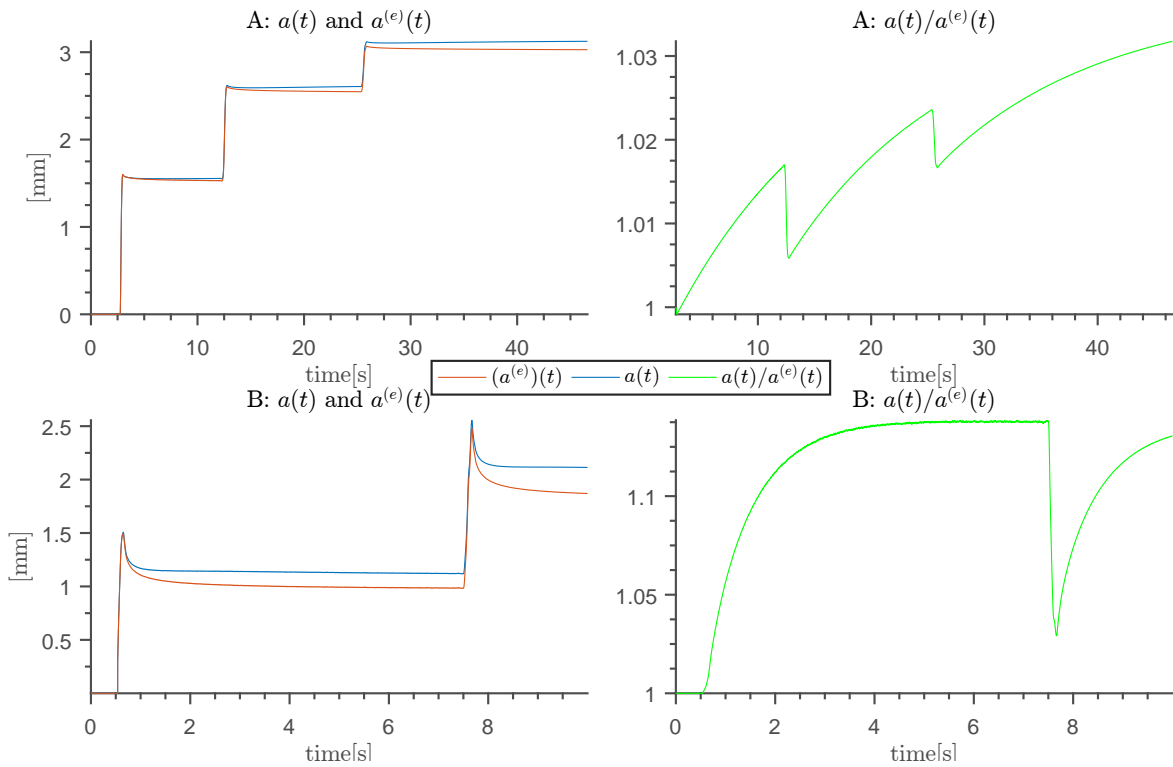


Figure 3.20: Coupling equation illustration

The division  $a(t)/a^{(e)}(t)$  shows the expected behavior of  $k$ . Therefore, a coupling equation is proposed as follows:

$$k(t) = m_k \left( \frac{a(t)}{a^{(e)}(t)} \right) + n_k \quad (3.53)$$

where  $a(t)$  is the estimated radius of contact,  $m_k$  and  $n_k$  are parameter to scale the value. The elastic  $a^{(e)}(t)$  is the radius of contact generated by the elastic response as shown in the following equation:

$$a^{(e)}(t) = \sqrt{uR\delta^{(e)}} [N(t)] \quad (3.54)$$

The values  $m_k$  and  $n_k$  can be estimated by imposing an step normal force as follows:

$$k(t) = m_k \left( \frac{\sqrt{uR\delta^{(e)} [N_0] h(t)}}{\sqrt{uR\delta^{(e)} [N_0]}} \right) + n_k \quad (3.55)$$

$$k(t) = m_k \left( \sqrt{h(t)} \right) + n_k \quad (3.56)$$

When  $h(t)|_{t=0} = 1$  the value of  $k$  is the minimal. Additionally, when  $h(t)|_{t \rightarrow \infty}$  the value of  $k$  is the maximal. The range of values of  $k$  as presented by [TK07] is  $2 \leq k \leq 4$ . The value of the parameters  $m_k$  and  $n_k$  can be estimated by solving the following equations:

$$k(t)|_{t=0} = m_k + n_k \quad (3.57)$$

$$k(t)|_{t \rightarrow \infty} = m_k \sqrt{1 + \sum_{j=1}^n b_j} + n_k \quad (3.58)$$

where  $b_i$  are the parameters of the reduced creep phenomena  $h(t)$  as shown in equation 3.37.

The calculated value of  $k$  for an step input of normal force is shown in figure 3.21

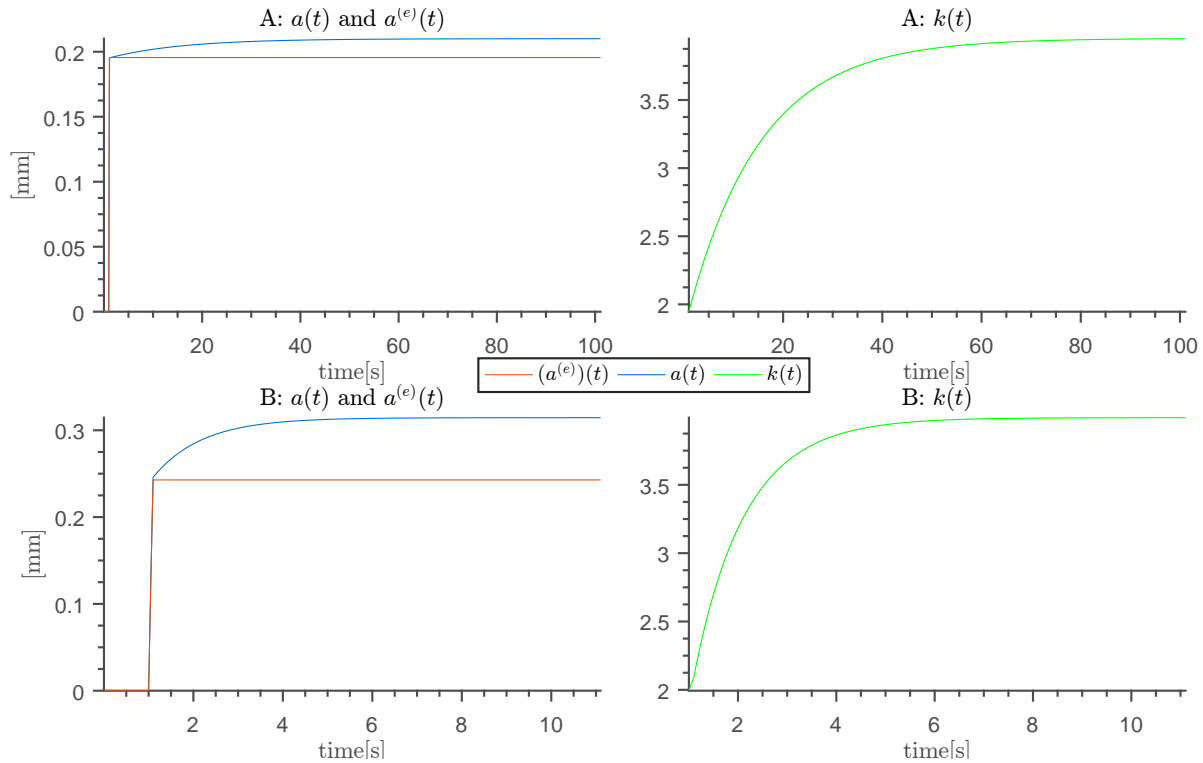


Figure 3.21: Parameter  $k$  estimated to a step input

The estimated parameter  $k$  for the finger A arrive to the stabilization at 60s, this behavior is undesired because the maximal torque is attended when the parameter  $k$  is maximal. The parameter  $k$  for the finger B have a stabilization time of 6s, ten times faster than the finger A. However, an ideal soft finger should have a faster stabilization time.

It should be noted that the proposed equation estimate correctly the value of  $k$  when the forces are increasing. When the forces are decreasing the behavior of the material is different as shown in [TK09].

### 3.3.7 Conclusion

This section presents the characterization of the parameters for the elastic function, creep compliance function and  $a^2 = uR\delta$ . Additionally, a function is proposed, that function relies the radius of contact  $a$  and the parameter  $k$ . Those presented functions allow to estimate the radius of contact  $a$  and the parameter  $k$  in function of the normal force  $N$  and the time  $t$  as figure 3.22 shows:

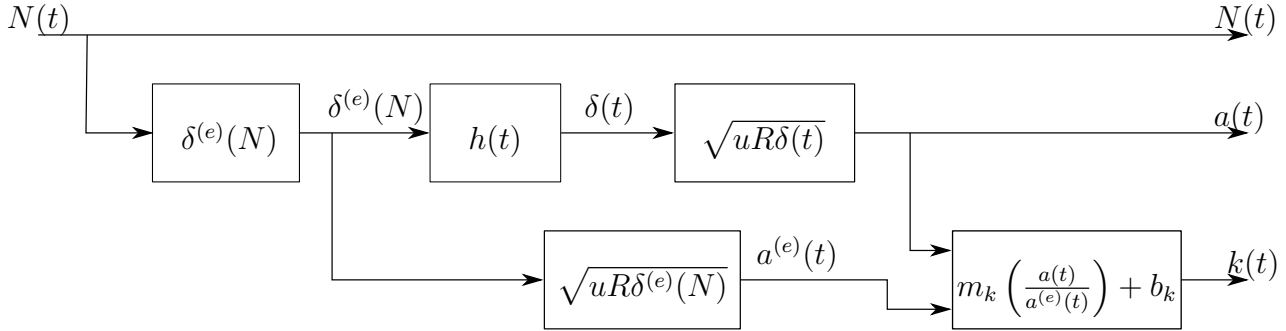


Figure 3.22: Block-scheme representation normal force  $N$  to radius of contact  $a$  and the parameter  $k$

As presented in the section 3.2.2, the pressure distribution depends on the normal force  $N$ , the radius of contact  $a$  and the parameter  $k$ . With the characterization presented in this section it is possible to estimate the radius of contact  $a$  and the normal force is directly measured. For the parameter  $k$  an assumption between  $k$  and  $s$  is proposed.

The viscoelastic model used in this section uses the same assumptions as presented in section 3.2: the soft fingers have an hemispherical geometry. The deformations generated in the soft finger are produced by a rigid object. The deformation is vertical to the soft finger.

The accuracy of the model for the finger A it is appropriate to be implemented. However, the model for the finger B should be changed, the finger B does not behave as a viscoelastic finger.

Conclusively, after the characterization of the soft fingers, the following section is intended to the implementation of the presented models to detect the slippage.

## 3.4 Slip detection using limit surface

In the previous section, the characterization of the soft fingers allows to estimate the radius of contact  $a$  and the parameter  $k$  from the normal force measurement  $N$ . Consequently, pressure distribution can be calculated for every instant of time, which, in turn, allows for the estimation of the limit of friction for every instant of time in accordance with the friction limit theory.

This section is intended to implement limit surface theory on an intrinsic tactile system with soft surface. The assumptions made for this integration are the same as presented in section 3.1 and 3.2. The assumptions are: the soft fingers have an hemispherical geometry. The deformations generated in the soft finger are produced by a rigid object. The deformation is vertical to the soft finger. A body undergoes fully developed sliding on a locally planar surface. The distribution of normal force (or pressure) across the contact surface is known. Friction force depends only on the local normal force applied and on slip direction, but not on the magnitude of slip velocity or slip history.

In order to establish a comparison, the estimated models for both fingers are tested.

This section is divided into four subsections: The first part describes the design and construction of the soft fingers. The second part shows the characterization made to the soft fingers based on the viscoelastic model of contact. The third subsection reports the implementation of limit surface theory for early slip detection on an intrinsic tactile system. Finally, the results are analyzed and conclusions are made.

### 3.4.1 Slippage test bench

In order to test the limit surface friction limit for the proposed intrinsic tactile system, it is necessary to test different types of slippage produced by different tangential forces and torques. Thus, a test bench is created as shown in figure 3.23a.

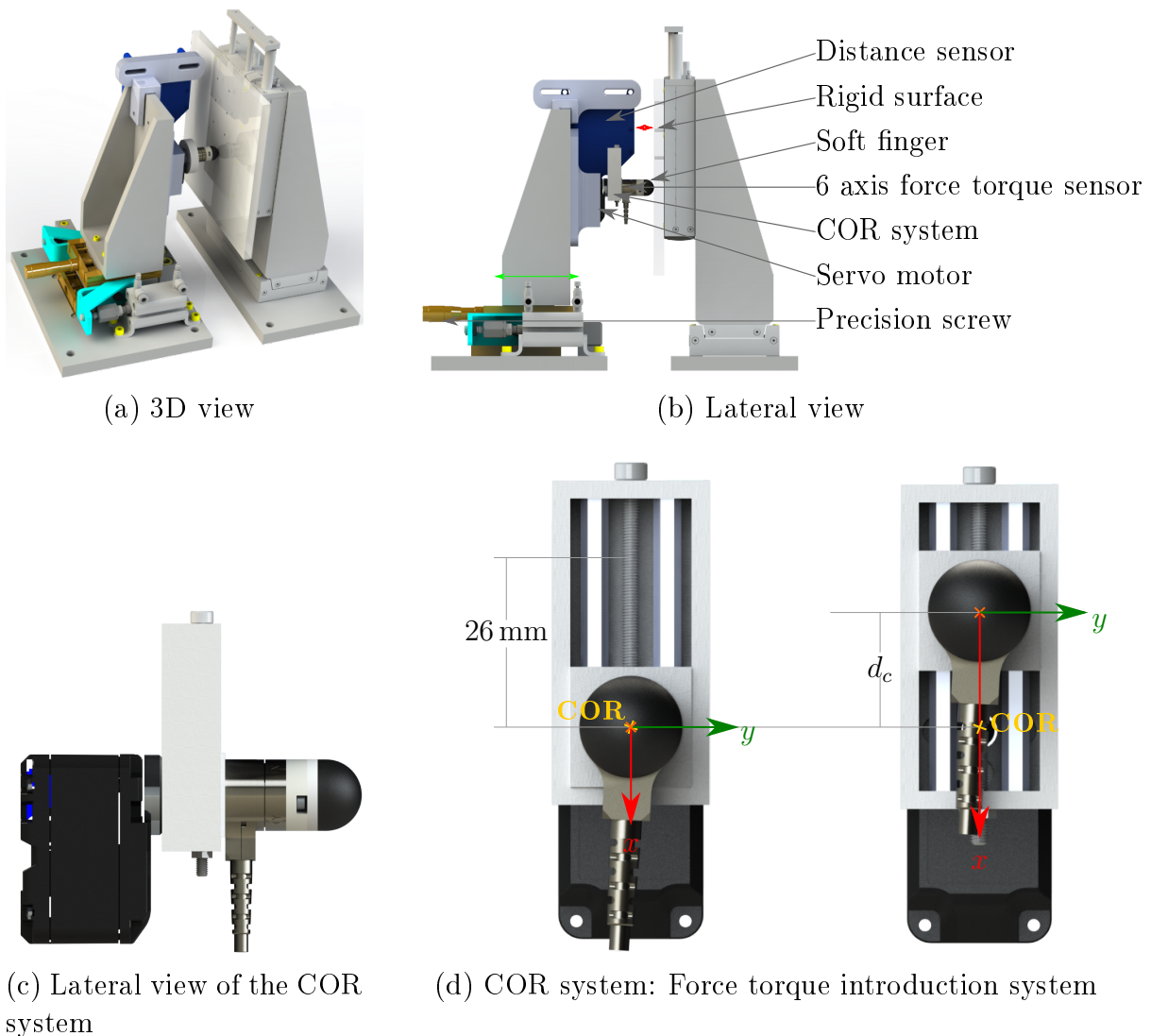


Figure 3.23: Test bench: Slip detection

This system is similar to the one presented in the previous section. The main difference is that the support of the 6-axis force sensor is modified as shown in figure 3.23c. The new support is a system composed of a servomotor and a mobile platform. The support is called COR system



because the distance between the rotation axis of the servomotor and the sensor can be set by the screw, as shown in figure 3.23d. This system allows for the induction of slippage with different tangential forces and torques. The system is inspired by the construction of the limit surface as presented in section 3.1.

### 3.4.2 Construction of the limit surface

The construction of the limit surface for the case presented here, where the contact area is constant and circular, can be expressed as follows ([XK99]):

$$f_f = \frac{\mu N}{\pi} \int_0^{2\pi} \int_0^a \frac{r^2 \cos \theta - r d_c}{\sqrt{r^2 + d_c^2 - 2r d_c \cos \theta}} \frac{C_k}{a^2} \left[ 1 - \left( \frac{r}{a} \right)^k \right]^{\frac{1}{k}} dr d\theta \quad (3.59)$$

$$\tau_f = \frac{\mu N}{\pi} \int_0^{2\pi} \int_0^a \frac{r^3 - r^2 d_c \cos \theta}{\sqrt{r^2 + d_c^2 - 2r d_c \cos \theta}} \frac{C_k}{a^2} \left[ 1 - \left( \frac{r}{a} \right)^k \right]^{\frac{1}{k}} dr d\theta \quad (3.60)$$

Those equations are the result of combining the pressure distribution from equation 3.41 in the equations of limit surface 3.4 and 3.5. Additionally, the vector  $\hat{v}(\vec{r})$  represented in the equation 3.3 is calculated as:

$$\hat{v}(\vec{r}) = \frac{r \cos \theta - d_c}{\sqrt{r^2 + d_c^2 - 2r d_c \cos \theta}} \quad (3.61)$$

For further information see [XK99] and [TK07].

### 3.4.3 Experiment

The methodology of the experiment is the following:

- The soft finger is mounted on the reference sensor, and the distance between the sensor and the axe of the motor is fixed
- The system remains without contact for some minutes
- Signal acquisition starts
- The precision screw is rotated to exert forces near 5 N on the soft finger
- The axe of servomotor is rotated 45 degrees
- Contact is removed and signal acquisition is stopped

Twenty measurements are made for each soft finger. Each measurement is made at a known distance as shown in table 3.7

Table 3.7: Distances from the COR

#	1	2	3	4	5	6	7	8	9	10	11	12	13	114	15	16	17	18	19	20
$d_c$ [mm]	0	0.5	1	1.5	2	2.5	3	4	5	6	7	8	9	10	12	14	16	18	20	26

### 3.4.4 Results and analysis

This subsection presents the results of the proposed experiment.

#### 3.4.4.1 Reconstruction the limit surface experimentally

Figure 3.24 shows the measurement of the frictional force  $f_f$ , the normal applied torque  $\tau_N$ , and the curve  $f_f$  vs  $\tau_N$  for the 20 measurements for both soft fingers. The results are presented synchronized and the starting point is the time when the motor started to exert forces on the soft finger.

The graph  $f_f$  vs  $\tau_N$  for both soft fingers clearly shows the limit surface. It should be noted that, since the normal force was applied manually to 5 N, the curve is an approximation.

The proposed test bench does not provide the displacement measurement and hence the moment when the object slips is estimated. Three different methods were applied to estimate the moment when slippage occurred: the maximum friction force, the maximum normal torque, and the maximum value of the magnitude of the vector composed by the frictional force and the normal torque. The results are shown in figure 3.24.

It could be said that the system starts to slip approximately 2 seconds after the motor starts to exert the forces. It should be noted that the maximum normal torque always happens before the maximum frictional force. The maximum frictional force and normal torque behave in two separate ellipses. This behavior is well noticed in the limit surface of the soft finger A. There is a linear behavior until the maximum normal torque occurs.

As expected, the maximum frictional force works well to identify slippage for the measurements with the biggest distance  $d_c$  to the center of rotation. Likewise, the maximum normal torque is a good indicator for identification of slippage in the case of measurements with the smallest  $d_c$ .

The maximal measured torque in soft finger B is bigger than in soft finger A. This behavior can be explained by the coefficient of friction  $\mu$  and the difference of material. Since the material finger B is made of is softer than that of finger A, the radius of contact of the former is greater.

#### 3.4.4.2 Evolution of the pressure distribution and the limit surface

Figures 3.25 and 3.26 show the measurement of the normal force  $N$ , the radius of contact  $a$ , the shape parameter  $k$ , the evolution of pressure distribution, as well as the evolution of the estimated limit surface for three measurements for each soft finger. The coefficient of friction is not calculated. Subsequently, the calculated limit surface is divided by the coefficient of friction.

The points shown in the figures represent the different times when pressure distribution and limit surface are calculated for the representation. The color variation helps to follow the time line.

It can be seen that the radius of contact of finger B is greater than that of finger A for the same applied force. This behavior can be explained by the different hardness of the materials. As a consequence, the maximal supported torque is higher for finger B.

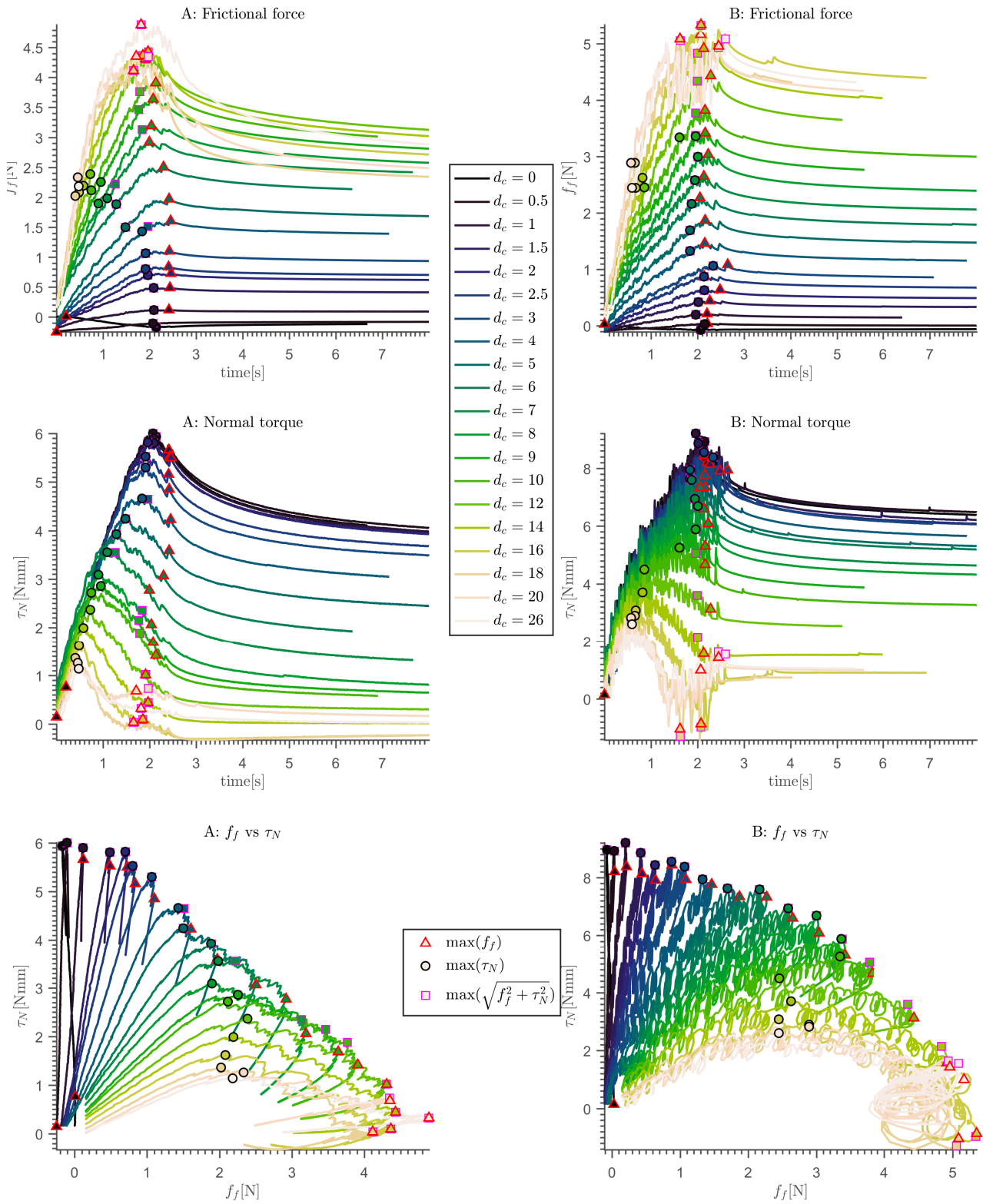


Figure 3.24: Frictional force  $f_f$  and normal torque  $\tau_N$

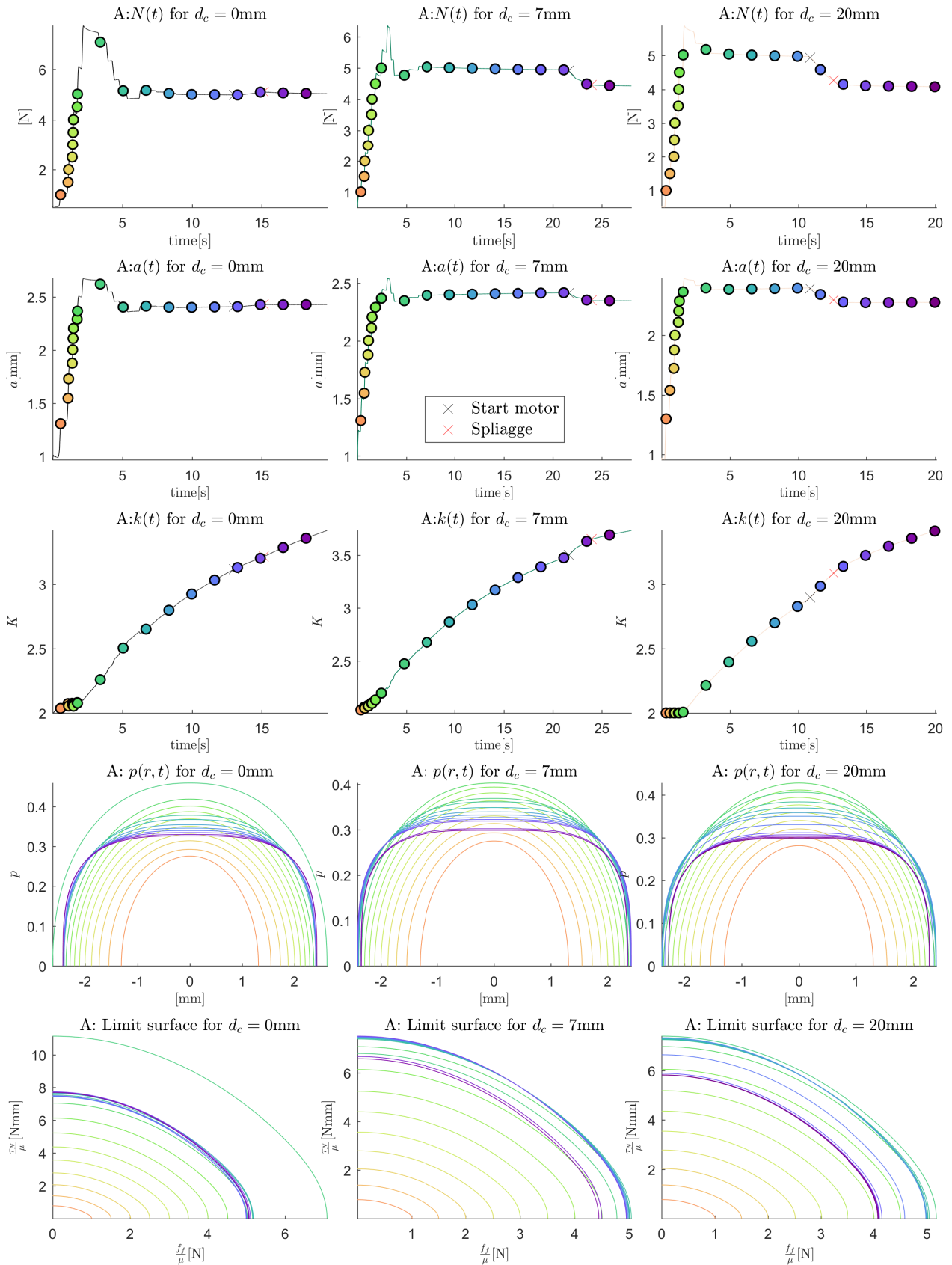


Figure 3.25: Pressure distribution and limit surface for the finger A

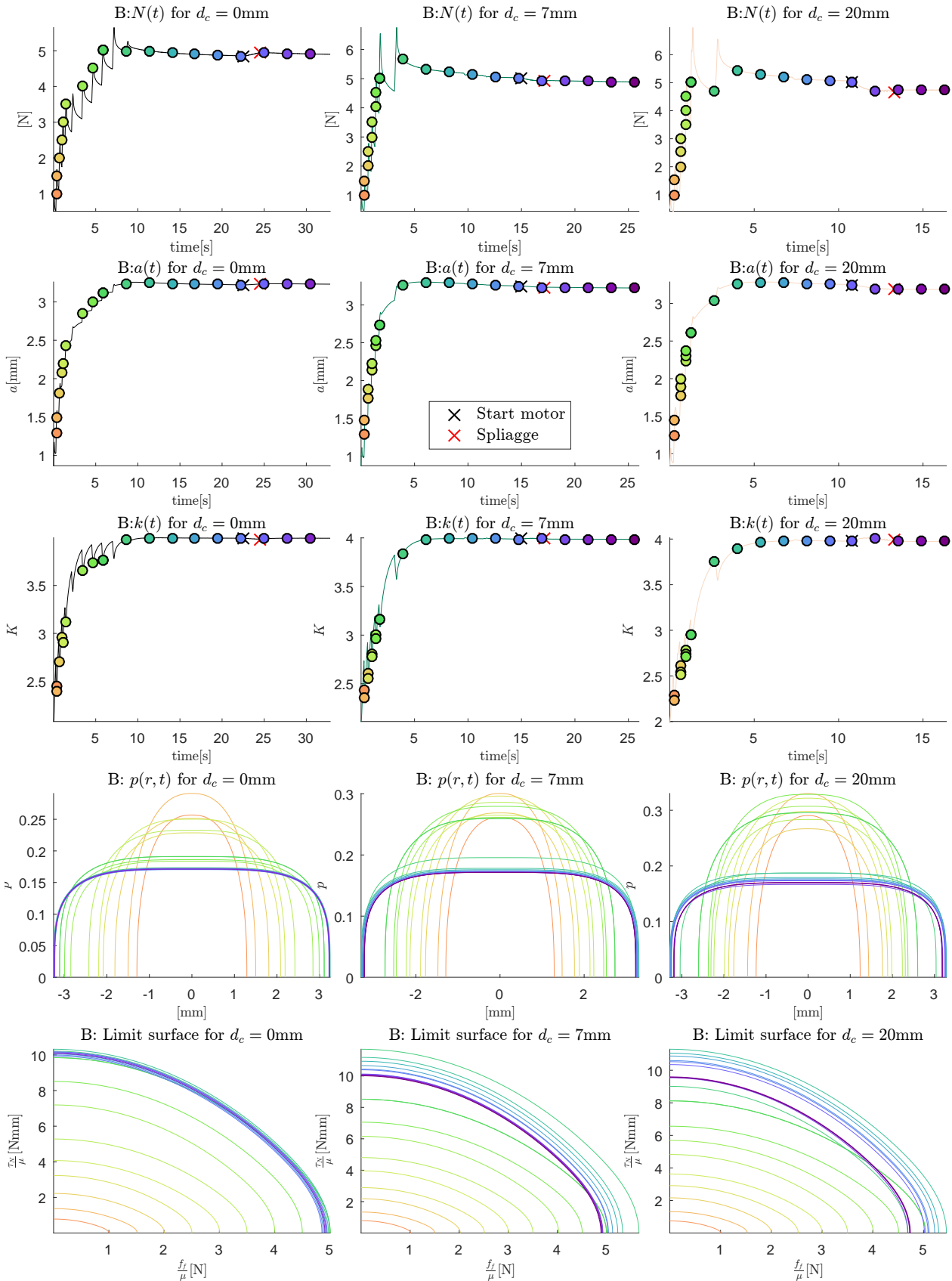


Figure 3.26: Pressure distribution and limit surface for the finger B

### 3.4.5 Conclusion

This section presents the integration of the limit surface friction limit in an intrinsic tactile system. The proposed model that estimates the radius of contact and the parameter  $k$  from the normal force is applied to estimate the pressure distribution. Thus, limit surface can be calculated at every instant. The implementation in real time would depend on limit surface integrals computational time represented in equations 3.59 and 3.60.

The assumptions made for this integration are the same as presented in section 3.1 and 3.2. The assumptions are: the soft fingers have an hemispherical geometry. The deformations generated in the soft finger are produced by a rigid object. The deformation is vertical to the soft finger. A body undergoes fully developed sliding on a locally planar surface. The distribution of normal force (or pressure) across the contact surface is known. Friction force depends only on the local normal force applied and on slip direction, but not on the magnitude of slip velocity or slip history.

As presented in [TV05] and shown in figures 3.25 and 3.26, when contact is established, the surface of contact and the parameter  $k$  are larger than when contact starts. As a result, the supported torque is bigger when creep behavior is established. Therefore, the ideal soft finger should attain its maximal area of contact with maximal pressure distribution as fast as possible. In this case, the model of finger B is better equipped for dexterous manipulation of objects.



# Conclusion and perspectives

The presented work has treated two main subjects related to tactile sensing system for robotic dexterous manipulation of objects. The first subject was the development of an artificial tactile sensing system suited for the integration in a robotic anthropomorphic manipulator and based on CEA-LETI's 3-axis force sensors. The second subject was the analysis of object slippage during the manipulation in order to prevent damaging the object either by letting it slide or by applying unnecessarily high grasp force.

The work was divided in three parts: protection of multi-axis force sensors, design and construction of intrinsic tactile systems, slippage analysis with an intrinsic tactile system.

A bibliographic review showed the necessity of applying a coating to the CEA-LETI's sensor before integrating it in a tactile system. The objective is protect it and increase the range of forces that can be supported by the sensor. The 3-axis force sensor was characterized in order to compare its properties before and after applying the protection. Five different coatings with different shapes, sizes and materials were tested and characterized in order to show the coating's effect. The results revealed some guidelines to be followed in order to obtain an appropriate coating. In fact, the shape of the coating must be symmetrical, and centered with respect the center of the sensitive area. The tip of the protection must be pointy to assure that the forces are applied in a specific zone. To achieve these conditions, it is advised to use a molding process instead of material deposit. The polyurethane shore 40 showed more promising properties compared to polyurethane shore 80. Finally, the dynamic range was verified for the chosen coating. At this stage, the sensor was ready to be implemented in a tactile sensing system for dexterous manipulation of objects.

In order to integrate the 3-axis force sensor in a tactile system, a bibliographic review detailing the different kinds of tactile systems was presented. It has shown that the intrinsic tactile systems are the most suitable for this sensor. Before creating a touch system adapted to dexterous manipulation, a first proof of concept system was implemented. The system is based on an array of three coated 3-axis force sensors fixed in a triangular arrangement. A flat rigid touch surface is glued on top of the sensors. This is an intrinsic tactile system able to measure the three components of the force, the three components of the torque perpendicular to the sensitive surface, and the position of the centroid of forces applied to the sensitive surface. Three different experiments were done to characterize the tactile system. The experiments has shown a mean error for position estimation of 0.7 mm (with standard deviation of 0.372 mm) and a mean error in force estimation of 31.9 mN (with standard deviation of 12.8 mN).

Once the concept was proven, an intrinsic tactile system was built for the integration in an anthropomorphic robotic gripper was designed and characterized. This system fulfills most of the requirements of dexterous manipulation of objects. The experiments on this system has shown that the estimation of force had the same statistics compared to the previous system. However, the position estimation accuracy was improved: The maximum measured error in position is 621.04  $\mu\text{m}$  and the RMSE is 141.21  $\mu\text{m}$ . The maximum measured error in force is 240.57 mN and the root mean square error (RMSE) is 41.47 mN.

For dexterous manipulation of objects, it is necessary to predict whether the manipulated object will slip in order to adapt the grip. The last part of this work dealt with the detection of slippage on an intrinsic tactile sensing system. Several theories could be used to detect the slippage. In this work, the limit surface theory was chosen. This theory requires the knowledge



of the distribution of pressure. The viscoelastic model for soft fingers makes it possible to estimate the distribution of pressure from the measurement of the normal force, the radius of contact, and a shape parameter. The area of contact and the shape parameter could also be estimated from a function of the normal force, time, and the material properties.

Consequently, two soft fingers with different materials and the same hemispherical geometry were created and characterized based on the viscoelastic model. The results are promising as the characterization with the viscoelastic model fits the data by 90% for the first finger and by 75% for second finger. In order to estimate the pressure distribution, two equations were proposed. The first one links the deformation to the radius of contact. And the second one estimates the shape of the distribution of pressure. The experiments assumed that the soft fingers have a hemispherical geometry, the deformations generated in the soft finger are produced by a rigid object and the deformation is perpendicular to the contact surface.

The characterization allowed the estimation of the pressure distribution in real-time which enables the estimation of the limit of friction at any moment. The estimations of the friction limit surface were based on the following assumptions: A body undergoes fully developed sliding on a locally planar surface. Friction force depends only on the normal component of the local applied force and the slip direction assuming that the coefficient of friction is known. The experiments show that the friction limit can be calculated for every instant of time with an intrinsic tactile system.

This work was developed with the available resources at each experiment. Therefore, some experiments could be improved for a better accuracy. For example, the intrinsic systems created in chapter 2 was calibrated with a 3-axis force sensor which could not be used to calibrate the torque estimation. Consequently, a direct comparison with a 6-axis force-torque sensor could give a more accurate vision of the capabilities of the proposed system.

Being able to directly measure the distribution of the pressure is important to test the different propositions. Further work can focus on analyzing the pressure distribution for example by using an extrinsic pressure array.

To create an improved tactile system, the developed intrinsic system could be implemented with a soft surface that integrates an extrinsic system. The extrinsic system would measure the pressure distribution which reduces the number of hypothesis needed to resolve the slip detection problem. The soft surface should have the right balance between softness and robustness. A special attention should be given to temporal response speed of the soft surface. Such hybrid tactile system would be able to estimate the applied forces, the applied torques, the position of contact, the distribution of pressure and the area of contact. This system could estimate the limit surface without any assumption. Therefore, the slippage prediction could be easily applied using the limit surface theory.

In other perspective, the limit surface could be used as a control strategy. In fact, the limit surface theory enables estimating the evolution of the contact in time. Therefore, the normal applied force can be adjusted according to the distance between the actual state in the frictional force versus normal torque diagram and the calculated limit surface.

# Test system

## A.1 Measuring devices

In the presented work two the following measuring systems are used.

### A.1.1 Two axis force measurement system

The measurement system has been used by [Db10], and it was designed with the concern of accurately controlling the movement and minimize external vibration in order to recognize textures. This device can measure the normal force and one tangential force exerted on an end effector. The machine was made by Nominal Concept, an outside consulting firm to CEA specializing in the production of precision mechanical devices. The measurement system is shown in figure A.1.

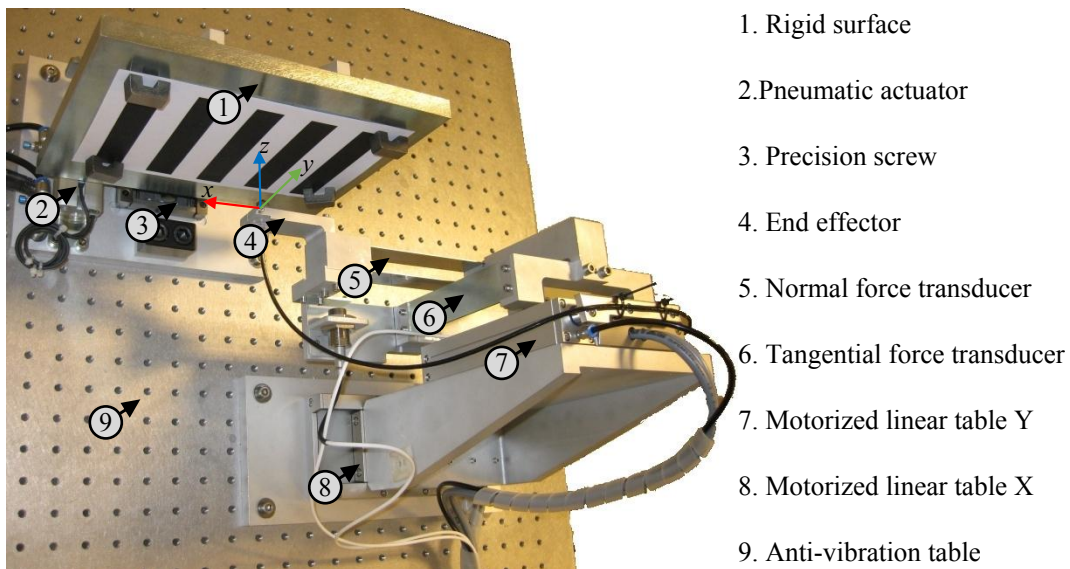


Figure A.1: Two axis force measurement system

In order to eliminate external vibrations during manipulation, the assembly is mounted on a foamed marble supported by an air vibration frame (Thorlab). The measurement system is composed of two motorized linear tables (Lx80F40 Linax Jenny Science) for moving the end effector along the two axes  $x$  (horizontal),  $y$  (vertical) as shown in figure A.1. These linear table is equipped with an optical rule which allows to control the position with an accuracy of  $1\ \mu\text{m}$  over a length of 8cm. On the vertical motorized linear table an arm is fixed, and this table is equipped with a pneumatic compensator that allows to relieve the weight of the arm. The Lx80F40 tables can withstand a maximum force of opposition to the movement of 40 N. Each table is connected to a controller Xenax (Jenny Science), itself connected to a computer via an

Ethernet cable. Thus, it can independently program the movement of each of the tables, with the disadvantage of not having feedback of the position in time.

The arm consists of two force transducers, made of bimetal springs mounted in series. The first force transducer measures the tangential force along the x-axis. The second force transducer measures the normal force along the z-axis. The operation of the cantilevers is presented later in this appendix.

The rigid surface is a steel plate, mounted on a pneumatic actuator that makes it move forward or backward in the z-axis. The plate can also move via a precision screw and it is placed in front of the end effector. In the past, this plate served to position different samples of textures. However, in this investigation the plate exerts forces on the elements located in the end effector. The forces in the z-axis occur by the movement of the plate through the precision screw, and the tangential forces through the friction created by the movement of the linear tables.

#### A.1.1.1 Characterization of the force transducers

The objective of the system is to measure the normal force and tangential force in stationary position during the movement of the sensor (dynamic). This model of the system is a second order mass spring damper as shown in Figure A.2. This same model can be applied to both transducers.

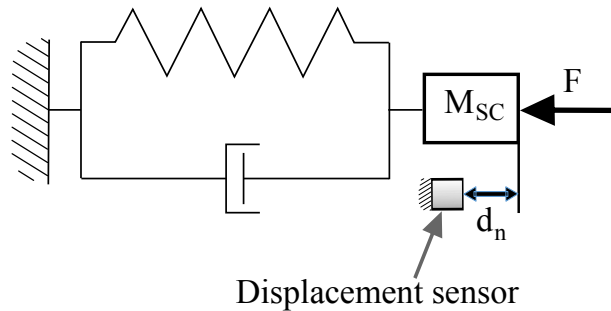


Figure A.2: Second order mass spring damper

**Stationary characterization** In the first instance, the system is assumed to be the free end of a spring subjected to a force. The operating principle of the system is to measure the displacement of the springs. A proportional relation  $F = kx$  links the displacement  $x$  from the free end to the normal force  $F$  applied at this point, via the stiffness  $k$ . The single spring is usually used, for example in the Atomic Force Microscopes, and it has the disadvantage of changing the orientation of the tangential plane at the free end with the bending of the spring. In our assembly, the consequence would be changing the orientation of the end effector based on the contact force, and modifying the directions of the applied forces.

The use of two springs embedded at each end keeps the parallelism between the embedding plans, thus maintaining the end effector in a constant orientation. Figure A.3 shows the behaviour of a two-spring system subjected to a normal force  $F$ . The distance  $d_n$  of the free end is proportional to the applied force. Equation A.1 is used to roughly estimate the stiffness  $k$  of the two-spring system according to the length  $L$ , width  $b$ , thickness  $e$  and the Young's modulus  $E$  of the material.

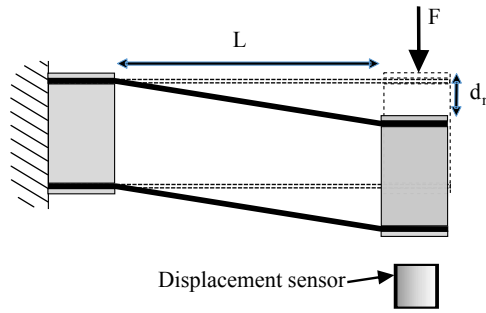


Figure A.3: Force transducer operating principle

$$k = \frac{Ebe^3}{L^3} \quad (\text{A.1})$$

In the two-spring system, each spring is made of a metal sheet. The sheet is perpendicular to the axis of the force to be measured; in this way deformations in the other two axes are minimal. Characteristics of the sheets:

- For Z axis
  - Thickness  $e_z = 0.6 \text{ mm}$
  - Young's modulus  $E_z = 220 \text{ GPa}$  for steel
  - Length  $L_z = 120 \text{ mm}$
  - Stiffness  $k_z \approx 0.8 \text{ N mm}^{-1}$
- For X axis
  - Thickness  $e_x = 1.5 \text{ mm}$
  - Young's modulus  $E_x = 203 \text{ GPa}$  for stainless steel
  - Length  $L_x = 120 \text{ mm}$
  - Stiffness  $k_x \approx 11 \text{ N mm}^{-1}$

These values were chosen for texture recognition applications where the z-axis chosen is low in order to impose a low normal force, which varies little according to the texture. The stiffness chosen is large for the tangential force transducer since much deformation is not desired because there would be uncertainty about the position.

The displacement sensor for the force transducers X and Z are measured with Foucault current sensors from Micro-Epsilon, with models U3 (3 mm measuring range) and EU6 (6 mm measuring range) respectively. These sensors deliver voltage  $U_{x\text{ref}}$  and  $U_{z\text{ref}}$  respectively that is proportional to the displacement of a target steel in front of which they are placed.

The stiffness of the cantilever is very dependent on the thickness and length of the sheets. Foucault current displacement sensors change their behaviour depending on the magnetic environment. Therefore, the force transducer system is characterized once assembled on the complete testing system.

For optimum utilization of the displacement sensors, the characteristic should be adjusted to the environment and to the 0-5 V range of the acquisition system. This is achieved by

three potentiometers of the electronic sensor for setting the zero, linearity and gain. An optical sensor from Micro-Epsilon NCDT1700 1  $\mu\text{m}$  resolution and very good repeatability is used for characterization. Once set, the sensors have a linear characteristic slope of 1.2  $\text{mm V}^{-1}$  for the EU6 sensor, and 0.6  $\text{mm V}^{-1}$  for U3 sensor. Measurement error of these sensors does not exceed 0.3  $\mu\text{m}$  to 0.15  $\mu\text{m}$  for EU6 and U3, respectively.

The force transducers are characterized applying force via a pulley, as shown in Figure A.4

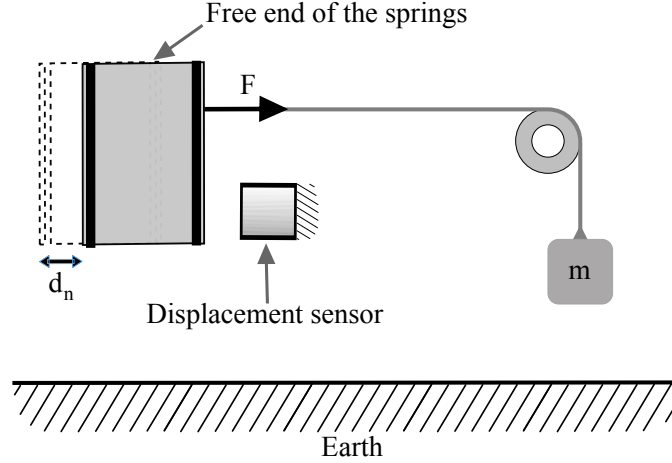


Figure A.4: Force transducer characterisation

Where the reference force  $F$  is equal to mass  $m$  times acceleration  $g$  induced by gravity. The data acquired with different values of  $m$  is shown in the figure A.5.

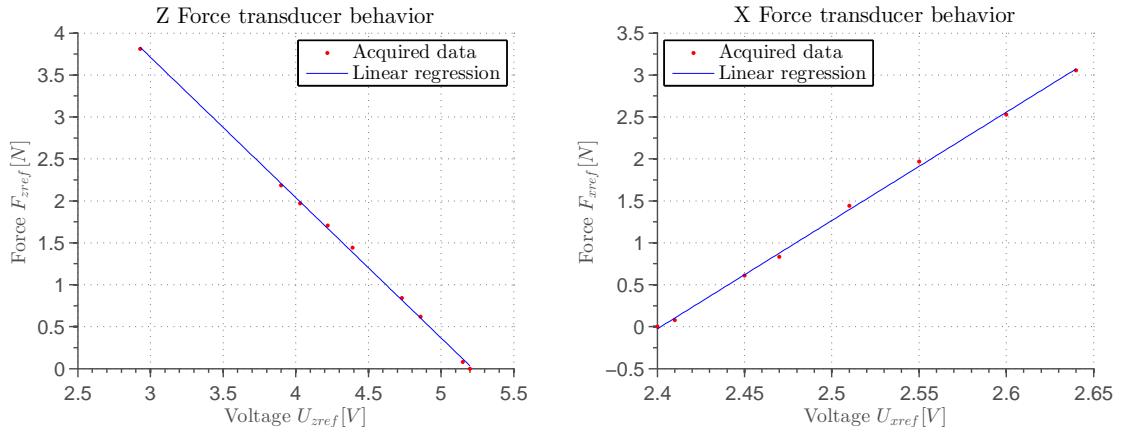


Figure A.5: Measures for the characterization

The force transducer has a linear behaviour, as expected. The equations that represent the two lines for X and Z respectively are

$$f_{xref} = S_{xref}u_{xref} + b_{zref} \quad (\text{A.2})$$

$$f_{zref} = S_{zref}u_{zref} + b_{zref} \quad (\text{A.3})$$

Where  $S_{xref}$  and  $S_{zref}$  are the sensitivities of the system, in the same way  $b_{xref}$  and  $b_{zref}$  are the bias of the resting system. These values are calculated by linear regression, where  $S_{xref} = 12.912 \text{ N V}^{-1}$ ,  $S_{zref} = -1.67 \text{ N V}^{-1}$ ,  $b_{xref} = -31.05 \text{ N}$  and  $b_{zref} = 8.73 \text{ N}$ .

The bimetal force transducer still has the disadvantage of imposing lateral movement  $d_x$  to the end effector when normal force is exerted, forcing a  $d_z$  displacement. When  $d_z$  is small compared to  $L$ ,  $d_x$  can be estimated by the relation  $d_x = L - \sqrt{L^2 - d_z^2}$ . For normal force  $f_z$  in the range of 1 N applied on the end effector, a displacement  $d_z = 0.73$  mm is made, the end effector moves laterally along the x axis of about  $d_x = 2.2$   $\mu$ m. This produces unwanted tangential forces.

**Dynamic characterization** It is necessary to understand what is the dynamic behaviour of the system in order to know what are its limitations. The test performed recreates a step function in the system input. The end effector is brought into contact until a force  $f_{init} \approx 0.6$  N is exerted to the transducer. Then, the pneumatic actuator releases the force automatically. Since no speed or acceleration of the actuator is known and the same method was used to characterize the sensors shown in this paper we consider this as a stepping signal. With these signals the transfer function system is calculated. Starting with the characteristic transfer function of a second order system A.4, as follows:

$$f_{\text{ref}} = \frac{K_p}{1 + 2\xi\tau_\omega s + \tau_\omega^2 s^2} f_{\text{real}} \quad (\text{A.4})$$

Then, it is necessary to find the values  $K_P$ ,  $\xi$ ,  $\tau_\omega$  for each transducer system. These values can be calculated in different ways, for example with Smith's method for underdamped second order systems, or by minimizing the error between the input and output. For simplicity, however, the toolbox of MATLAB for system identification is used. The values are

$$\begin{array}{ll} TF_{f_{z\text{ref}}} & TF_{f_{x\text{ref}}} \\ K_P = 1 & K_P = 1 \\ \xi = 0.0055 & \xi = 0.0088 \\ \tau_\omega = 0.013 & \tau_\omega = 0.0063 \end{array}$$

The acquired signals of force, the calculated model, and the theoretical step signal of force are shown in Figure 1 A.6

The z-axis signal is not complete because the reference sensor does not measure beyond a certain distance. The error of the reference system is analysed in table A.1. It shows the error when the end effector contacts the surface as well as when it does not.

Measure	State	Mean error	Max error	Standard deviation
$f_{x\text{ref}}$	free	2.89 mN	57.11 mN	12.26 mN
	contact	89.06 $\mu$ N	24.85 mN	6.07 mN
$f_{z\text{ref}}$	free	501.06 $\mu$ N	8.36 mN	1.75 mN
	contact	111.67 $\mu$ N	6.76 mN	1.66 mN

Table A.1: Error statistics force transducer

Transducers noise when no force is exerted is greater than when forces are exerted since the system is free and susceptible to environmental perturbations.

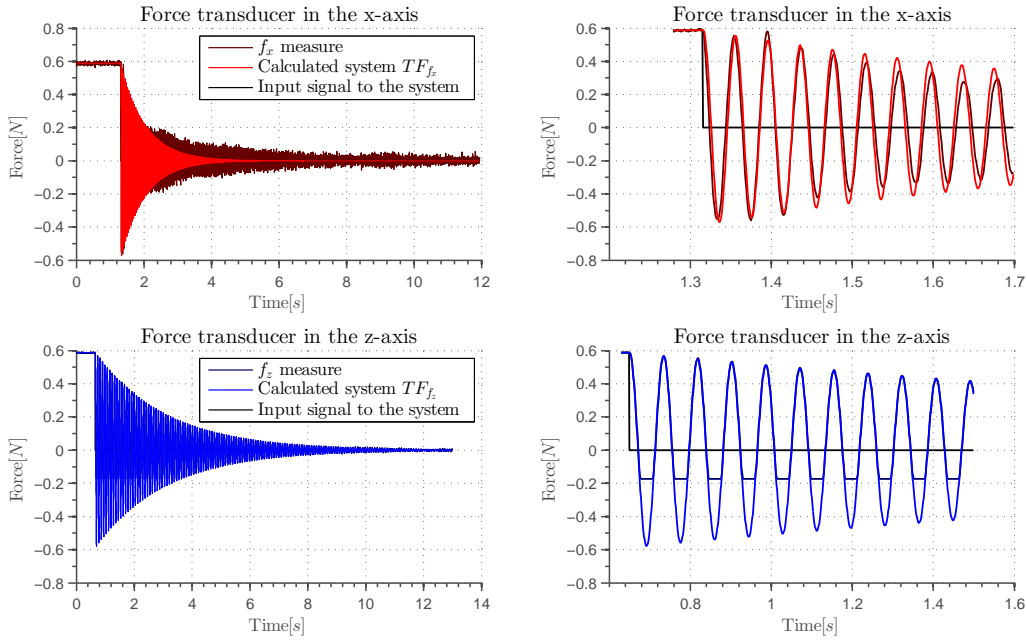


Figure A.6: Dynamic reaction force transducer to step signal

**Conclusion** For the systems presented in this work, this method of measurement is quite problematic because the position has errors depending on the forces applied. And since three-axis force sensors are used, this system only measures two axes.

The signal acquisition system and motor control are presented in section A.2.

#### A.1.1.2 Summary of the characteristics of the system

- Controlled movement by two linear motors in the X and Y axes. (It has not measure of the position in time).
- Movement in the z axis manually controlled by a precision screw
- Measure of the reference forces  $f_{z\text{ref}}$  and  $f_{x\text{ref}}$ .

### A.1.2 Three axis force measurement system

Given the need of the work to characterize different types of 3-axis force sensors, it was decided to change the system shown in A.1. To achieve this, a three-axis sensor is added as shown in Figure A.7

To provide the three-axis force measurement, a force sensor (the K3D40) is placed parallel to the movement of both linear tables. The reference sensor has a noise with a standard deviation of  $0.01N$ . The sensor is coupled to a rigid base through parts made in a 3D printer. This sensor has crosstalk between the axes. To calculate the actual force, the following equation is used:

$$\begin{bmatrix} f_{x\text{ref}} \\ f_{y\text{ref}} \\ f_{z\text{ref}} \end{bmatrix} = \begin{bmatrix} S_{r_{xx}} & S_{r_{xy}} & S_{r_{xz}} \\ S_{r_{yx}} & S_{r_{yy}} & S_{r_{yz}} \\ S_{r_{zx}} & S_{r_{zy}} & S_{r_{zz}} \end{bmatrix} \begin{bmatrix} u_{x\text{ref}} - b_{x\text{ref}} \\ u_{y\text{ref}} - b_{y\text{ref}} \\ u_{z\text{ref}} - b_{z\text{ref}} \end{bmatrix} \frac{1}{V_{in}} \quad (\text{A.5})$$

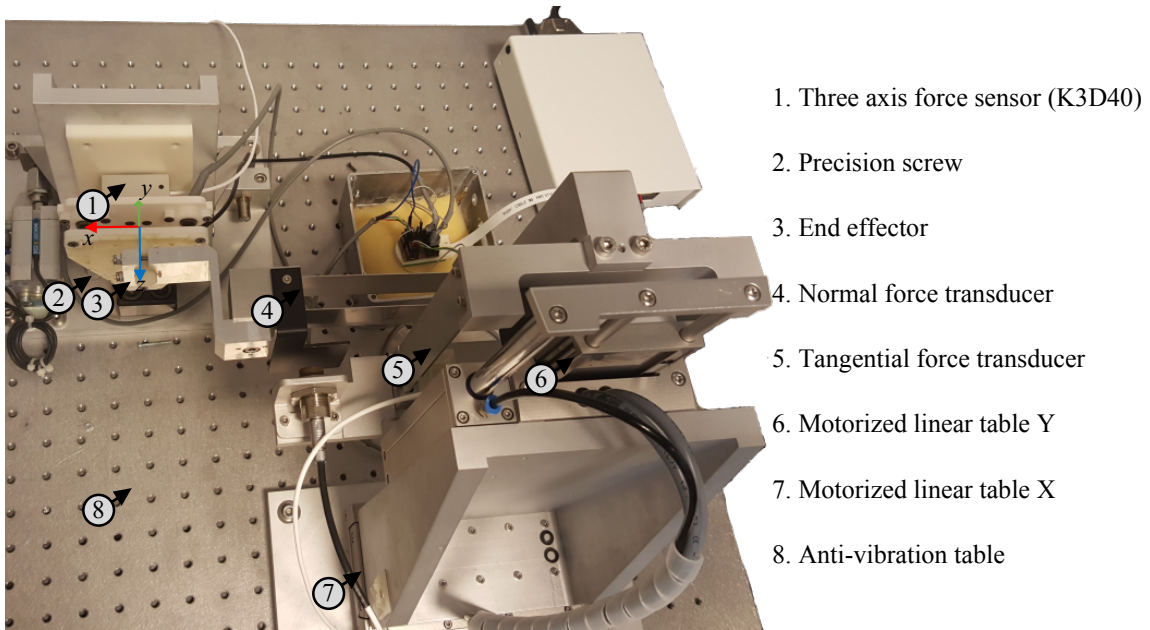


Figure A.7: Three axis force measurement system

Where the forces  $f_{xref}$ ,  $f_{yref}$  and  $f_{zref}$  are proportional to the voltages  $u_{xref}$ ,  $u_{yref}$  and  $u_{zref}$  by a sensitivity matrix  $\mathbf{Sr}$ . The voltages have an offset of  $b_{xref}$ ,  $b_{yref}$  and  $b_{zref}$  and they are proportional to the input voltage  $V_{in}$ . The sensitivity matrix can be calculated from the data given by the manufacturer. This information is shown in table A.2.

axis	rated load in $\text{mV V}^{-1}$	hysteresis
X- axis	0.3334 at 2 N	0.0001
crosstalk X to Y	0.0038	
crosstalk X to Z	0.0141	
Y- axis	0.3519 at 2 N	0.0002
crosstalk Y to X	-0.0008	
crosstalk Y to Z	0.0154	
Z- axis	0.5705 at 2 N	0.0000
crosstalk Z to X	-0.0021	
crosstalk Z to Y	-0.0022	

Table A.2: Reference sensor characteristics: sensibility

The table A.3 show the bias of the sensor.

axis	zero signal in $\text{mV V}^{-1}$
X- axis	0.0091
Y- axis	0.0653
Z- axis	0.0691

Table A.3: Reference sensor characteristics: bias



The characteristics of the K3D40 sensor are shown in the figure A.8

### Technical Data

Design & Material			
Type		3-Axlesensor	
Material		Aluminium	
Length x wide x height	mm x mm x mm	40 x 40 x 20	
Force transmission / fastening		4x M3x0,5	
Weight	g	46	
Mechanical Data			
Nominal force (FS). x-. y-. z-Axis	N	$\pm 2$	$10\pm$
Operating force	%FS	200	200
Breaking force	%FS	600	600
Displacement at FS	mm	0,1	0,1
Natural frequency	Hz	180	400
Spring stiffness	N/mm	20	100
Elektrical Data			
Rated output 1)	mV/V @ FS	0,5 <sup>1)</sup>	
Zero signal toleranz	mV/V	< 0,1	
Max. supply voltage	V	10	
Input resistance	Ohm	350	5
Output resistance	Ohm	350	5
Insulation resistance	Ohm	> 5 10 <sup>9</sup>	
Connection, 12	m	3	
Precision			
Accuracy class	%	0,5	
Linearity error	% FS	0,2	
Reversibility error	% FS	0,1	
Temp. coeff. of the zero signal	%FS / K	0,05	
Temp. coeff. of the nominal output	% RD / K	0,05	
Creep error (30 min)	% FS	0,05	
Eccentricity & Crosstalk			
Allowed torque according of eccentric load	mm	50	
Influence of eccentric load to FS	% FS @ 50mm	0,5	
Crosstalk from x to y at rated load	% FS	<0,5	
Crosstalk from y to x at rated load	% FS	<0,5	
Crosstalk from z to x/y at rated load	% FS	<1	
Temperature			
Nominal temperature range	°C	-20...+60	
Operating temperature range	°C	-20...+70	
Storage temperature range	°C	-20...+70	

Figure A.8: Characteristics of the K3D40 sensor

The signal acquisition system and motor control is presented in section A.2

#### A.1.2.1 Summary of the characteristics of the system

- Controlled movement by two linear motors in the X and Y axes. (It has not measure of the position in time).

- Movement in the  $z$  axis manually controlled by a precision screw
- Measure of the reference forces  $f_{xref}$ ,  $f_{yref}$  and  $f_{zref}$ .

## A.2 Data acquisition and motor control

In this section the control and data acquisition systems presented in this appendix are explained.

### A.2.1 Data acquisition

The acquisition card NI PXI-6225 integrated into the chassis NI PXe-1071i is used to digitize the signal. This system has a programmable sampling frequency  $f_e$ . The filtering unit includes an elliptical low-pass filter of the eighth order, with a programmable cut-off frequency. In general, the filter cut-off frequency is automatically adjusted to about  $\frac{f_e}{3}$ . Different programs are developed in LabVIEW to acquire the signals.

### A.2.2 Motor control

To control the linear motors Lx80F40 Linax and Jenny Science presented in the previous appendixes, two XENAX controllers are used. The commands are programmed into a computer via an application developed in LabVIEW and they are sent via Ethernet to the controllers. In this system, the movement speed, the positions, and the time the system stays in one position could be fixed, with the inconvenient that there is no feedback of position against time.



# Bibliography

- [Alc+13] N. Alcheikh et al. “Characterization and modeling of a piezoresistive three-axial force micro sensor”. In: *Sensors and Actuators A: Physical* 201 (Oct. 15, 2013), pp. 188–192. DOI: 10.1016/j.sna.2013.07.001 (cit. on pp. 7, 35, 36).
- [Ati] *ATI Industrial Automation*. URL: [http://www.ati-ia.com/products/ft/ft\\_models.aspx?id=Nano17](http://www.ati-ia.com/products/ft/ft_models.aspx?id=Nano17) (visited on 10/13/2014) (cit. on pp. 2, 36).
- [Bar+04] F. Barbagli et al. “Simulating human fingers: a soft finger proxy model and algorithm”. In: *12th International Symposium on Haptic Interfaces for Virtual Environment and Teleoperator Systems, 2004. HAPTICS '04. Proceedings*. 12th International Symposium on Haptic Interfaces for Virtual Environment and Teleoperator Systems, 2004. HAPTICS '04. Proceedings. Mar. 2004, pp. 9–17. DOI: 10.1109/HAPTIC.2004.1287172 (cit. on pp. 71, 73).
- [Bat+16] E. Battaglia et al. “ThimbleSense: A Fingertip-Wearable Tactile Sensor for Grasp Analysis”. In: *IEEE Transactions on Haptics* 9.1 (Jan. 2016), pp. 121–133. DOI: 10.1109/TOH.2015.2482478 (cit. on pp. 2, 36).
- [BC94] A. Bicchi and G. Canepa. “Optimal design of multivariate sensors”. In: *Measurement Science and Technology* 5.4 (1994), p. 319. DOI: 10.1088/0957-0233/5/4/001 (cit. on p. 56).
- [Bec+05] L. Beccai et al. “Design and fabrication of a hybrid silicon three-axial force sensor for biomechanical applications”. In: *Sensors and Actuators A: Physical* 120.2 (May 17, 2005), pp. 370–382. DOI: 10.1016/j.sna.2005.01.007 (cit. on p. 7).
- [Bec+08] L. Beccai et al. “Development and Experimental Analysis of a Soft Compliant Tactile Microsensor for Anthropomorphic Artificial Hand”. In: *Mechatronics, IEEE/ASME Transactions on* 13.2 (Apr. 2008), pp. 158–168. DOI: 10.1109/TMECH.2008.918483 (cit. on pp. 7–9).
- [Bia+05] L. Biagiotti et al. “Modelling and identification of soft pads for robotic hands”. In: *2005 IEEE/RSJ International Conference on Intelligent Robots and Systems*. 2005 IEEE/RSJ International Conference on Intelligent Robots and Systems. Aug. 2005, pp. 2786–2791. DOI: 10.1109/IR0S.2005.1545529 (cit. on pp. 72, 73, 79, 82, 83).
- [Bou+13] M. Boukallel et al. “Flexible Tactile Sensors for Multidigital Dexterous In-Hand Manipulation”. In: *Flexible Robotics*. Ed. by thieu Grossard, Nicolas Chaillet, and Stéphane Régnier. John Wiley & Sons, Inc., 2013, pp. 181–242 (cit. on p. 59).
- [BSB93] A. Bicchi, J. Salisbury, and D. Brock. “Contact Sensing from Force Measurements”. In: *The International Journal of Robotics Research* 12.3 (June 1, 1993), pp. 249–262. DOI: 10.1177/027836499301200304 (cit. on pp. 36, 38–40, 59, 63).
- [Cho10] W. Choi. “Polymer micromachined flexible tactile sensor for three-axial loads detection”. In: *Transactions on Electrical and Electronic Materials* 11.3 (2010), pp. 130–133 (cit. on p. 7).
- [Cio+13] V. Ciobanu et al. “Tactile sensor value preprocessing pipeline”. In: *System Theory, Control and Computing (ICSTCC)*, 2013 17th International Conference. Oct. 2013, pp. 674–680. DOI: 10.1109/ICSTCC.2013.6689038 (cit. on p. 2).

- [CM05] G. Cannata and M. Maggiali. “An embedded tactile and force sensor for robotic manipulation and grasping”. In: *2005 5th IEEE-RAS International Conference on Humanoid Robots*. 2005 5th IEEE-RAS International Conference on Humanoid Robots. Dec. 2005, pp. 80–85. DOI: 10.1109/ICHR.2005.1573549 (cit. on p. 37).
- [CM06] G. Cannata and M. Maggiali. “Processing of Tactile/Force Measurements for a Fully Embedded Sensor”. In: *2006 IEEE International Conference on Multisensor Fusion and Integration for Intelligent Systems*. 2006 IEEE International Conference on Multisensor Fusion and Integration for Intelligent Systems. Sept. 2006, pp. 160–166. DOI: 10.1109/MFI.2006.265617 (cit. on pp. 37, 38).
- [CPD11] R. Candelier, A. Prevost, and G. Debrégeas. “The Role of Exploratory Conditions in Bio-Inspired Tactile Sensing of Single Topological Features”. In: *Sensors (Basel, Switzerland)* 11.8 (Aug. 11, 2011), pp. 7934–7953. DOI: 10.3390/s110807934 (cit. on pp. 2, 7–9, 35).
- [CTW97] D.G. Caldwell, N. Tsagarakis, and A Wardle. “Mechano thermo and proprioceptor feedback for integrated haptic feedback”. In: *, 1997 IEEE International Conference on Robotics and Automation, 1997. Proceedings.* , 1997 IEEE International Conference on Robotics and Automation, 1997. Proceedings. Vol. 3. Apr. 1997, 2491–2496 vol.3. DOI: 10.1109/ROBOT.1997.619335 (cit. on p. 32).
- [Dah+10] R.S. Dahiya et al. “Tactile Sensing #x2014;From Humans to Humanoids”. In: *IEEE Transactions on Robotics* 26.1 (Feb. 2010), pp. 1–20. DOI: 10.1109/RO.2009.2033627 (cit. on pp. 1, 30, 31, 33, 34, 46, 63).
- [Dao+01] D. Dao et al. “Micro force-moment sensor with six-degree of freedom”. In: *Proceedings of 2001 International Symposium on Micromechatronics and Human Science, 2001. MHS 2001.* 2001, pp. 93–98. DOI: 10.1109/MHS.2001.965228 (cit. on pp. 7, 36).
- [DB+09] F. De Boissieu et al. “Tactile texture recognition with a 3-axial force MEMS integrated artificial finger.” In: *Robotics: Science and Systems*. Seattle, WA, 2009, pp. 49–56 (cit. on p. 5).
- [Db10] F. De boissieu. “Toucher artificiel à base d’un microcapteur d’effort: traitement du signal et des informations associées”. Thèse de doctorat dirigée par Servièrè, Christine Signal, image, parole, télécoms Grenoble, INPG 2010 2010INPG0041. Doctorat. 2010. 1 vol. (164 p.) (Cit. on pp. 2, 7–9, 12, 14, 15, 21, 103).
- [DDR85] P. Dario and D. De Rossi. “Tactile sensors and the gripping challenge: Increasing the performance of sensors over a wide range of force is a first step toward robotry that can hold and manipulate objects as humans do”. In: *IEEE Spectrum* 22.8 (Aug. 1985), pp. 46–53. DOI: 10.1109/MSPEC.1985.6370785 (cit. on p. 33).
- [DMNP12] G. De Maria, C. Natale, and S. Pirozzi. “Force/tactile sensor for robotic applications”. In: *Sensors and Actuators A: Physical* 175 (Mar. 2012), pp. 60–72. DOI: 10.1016/j.sna.2011.12.042 (cit. on p. 36).
- [DN04] J Dargahi and S Najarian. “Human tactile perception as a standard for artificial tactile sensing—a review”. In: *The International Journal of Medical Robotics and Computer Assisted Surgery* 1.1 (2004), pp. 23–35. DOI: 10.1002/rcs.3 (cit. on pp. 31, 33).

- [FAG13] M.T. Francomano, D. Accoto, and E. Guglielmelli. “Artificial Sense of Slip 2014;A Review”. In: *IEEE Sensors Journal* 13.7 (July 2013), pp. 2489–2498. DOI: 10.1109/JSEN.2013.2252890 (cit. on p. 2).
- [FD76] W.N. Findley and F.A. Davis. *Creep and Relaxation of Nonlinear Viscoelastic Materials*. Google-Books-ID: AZuNioxH\_i4C. Courier Corporation, 1976. 402 pp. (cit. on pp. 71–74, 76).
- [For] “Force activated touch screen measuring deformation of the front panel”. Pat. Classification aux États-Unis 178/18.01, 345/179, 345/156, 345/174, 345/173; Classification internationale G06F3/041, G06F3/03, G06F3/033; Classification coopérative G06F3/0414; Classification européenne G06F3/041F (cit. on p. 36).
- [Fun93] Y. C. Fung. *Biomechanics: Mechanical Properties of Living Tissues*. Google-Books-ID: yx3aBwAAQBAJ. Springer Science & Business Media, 1993. 585 pp. (cit. on pp. 72, 74).
- [GMP15] M. Grossard, J. Martin, and G. F. d C. Pacheco. “Control-Oriented Design and Robust Decentralized Control of the CEA Dexterous Robot Hand”. In: *IEEE/ASME Transactions on Mechatronics* 20.4 (Aug. 2015), pp. 1809–1821. DOI: 10.1109/TMECH.2014.2355040 (cit. on pp. 1, 63).
- [GRP89] S. Goyal, A. Ruina, and J. Papadopoulos. “Limit surface and moment function descriptions of planar sliding”. In: , *1989 IEEE International Conference on Robotics and Automation, 1989. Proceedings.* , 1989 IEEE International Conference on Robotics and Automation, 1989. Proceedings. May 1989, 794–799 vol.2. DOI: 10.1109/ROBOT.1989.100081 (cit. on pp. 66, 67).
- [GRP91] S. Goyal, A. Ruina, and J. Papadopoulos. “Planar sliding with dry friction Part 1. Limit surface and moment function”. In: *Wear* 143.2 (Mar. 20, 1991), pp. 307–330. DOI: 10.1016/0043-1648(91)90104-3 (cit. on pp. 66, 67).
- [Har80] Leon D. Harmon. *Touch-sensing Technology: A Review*. Society of Manufacturing Engineers, 1980. 57 pp. (cit. on pp. 30, 33).
- [HC75] K. H. Hunt and F. R. E. Crossley. “Coefficient of Restitution Interpreted as Damping in Vibroimpact”. In: *Journal of Applied Mechanics* 42.2 (June 1, 1975), pp. 440–445. DOI: 10.1115/1.3423596 (cit. on p. 73).
- [HC96] R.D. Howe and M.R. Cutkosky. “Practical Force-Motion Models for Sliding Manipulation”. In: *The International Journal of Robotics Research* 15.6 (Dec. 1, 1996), pp. 557–572. DOI: 10.1177/027836499601500603 (cit. on p. 66).
- [HK99] H.Y. Han and S. Kawamura. “Analysis of stiffness of human fingertip and comparison with artificial fingers”. In: *1999 IEEE International Conference on Systems, Man, and Cybernetics, 1999. IEEE SMC '99 Conference Proceedings.* 1999 IEEE International Conference on Systems, Man, and Cybernetics, 1999. IEEE SMC '99 Conference Proceedings. Vol. 2. 1999, 800–805 vol.2. DOI: 10.1109/ICSMC.1999.825364 (cit. on p. 73).
- [Ho+11] V. Ho et al. “Development and Analysis of a Sliding Tactile Soft Fingertip Embedded With a Microforce/Moment Sensor”. In: *IEEE Transactions on Robotics* 27.3 (June 2011), pp. 411–424. DOI: 10.1109/TR0.2010.2103470 (cit. on pp. 7–9).
- [How93] Robert D. Howe. “Tactile sensing and control of robotic manipulation”. In: *Advanced Robotics* 8.3 (Jan. 1, 1993), pp. 245–261. DOI: 10.1163/156855394X00356 (cit. on p. 30).

- [HTA10] R. Hanyu, T. Tsuji, and S. Abe. “A simplified whole-body haptic sensing system with multiple supporting points”. In: *2010 11th IEEE International Workshop on Advanced Motion Control*. 2010 11th IEEE International Workshop on Advanced Motion Control. Mar. 2010, pp. 691–696. DOI: 10.1109/AMC.2010.5464045 (cit. on pp. 36, 45).
- [IH03] T. Inoue and S. Hirai. “Modeling of soft fingertip for object manipulation using tactile sensing”. In: *2003 IEEE/RSJ International Conference on Intelligent Robots and Systems, 2003. (IROS 2003). Proceedings*. 2003 IEEE/RSJ International Conference on Intelligent Robots and Systems, 2003. (IROS 2003). Proceedings. Vol. 3. Oct. 2003, 2654–2659 vol.3. DOI: 10.1109/IROS.2003.1249271 (cit. on pp. 69, 79).
- [Jac+88] S.C. Jacobsen et al. “Design of tactile sensing systems for dextrous manipulators”. In: *IEEE Control Systems Magazine* 8.1 (Feb. 1988), pp. 3–13. DOI: 10.1109/37.462 (cit. on p. 33).
- [Jam86] J.W. Jameson. *Analytic techniques for automated grasp*. UMI, 1986 (cit. on p. 66).
- [JJ87] K. L. Johnson and K.L. Johnson. *Contact Mechanics*. Google-Books-ID: Do6WQIUwbpkC. Cambridge University Press, Aug. 28, 1987. 472 pp. (cit. on p. 77).
- [KDR94] B Kloeck and NF De Rooij. “Mechanical sensors”. In: *Semiconductor Sensors* (1994), pp. 153–204 (cit. on p. 10).
- [Kim+06] K. Kim et al. “3-Axes Flexible Tactile Sensor Fabricated by Si Micromachining and Packaging Technology”. In: *19th IEEE International Conference on Micro Electro Mechanical Systems, 2006. MEMS 2006 Istanbul*. 19th IEEE International Conference on Micro Electro Mechanical Systems, 2006. MEMS 2006 Istanbul. 2006, pp. 678–681. DOI: 10.1109/MEMSYS.2006.1627890 (cit. on p. 7).
- [KK97] P. R. Kraus and V. Kumar. “Compliant contact models for rigid body collisions”. In: *, 1997 IEEE International Conference on Robotics and Automation, 1997. Proceedings.* , 1997 IEEE International Conference on Robotics and Automation, 1997. Proceedings. Vol. 2. Apr. 1997, 1382–1387 vol.2. DOI: 10.1109/ROBOT.1997.614330 (cit. on p. 73).
- [KY04] I. Kao and F. Yang. “Stiffness and contact mechanics for soft fingers in grasping and manipulation”. In: *IEEE Transactions on Robotics and Automation* 20.1 (Feb. 2004), pp. 132–135. DOI: 10.1109/TRA.2003.820868 (cit. on p. 73).
- [Lee+08] H. Lee et al. “Normal and Shear Force Measurement Using a Flexible Polymer Tactile Sensor With Embedded Multiple Capacitors”. In: *Journal of Microelectromechanical Systems* 17.4 (Aug. 2008), pp. 934–942. DOI: 10.1109/JMEMS.2008.921727 (cit. on pp. 7, 35).
- [Lee00] Mark H. Lee. “Tactile Sensing: New Directions, New Challenges”. In: *The International Journal of Robotics Research* 19.7 (July 1, 2000), pp. 636–643. DOI: 10.1177/027836490001900702 (cit. on pp. 33, 34).
- [LN99] M. H Lee and H. R Nicholls. “Review Article Tactile sensing for mechatronics—a state of the art survey”. In: *Mechatronics* 9.1 (Feb. 1, 1999), pp. 1–31. DOI: 10.1016/S0957-4158(98)00045-2 (cit. on pp. 1, 30, 33).

- [Mel+14] C. Melchiorri et al. “A new force/torque sensor for robotic applications based on optoelectronic components”. In: *2014 IEEE International Conference on Robotics and Automation (ICRA)*. 2014 IEEE International Conference on Robotics and Automation (ICRA). May 2014, pp. 6408–6413. DOI: 10.1109/ICRA.2014.6907805 (cit. on p. 36).
- [Mel00] C. Melchiorri. “Slip detection and control using tactile and force sensors”. In: *IEEE/ASME Transactions on Mechatronics* 5.3 (Sept. 2000), pp. 235–243. DOI: 10.1109/3516.868914 (cit. on p. 2).
- [MG14] J. Martin and M. Grossard. “Design of a fully modular and backdrivable dexterous hand”. In: *The International Journal of Robotics Research* 33.5 (2014), pp. 783–798 (cit. on p. 1).
- [MO99] D. W. Marhefka and D. E. Orin. “A compliant contact model with nonlinear damping for simulation of robotic systems”. In: *IEEE Transactions on Systems, Man, and Cybernetics - Part A: Systems and Humans* 29.6 (Nov. 1999), pp. 566–572. DOI: 10.1109/3468.798060 (cit. on p. 73).
- [Mur+94] R.M. Murray et al. *A mathematical introduction to robotic manipulation*. CRC press, 1994 (cit. on pp. 1, 58).
- [Nod+06] K. Noda et al. “A shear stress sensor for tactile sensing with the piezoresistive cantilever standing in elastic material”. In: *Sensors and Actuators A: Physical*. MEMS 2005 Special Issue Special Issue of the Micromechanics Section of Sensors and Actuators (SAMM), based on contributions revised from the technical digest of the IEEE 18th International Conference on Micro Electro Mechanical Systems (MEMS-2005). 127.2 (Mar. 13, 2006), pp. 295–301. DOI: 10.1016/j.sna.2005.09.023 (cit. on p. 7).
- [Nod+09] K. Noda et al. “MEMS on robot applications”. In: *TRANSDUCERS 2009 - 2009 International Solid-State Sensors, Actuators and Microsystems Conference*. TRANSDUCERS 2009 - 2009 International Solid-State Sensors, Actuators and Microsystems Conference. June 2009, pp. 2176–2181. DOI: 10.1109/SENSOR.2009.5285608 (cit. on p. 7).
- [PH99] D. T. V. Pawluk and R. D. Howe. “Dynamic Lumped Element Response of the Human Fingerpad”. In: *Journal of Biomechanical Engineering* 121.2 (Apr. 1, 1999), pp. 178–183. DOI: 10.1115/1.2835100 (cit. on pp. 72, 73, 82).
- [PR68] A. C. Pipkin and T. G. Rogers. “A non-linear integral representation for viscoelastic behaviour”. In: *Journal of the Mechanics and Physics of Solids* 16.1 (Jan. 1, 1968), pp. 59–72. DOI: 10.1016/0022-5096(68)90016-1 (cit. on p. 72).
- [Pre] *Pressure Profile* (cit. on p. 35).
- [Reb04] G.M. Rebeiz. *RF MEMS: Theory, Design, and Technology*. Google-Books-ID: A7728XHtmzAC. John Wiley & Sons, Feb. 6, 2004. 508 pp. (cit. on p. 6).
- [Rei+14] J. Reinecke et al. “Experimental comparison of slip detection strategies by tactile sensing with the BioTac ; on the DLR hand arm system”. In: *2014 IEEE International Conference on Robotics and Automation (ICRA)*. 2014 IEEE International Conference on Robotics and Automation (ICRA). May 2014, pp. 2742–2748. DOI: 10.1109/ICRA.2014.6907252 (cit. on p. 2).



- [Sar+12] R. Sargeant et al. “An optical multi-axial force/torque sensor for dexterous grasping and manipulation”. In: *2012 IEEE Conference on Multisensor Fusion and Integration for Intelligent Systems (MFI)*. 2012 IEEE Conference on Multisensor Fusion and Integration for Intelligent Systems (MFI). Sept. 2012, pp. 144–149. DOI: 10.1109/MFI.2012.6343043 (cit. on p. 36).
- [Soh+09] M. Sohgawa et al. “Tactile array sensor with inclined chromium/silicon piezoresistive cantilevers embedded in elastomer”. In: *Solid-State Sensors, Actuators and Microsystems Conference, 2009. TRANSDUCERS 2009. International*. Solid-State Sensors, Actuators and Microsystems Conference, 2009. TRANSDUCERS 2009. International. June 2009, pp. 284–287. DOI: 10.1109/SENSOR.2009.5285509 (cit. on p. 7).
- [Son+12] X. Song et al. “A novel dynamic slip prediction and compensation approach based on haptic surface exploration”. In: *2012 IEEE/RSJ International Conference on Intelligent Robots and Systems (IROS)*. 2012 IEEE/RSJ International Conference on Intelligent Robots and Systems (IROS). Oct. 2012, pp. 4511–4516. DOI: 10.1109/IROS.2012.6385897 (cit. on p. 36).
- [Syn] *Syntouchllc*. URL: <http://www.syntouchllc.com/Products/BioTac/> (visited on 10/13/2014) (cit. on pp. 2, 37).
- [TK07] P. Tiezzi and I. Kao. “Modeling of Viscoelastic Contacts and Evolution of Limit Surface for Robotic Contact Interface”. In: *IEEE Transactions on Robotics* 23.2 (Apr. 2007), pp. 206–217. DOI: 10.1109/TR0.2006.889494 (cit. on pp. 71, 72, 77, 78, 88–91, 94).
- [TK09] C. H. D. Tsai and I. Kao. “The latency model for viscoelastic contact interface in robotics: Theory and experiments”. In: *IEEE International Conference on Robotics and Automation, 2009. ICRA '09*. IEEE International Conference on Robotics and Automation, 2009. ICRA '09. May 2009, pp. 1291–1296. DOI: 10.1109/ROBOT.2009.5152679 (cit. on p. 91).
- [TV05] P. Tiezzi and G. Vassura. “Experimental analysis of soft fingertips with internal rigid core”. In: *ICAR '05. Proceedings., 12th International Conference on Advanced Robotics, 2005*. ICAR '05. Proceedings., 12th International Conference on Advanced Robotics, 2005. July 2005, pp. 109–114. DOI: 10.1109/ICAR.2005.1507399 (cit. on p. 99).
- [Vis+10] Y. Visell et al. “Interaction capture in immersive virtual environments via an intelligent floor surface.” In: *VR*. 2010, pp. 313–314 (cit. on p. 36).
- [Vá07] G. Vászárhelyi. “The Design of Tactile Sensors and Their Elastic Cover”. In: *Péter Pázmány Catholic University, Faculty of Information Technology, Multidisciplinary Technical Sciences Doctoral School, Budapest* (2007), pp. 1–19 (cit. on pp. 7, 8).
- [WB00] L. Wang and D. Beebe. “A silicon-based shear force sensor: development and characterization”. In: *Sensors and Actuators A: Physical* 84.1 (Aug. 1, 2000), pp. 33–44. DOI: 10.1016/S0924-4247(99)00342-8 (cit. on p. 7).
- [Wei] *Weiss-robotics* (cit. on p. 35).
- [Wol06] J. Wolfe. *Sensation and perception*. Sinauer Associates Inc, 2006 (cit. on p. 31).

- [XK00] N. Xydas and I. Kao. “Influence of material properties and fingertip size on the power-law equation for soft fingers”. In: *2000 IEEE/RSJ International Conference on Intelligent Robots and Systems, 2000. (IROS 2000). Proceedings.* 2000 IEEE/RSJ International Conference on Intelligent Robots and Systems, 2000. (IROS 2000). Proceedings. Vol. 2. 2000, 1285–1290 vol.2. DOI: 10.1109/IROS.2000.893196 (cit. on p. 79).
- [XK99] N. Xydas and I. Kao. “Modeling of Contact Mechanics and Friction Limit Surfaces for Soft Fingers in Robotics, with Experimental Results”. In: *The International Journal of Robotics Research* 18.9 (Sept. 1, 1999), pp. 941–950. DOI: 10.1177/02783649922066673 (cit. on pp. 69, 70, 73, 79, 94).
- [Yan66] W.H. Yang. “The Contact Problem for Viscoelastic Bodies”. In: *Journal of Applied Mechanics* 33.2 (June 1, 1966), pp. 395–401. DOI: 10.1115/1.3625055 (cit. on p. 77).
- [Yao+87] CT Yao et al. “A novel three-dimensional microstructure fabrication technique for a triaxial tactile sensor array”. In: *Proceedings of the IEEE Micro-Robotics and Teleoperators Workshop.* Vol. 6. 1987 (cit. on p. 9).
- [YBA11] H. Yousef, M. Boukallel, and K. Althoefer. “Tactile sensing for dexterous in-hand manipulation in robotics—A review”. In: *Sensors and Actuators A: Physical* 167.2 (June 2011), pp. 171–187. DOI: 10.1016/j.sna.2011.02.038 (cit. on pp. 1, 7, 30, 33, 34, 63).
- [ZSL96] X. Zhou, Q. Shi, and Z. Li. “Contact localization using force/torque measurements”. In: *, 1996 IEEE International Conference on Robotics and Automation, 1996. Proceedings.* , 1996 IEEE International Conference on Robotics and Automation, 1996. Proceedings. Vol. 2. Apr. 1996, 1339–1344 vol.2. DOI: 10.1109/ROBOT.1996.506892 (cit. on pp. 36, 61).



---

**Résumé** — La détection tactile et la détection de glissement jouent un rôle important en permettant la manipulation robotique dextre des objets. Ainsi, le développement d'un système de capteur tactile entièrement intégré à haute résolution présente un intérêt certain. Ces travaux traitent de la conception et de la mise en place d'un système tactile intrinsèque basé sur un ensemble de capteurs MEMs de force à 3 axes et la détection du glissement avec ce système. Afin de créer un système tactile, les capteurs de force à 3 axes sont protégés par un revêtement, une étude sur le revêtement est réalisée. Deux systèmes intrinsèques différents basés sur un ensemble de capteurs de force à 3 axes sont développés, le premier est utilisé comme test de faisabilité de ce type de système. Le deuxième système intrinsèque est adapté à un doigt robotique à surface souple. Les systèmes proposés mesurent trois composants de force, le couple normal à la surface de contact et la position du centre de contact appliqué sur sa surface sensible. Les deux systèmes sont caractérisés et testés. La détection du glissement avec un système tactile intrinsèque est testée également. La détection du glissement est faite par l'application de la théorie de la surface limite et du modèle de contact viscoélastique.

**Mots clés :** Système tactile, détection de glissement, viscoélastique, intrinsèque, capteur de force multi-axe

---

---

**Abstract** — Tactile sensing and slip detection plays an important role in enabling robotic dexterous object manipulation. Thus developing a high-resolution fully integrated tactile sensor system is of great interest. This work deals the design and implementation of an intrinsic tactile sensing system based on a set of 3-axis force MEMs sensors and the detection of slippage with such system. In order to create a tactile system the 3-axis force sensors are protected by a coating, a study about the coating is made. Two different intrinsic systems based on an array of 3-axis force sensors are developed, the first one is used a feasibility test of this kind of system. The second intrinsic system is adapted to a robotic finger with soft surface. The proposed systems measures three-force components, the normal torque to the contact surface, and the position of the contact centroid applied to its sensitive surface. Both systems are characterized and tested. The detection of slippage with an intrinsic tactile system is tested. The application of the limit surface theory and the viscoelastic model of contact make the detection of slippage.

**Keywords:** Tactile system, slippage detection, viscoelastic, intrinsic, multi-axis force sensor

---